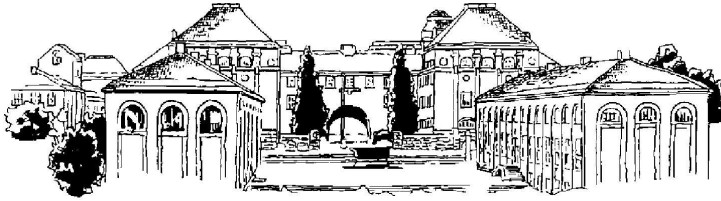




**KTH Information and  
Communication Technology**

# Photonic Devices with MQW Active Material and Waveguide Gratings: Modelling and Characterisation

Muhammad Nadeem Akram



Stockholm 2005

Doctoral Dissertation  
Royal Institute of Technology (KTH)  
Department of Microelectronics and Information Technology

## **Photonic Devices with MQW Active Material and Waveguide Gratings: Modelling and Characterisation**

A dissertation submitted to the Royal Institute of Technology (KTH), Stockholm, Sweden, in partial fulfillment for the degree of Doctor of Philosophy.

Akademisk avhandling som med tillstånd av Kungl Tekniska Högskolan framläggas till offentlig granskning för avläggande av teknisk doktorsexamen fredagen den 7 Oktober 2005 kl 10.00 i sal C1 Electrum, Kungl Tekniska Högskolan, Isafjordsgatan 22, Kista, Stockholm.

Cover Picture: Cross-Section of a Semi-Insulating Buried Heterostructure MQW InP Laser.

ISBN 91-7178-132-3

TRITA-MVT Report 2005-3

ISSN 0348-4467

ISRN KTH/MVT/FR-05/3-SE

© Muhammad Nadeem Akram, Oct 2005

Printed by Universitetsservice US AB, Stockholm 2005

**Akram, Muhammad Nadeem:** Photonic Devices with MQW Active Material and Waveguide Gratings: Modelling and Characterisation

ISBN 91-7178-132-3, ISRN KTH/MVT/FR-05/3-SE

ISSN 0348-4467, TRITA-MVT Report 2005:3

Department of Microelectronics and Information Technology, Optics, Photonics and Quantum Electronics Laboratory, Royal Institute of Technology, Stockholm, Sweden.

## Abstract

The research work presented in this thesis deals with modelling, design and characterisation of passive and active optical waveguide devices. The first part of the thesis is related to algorithm development and numerical modelling of planar optical waveguides and gratings using the Method of Lines (MoL). The basic three-point central-difference approximation of the  $\partial^2/\partial x^2$  operator used in the Helmholtz equation is extended to a new five-point and seven-point approximation with appropriate interface conditions for the *TE* and *TM* fields. Different structures such as a high-contrast waveguide and a *TM* surface plasmon mode waveguide are simulated, and improved numerical accuracy for calculating the optical mode and propagation constant is demonstrated. A new fast and stable non-paraxial bi-directional beam propagation method, called Cascading and Doubling algorithm, is derived to model deep gratings with many periods. This algorithm is applied to model a quasi-guided multi-layer anti-resonant reflecting optical waveguide (ARROW) grating polarizing structure.

In the second part of the thesis, our focus is on active optical devices such as vertical-cavity and edge-emitting lasers. With a view to improve the bandwidth of directly modulated laser, an InGaAsP quantum well with InGaAlAs barrier is studied due to its favorable band offset for hole injection as well as for electron confinement. Quantum wells with different barrier bandgap are grown and direct carrier transport measurements are done using time and wavelength resolved photoluminescence upconversion. Semi-insulating regrown Fabry-Perot lasers are manufactured and experimentally evaluated for light-current, optical gain, chirp and small-signal performance. It is shown that the lasers having MQW with shallow bandgap InGaAlAs barrier have improved carrier transport properties, better  $T_0$ , higher differential gain and lower chirp. For lateral current injection laser scheme, it is shown that a narrow mesa is important for gain uniformity across the active region. High speed directly modulated DBR lasers are evaluated for analog performance and a record high spurious free dynamic range of 103 dB Hz<sup>2/3</sup> for frequencies in the range of 1-19 GHz is demonstrated. Large signal transmission experiment is performed at 40 Gb/s and error free transmission for back-to-back and through 1 km standard single mode fiber is achieved.

**Keywords:** Method of Lines, Grating, ARROW Waveguide, Semiconductor Laser, Quantum Well, Carrier Transport, 40 Gb/s, RF Photonics.



*This thesis is dedicated to my wife Dr. Samira Nadeem, our beloved kids Usama and Aiman and, my parents Chaudhary Muhammad Akram and Rafiq Akram*



# Acknowledgements

First and foremost, I am thankful to my main supervisor Dr. Richard Schatz for accepting me as a PhD student in his group. He has been very cooperative and patient through all the ups and downs during the course of my research work. I am also thankful to him for his efforts to arrange the necessary research funding to carry on experimental work and device manufacturing. Thanks are also due to our chairman Prof. Lars Thylen for his efforts to maintain the research activities in the Photonics Laboratory. I am also thankful to Dr. H. A. Jamid (KFUPM Saudi Arabia) for continued research collaboration. I am grateful to the members of our team, especially Dr. Olle Kjebon, Dr. Saulius Marcinkevičius and Dr. Christofer Silfvenius for their collaboration and guidance. I have learned a lot from them by working in a team environment. I am especially thankful to my all time collaborator Jesper Berggren for his contributions on device epitaxy. We could not have gotten our devices in a short time without his expertise and skills. My PhD scholarship and the device research activities were mainly funded by the Swedish agencies VINNOVA and FMV through the Microwave Photonics project

I enjoyed the company of many talented research students in our laboratory. I would especially like to mention Marek Chacinski, Matteo Dainese, Dmitry Khoptyar, Jessica Sorio, Fredrik Olsson, Amir Abbas Jalali and Sebastian Mogg for their friendship and cooperation. I am grateful to Rashad Ramzan and Mohammad Shafiq for their never ending friendship and the pleasure of their company in Sweden.

I enjoyed and learned a lot from numerous graduate courses taken during my studies. I am thankful to Prof. Sebastian Lourdudoss for the Epitaxy and Device Processing courses, Prof. Shili Zhang for the Device and Material Characterisation course, Dr. Valdas Pasiskevičius (AlbaNova) for the Non-linear Optics Technology course, Prof. Anders Larsson (Chalmers) for the Photonics Devices course, Prof. David Hviland (AlbaNova) for the Electron Beam Lithography training.

In the end, I am extremely thankful and indebted to my dear wife Dr. Samira Nadeem for her constant support and understanding during the long course of my education. She has kept her nerves and diligently took care of me as well as our two kids as I was busy in my studies and work for most of the time during the last 6 years.





# Contents

<b>Abstract</b>	<b>iii</b>
<b>Acknowledgements</b>	<b>vii</b>
<b>List of Papers</b>	<b>xi</b>
<b>Acronyms</b>	<b>xv</b>
<b>1 Introduction</b>	<b>1</b>
1.1 Background and Motivation . . . . .	1
1.2 Thesis Organization . . . . .	4
<b>2 Optical Waveguide Simulation</b>	<b>5</b>
2.1 Introduction . . . . .	5
2.2 Three-Layer Dielectric Slab Waveguide . . . . .	5
2.3 Method of Lines . . . . .	9
2.3.1 Basic 3-Point Formulation of the MoL . . . . .	10
2.3.2 Interface Conditions . . . . .	11
2.3.3 Improved 3-Point Formulation with Interface Conditions . . . . .	12
2.3.4 Higher-Order Formulation with Interface Conditions . . . . .	13
2.4 Perfectly Matched Layer (PML) Absorber . . . . .	13
2.5 Simulation of Discontinuities . . . . .	14
2.5.1 A Single Discontinuity . . . . .	14
2.5.2 A Double Discontinuity . . . . .	15
2.5.3 Multiple Discontinuities . . . . .	16
2.6 Cascading and Doubling Algorithm . . . . .	17
2.6.1 Theory . . . . .	18
2.6.2 Symmetrical and Identical Structures . . . . .	19
2.6.3 Case Study: Uniform Rectangular Grating . . . . .	20
2.7 ARROW Grating Simulation . . . . .	22
2.7.1 Unperturbed ARROW Waveguide . . . . .	22

<b>3</b>	<b>Semiconductor Laser Simulation</b>	<b>25</b>
3.1	Introduction . . . . .	25
3.2	Basic Rate-Equation Model . . . . .	26
3.2.1	Threshold Condition . . . . .	26
3.2.2	Steady-State Characteristics . . . . .	30
3.2.3	Dynamic Characteristics . . . . .	30
3.2.4	Parasitic Effects . . . . .	32
3.3	Self-Consistent 2D Simulation . . . . .	33
3.3.1	Thermionic Emission Current at a Hetero-Junction . . . . .	34
3.4	Multiple Quantum Well Active Region Optimization . . . . .	35
3.4.1	Single Quantum Well Material Gain . . . . .	36
3.4.2	Carrier and Gain Non-Uniformity Among Wells . . . . .	37
3.5	Lateral Current Injection (LCI) Laser . . . . .	38
3.5.1	Introduction . . . . .	38
3.5.2	Device Geometry . . . . .	40
3.5.3	Simulation Model . . . . .	41
<b>4</b>	<b>Characterisation of MQW Active Region and Lasers</b>	<b>45</b>
4.1	Introduction . . . . .	45
4.2	Transient PL Measurement . . . . .	46
4.2.1	Measurement Setup . . . . .	46
4.2.2	MQW Carrier Transport Test Structure . . . . .	46
4.3	FP-Laser Characterisation . . . . .	47
4.3.1	Light-Current and Voltage-Current Measurements . . . . .	49
4.3.2	Optical Gain and Chirp Measurements . . . . .	51
4.3.3	Small-Signal Modulation Response Measurements . . . . .	53
4.4	Wide-Band Directly Modulated DBR Laser . . . . .	57
4.4.1	DBR Laser Structure . . . . .	57
4.4.2	40 Gb/s Transmission . . . . .	57
4.4.3	Analog Distortion in DBR Laser . . . . .	58
<b>5</b>	<b>Summary, Conclusion and Future Work</b>	<b>65</b>
<b>6</b>	<b>Summary of the Original Work</b>	<b>69</b>
	<b>Bibliography</b>	<b>75</b>

# List of Papers

**List of papers included in the thesis:** The thesis is based on the following papers, which will be referred to by their respective letters:

- A. *A New Higher-Order Finite-Difference Approximation Scheme for the Method of Lines*, Hussain A. Jamid and Muhammad Nadeem Akram, IEEE Journal of LightWave Technology, Vol. 19, No. 3, pp. 398-404, March 2001.
- B. *Analysis of Deep Waveguide Gratings: An Efficient Cascading and Doubling Algorithm in the Method of Lines Framework*, Hussain A. Jamid and Muhammad Nadeem Akram, IEEE Journal of LightWave Technology, Vol. 20, No. 7, pp. 1204-1209, July 2002.
- C. *Analysis of Antiresonant Reflecting Optical Waveguide Gratings by use of the Method of Lines*, Hussain A. Jamid and Muhammad N. Akram, Applied Optics, Vol. 42, No. 18, pp. 3488-3494, June 2003.
- D. *Influence of Electrical Parasitics and Drive Impedance on the Laser Modulation Response*, M. Nadeem Akram, Richard Schatz and Olle Kjebon, IEEE Photonics Technology Letters, Vol. 16, No. 1, pp. 21-23, January 2004.
- E. *Design Optimization of InGaAsP-InGaAlAs 1.55  $\mu\text{m}$  Strain Compensated MQW Lasers for Direct Modulation Applications*, M. Nadeem Akram, Christofer Silfvenius, Olle Kjebon and Richard Schatz, Semiconductor Science and Technology, Vol. 19, No. 5, pp. 615-625, May 2004.
- F. *Lateral Current Injection (LCI) Multiple Quantum-well 1.55  $\mu\text{m}$  Laser with Improved Gain Uniformity Across the Active Region*, M. Nadeem Akram, Optical and Quantum Electronics, Vol. 36, No. 9, pp. 827-846, July 2004.
- G. *The Effect of Barrier Composition on the Carrier Transport,  $T_0$ , Gain Spectrum and Chirp of 1.55  $\mu\text{m}$  Multiple Quantum Well Lasers*, M. Nadeem Akram, R. Schatz, S. Marcinkevičius, O. Kjebon and J. Berggren, Manuscript.

- H. *40 Gb/s Transmission Experiment Using Directly Modulated 1.55  $\mu\text{m}$  DBR Lasers*, Olle Kjebon, M. Nadeem Akram and Richard Schatz, International Conference on Indium Phosphide and Related Materials (IPRM), pp. 495-498, 12-16 May 2003.
- I. *Experimental Evaluation of Detuned Loading Effects on the Distortion in Edge Emitting DBR Lasers*, Olle Kjebon, Richard Schatz, C. Carlsson and N. Akram, International Topical Meeting on Microwave Photonics, pp. 125-128, 5-8 Nov. 2002.

**List of papers not included in the thesis:**

- J. *Design of a Multiple Field-of-View Optical System for 3 to 5- $\mu\text{m}$  Infrared Focal-Plane Arrays*, M. Nadeem Akram, Optical Engineering, Vol. 42, No. 6, pp. 1704-1714, June 2003.
- K. *A Design Study of Dual Field-of-View Imaging Systems for the 3-5  $\mu\text{m}$  Waveband Utilizing Focal-Plane Arrays*, M. Nadeem Akram, Journal of Optics A: Pure and Applied Optics, Vol. 5, No. 4, pp. 308-322, July 2003. *(This work was also presented at Novel Optical Systems Design and Optimization V, Proc. SPIE Vol. 4768, Sept 2002).*
- L. *Step-Zoom Dual Field-of-View Infrared Telescope*, M. Nadeem Akram and M. Hammad Asghar, Applied Optics: Optical Technology and Biomedical Optics, Vol. 42, No. 13, pp. 2312-2316, May 2003. *(This work was also presented at International Optical Design Conference 2002, Proc. SPIE Vol. 4832 Dec 2002).*
- M. *Strong 1.3 - 1.6  $\mu\text{m}$  Light Emission From Metamorphic InGaAs Quantum Wells on GaAs*, I. Tångring, S. M. Wang, Q. F. Gu, Y. Q. Wei, M. Sadeghi, A. Larsson, Q. X. Zhao, M. N. Akram and J. Berggren, Applied Physics Letters, Vol. 86, May 2005.

**Miscellaneous contributions:**

- N. *Design and Evaluation of High Speed DBR Lasers for Analog and Digital Transmission*, Richard Schatz, Olle Kjebon and M. N. Akram, Laser and Fiber-Optical Networks modelling, 2003. Proceedings of LFNM 2003. 5th International Workshop, Sept. 2003.
- O. *Design Optimization of InGaAsP-InGaAlAs 1.55  $\mu\text{m}$  Strain Compensated MQW Lasers for Direct Modulation Applications*, M. Nadeem Akram, Christofer Silfvenius, Jesper Berggren, Olle Kjebon, Richard Schatz, Indium Phosphide and Related Material (IPRM) Conference, Kagoshima, Japan, May 2004.
- P. *Efficient Modelling of Bragg Waveguide Gratings using Higher-Order Finite-Difference Approximations*, M. Nadeem Akram, Nordic Semiconductor Conference 2002, Tampere, Finland.

- Q.** *Experimental Evaluation of Carrier Transport, Gain,  $T_0$ , and Chirp of 1.55  $\mu\text{m}$  MQW Structures with Different Barrier Compositions*, M. Nadeem Akram, R. Schatz, S. Marcinkevičius, O. Kjebon and J. Berggren , European Conference on Optical Communications (ECOC), 25 September 2005, Glasgow.



# Acronyms

1D	One Dimensional
2D	Two Dimensional
ABC	Absorbing Boundary Condition
AC	Alternating Current
ARROW	Anti-Resonant Reflecting Optical Waveguide
BPM	Beam Propagation Method
BER	Bit Error Rate
CCD	Charge Coupled Device
DBR	Distributed Bragg Reflector
DC	Direct Current
DFB	Distributed Feed Back
FD	Finite-Difference
FP	Fabry-Perot
Gb/s	Giga-bit per Second
InGaAsP	Indium Gallium Arsenide Phosphide
InGaAlAs	Indium Gallium Aluminium Arsenide
LCI	Lateral Current Injection
MoL	Method of Lines
MQW	Multiple Quantum Well
N <sub>2</sub>	Nitrogen
PL	Photo-Luminescence
PML	Perfectly Matched Layer
QW	Quantum Well
RF	Radio Frequency
SIBH	Semi Insulating Buried Heterostructure
SIFBH	Semi Insulating Flat Buried Heterostructure
TE	Transverse Electric
TM	Transverse Magnetic
TMM	Transfer Matrix Method
VCI	Vertical Current Injection
VCSEL	Vertical Cavity Surface Emitting Laser





# Chapter 1

## Introduction

### 1.1 Background and Motivation

Both active and passive integrated optical devices are essential elements of the modern information driven society. Active devices such as semiconductor lasers, detectors and optical amplifiers are used to transmit, detect and amplify data in the form of optical pulses through optical fiber. Waveguide gratings are useful for wavelength and polarization filtering. If gratings are included in the laser cavity, we can have a single wavelength laser which is useful as a transmitter for long distance high bit rate optical communication. It is essential to evaluate the performance of such active and passive optical devices. Since not all the practical problems can be solved analytically, one has to resort to numerical methods which have become an essential and useful tool for the design and simulation of integrated optical devices. It is equally important to measure the device performance once it is manufactured. The measurements not only give true performance of a device, but also point out any shortcomings during the design or the manufacturing phase. Thus one can come up with new solutions to improve the performance of an existing device or have new device concepts to overcome the limitations imposed by the present devices.

The classic problem to model scattering from single and multiple discontinuities has been solved by many researchers using different numerical methods such as the Equivalent Transmission-Line Network Method [1], the Mode Matching Method [2], the Method of Lines [3–11] and Collocation Method [12]. A good reference to these and some other methods is given in [2] and [13]. Marcuse [14] used coupled-mode theory to analyze a slab waveguide with sinusoidal deformation on one interface. The spectral response of a grating filter using coupled-mode theory was calculated and compared with experimental work in [15]. The Effective-Index method was also used [16] to model a waveguide grating and the results compared with coupled-mode theory. A major limitation of the coupled-mode theory is that it can only model small perturbations due to its approximate

formulation. In order to simulate optical waveguides for modal analysis as well as for beam propagation, we have used Method of Lines (MoL) as a numerical tool in this thesis. MoL is a semi-analytical technique useful for the solution of partial differential equations (PDE). In this method, all independent variables except one are discretized and thus, the partial differential equation is transformed into a set of ordinary differential equations (ODE) which can be solved analytically [17]. This results in a higher numerical accuracy, less computational time and smaller memory requirements as compared to fully-discretizing finite-difference techniques. This method can be used to calculate the modes and propagation constants of a multilayer waveguide. This method can also be used for bi-directional beam propagation and can account for backward-reflected field from longitudinally inhomogeneous structures such as deep waveguide junctions and gratings. It has been applied to model integrated optical and microwave waveguide problems [18–22]. In this thesis, MoL is also applied to model Anti-resonant reflecting optical waveguides (ARROW) and grating structures and find their modal and spectral properties. ARROW structure is interesting due to its attractive features such as low transmission loss, high polarization selectivity, single mode capability even for large core thickness, and compatibility with mono-mode optical fibers due to the relatively large core size and small refractive index mismatch [23, 24]. Such waveguides can be integrated monolithically with electronic components in the  $\text{SiO}_2/\text{Si}$  material system [25]. Unlike conventional waveguides that depend on total internal reflection (TIR) for the guidance of the optical field in a region of high refractive index surrounded by regions of lower refractive index, the ARROW structure partially depends on a reflective multilayer structure for guidance in a medium of low refractive index surrounded by a medium of high refractive index. Since TIR at the core-cladding interface may not be realized in this situation, the ARROW structure is a leaky waveguide [26]. The radiation losses of the leaky waves are reduced by the high reflectivity of the anti-resonant cladding layer. When periodic corrugations are introduced on the top surface of an ARROW waveguide, an ARROW grating is obtained which leads to an optical wavelength filter. It is well known that  $TM$  polarized modes of the unperturbed ARROW waveguide are highly lossy [23]. Thus, in addition to being a wavelength filter, the ARROW grating is also expected to behave as a  $TE$ -pass reflection-mode polarizer.

Next we move to the active waveguide devices, that is lasers. Directly modulated semiconductor injection lasers with multiple quantum well (MQW) active region are important sources for high bit-rate data transmission [27–29]. The simulation of such devices can be based on 0-D rate-equations model [30], 1-D longitudinally resolved methods such as Transfer Matrix Method (TMM) [31] and Transmission Line Laser Method (TLLM) [32], 2-D physics based drift-diffusion model coupled to the optical gain model and waveguide model [33] for the device transverse structure, or complete 3-D transverse and longitudinally resolved model [34]. The 0-D model is based on a lumped model of the whole laser cavity and simulates the interaction between carriers and photons. It is useful for simple circuit level modelling of the device and helps calculate the

device performance with minimum number of parameters. The 1-D longitudinally resolved modelling is useful to simulate inhomogeneous carrier and photon distribution along the length of the laser cavity and can find static and dynamic properties of complicated devices having gratings in the cavity as well. The 2D or 3D physics based modelling is a comprehensive model based on the solution of corresponding partial differential equations for the electronic, optical and thermal sub-problems. It can be used to explore the inner working of a device and useful for the design of the laser devices including the active region. However such modelling is relatively time consuming as compared to the previously described models. Using such modelling, one can simulate the injection of carriers into the active region, carrier transport between different layers, current leakage around the active region, diode current-voltage characteristics, optical waveguide mode shape and its overlap with the gain region, and thermal effects. In this thesis, we have simulated such a laser based on multiple quantum wells and optimized the active region to help improve the carrier injection.

Semiconductor injection lasers usually employ vertical carrier injection (VCI) of both holes and electrons from the p and n-doped layers into the multiple quantum-well based active region to achieve population inversion and hence optical gain. An alternate approach is to inject carriers parallel to quantum well hetero-junctions and is called lateral current injection (LCI) scheme. We have also explored this scheme in order to find out an optimum device geometry to get uniform gain and carrier density in the active region.

In order to confirm the device simulation results, detailed device measurements are necessary to evaluate its real performance. We need to measure the material quality and the carrier lifetime of the grown quantum wells to determine their potential for lasing. This can be done by time-resolved photoluminescence (PL) measurements. A longer carrier lifetime indicates defect and impurity free crystal structure. A narrow and intense PL peak indicates good interface quality at the well-barrier hetero-junction interfaces. Moreover, if there are many quantum wells present in the active gain region, the carrier transport from one well to the next well is important both for static and dynamic properties of the laser. Time and wavelength resolved PL measurements can give us information about the carrier transport between the wells and can be helpful in designing the multiple quantum well active region. For semiconductor laser measurements, one can measure the light-current and current-voltage relationship of the laser diode at different temperatures. This gives information about the laser threshold current, threshold voltage, series resistance, electrical-to-optical conversion efficiency and high temperature performance. One can repeat such measurements for lasers with different cavity lengths, and get information about the laser internal loss and leakage current. One can measure optical gain of the laser waveguide as a function of the wavelength and the drive current. This measurement gives useful information about the lasing capability and efficiency of the active region. One can also do high speed microwave measurements to evaluate the laser modulation response. This gives information about the dynamic properties of a device and its capabilities both for analog and digital direct-modulation applications.

## 1.2 Thesis Organization

This thesis is based on the research papers that have either been published or submitted for review to different international research journals and reviewed conferences. The papers are also included at the end of the thesis. An introduction to the subjects covered and the motivation for the research done in this thesis is given in Chapter 1. Chapter 2 explains the numerical methods developed for optical waveguide simulation. A new finite difference method for optical mode solving is derived. A new Cascading and Doubling algorithm within the Method of Lines framework with full eigenvectors formulation is explained. This method is applied for non-paraxial bi-directional beam propagation through deep gratings. A new polarizing device based on anti-resonant waveguide grating structure is proposed and its polarizing properties are simulated.

In Chapter 3, we move to the active devices, that is semiconductor laser simulation. A brief theoretical background is given for the rate-equation model. Complete laser device simulation using drift-diffusion model is done to optimize the multiple quantum well based vertical injection as well as lateral injection laser.

In Chapter 4, thorough experimental evaluation of different multiple quantum well structures as well as Fabry-Perot and DBR lasers is performed. New strain balanced quantum wells based on InGaAsP compressive well and InGaAlAs tensile barrier are grown with a view to improve the carrier injection and optical gain in a MQW active region. Time and wavelength resolved PL measurements are done to measure the carrier transport through specially grown MQW test structures. Semi-insulating regrown Fabry-Perot lasers are fabricated and measured for optical gain, chirp, small-signal response and dc performance. High speed directly modulated DBR lasers are measured for analog performance. Digital transmission experiments at 40 Gb/s are also performed on these DBR lasers and error free operation is demonstrated for back to back and through 1 km standard single mode fiber link. This indicates the potential of the directly modulated DBR lasers for short distance high bitrate communication.

The thesis is concluded in Chapter 5 and some future research plans to further extend the device performance are highlighted. In Chapter 6, a brief summary of the original work done and the author's contribution to each publication is explained.

## Chapter 2

# Optical Waveguide Simulation

### 2.1 Introduction

In this chapter, a basic introduction to the optical mode structure in planar light waveguides is given. Method of Lines (MoL) is used as the numerical method applied to solve the wave equation both for mode calculation and for beam propagation. It is explained how the accuracy of the basic MoL can be increased by using higher-order approximations with appropriate boundary conditions. The need of absorbing boundary condition in the MoL at the termination of the problem space is highlighted. For beam propagation through discontinuities and gratings in a waveguide, a theoretical derivation is given for single and multiple discontinuities. Since there are many discontinuities along the beam propagation direction for a long grating, a new algorithm, called Cascading and Doubling algorithm, is used in the MoL framework which can model such gratings in less calculation steps. This algorithm is applied to model a deep grating and the results are compared with published results. At the end, a novel waveguide structure based on anti-resonant waveguide grating is used for polarization and spectral filtering applications. Its spectral response is simulated using the improved MoL algorithm. The results presented in this chapter culminate in the form of **Paper A, B and C**.

### 2.2 Three-Layer Dielectric Slab Waveguide

A three-layer dielectric slab waveguide is perhaps the simplest geometry for which, guided modes can be calculated analytically. We consider the lossless asymmetric dielectric slab shown in figure 2.1. We shall assume that  $n_1 > n_2 \geq n_3$  so that total internal reflection (TIR) can occur at each interface. Writing

Maxwell's equations in terms of the refractive index  $n_i$  ( $i = 1, 2, 3$ ) of the three layers and assuming that the material of each layer is non-magnetic and isotropic, that is  $\mu = \mu_o$  and  $\epsilon$  is a scalar, we have [35]:

$$\nabla \times \nabla \times \mathbf{E} = -\mu_o n_i^2 \epsilon_o \frac{\partial^2 \mathbf{E}}{\partial t^2} \quad (2.1)$$

To simplify further, we use the identity

$$\nabla \times \nabla \times \mathbf{A} = \nabla(\nabla \cdot \mathbf{A}) - \nabla^2 \mathbf{A} \quad (2.2)$$

where  $\mathbf{A}$  is any vector. We obtain:

$$\nabla^2 \mathbf{E} = \mu_o \epsilon_o n_i^2 \frac{\partial^2 \mathbf{E}}{\partial t^2} \quad (2.3)$$

Writing the last equation in phasor notation ( assuming a time-harmonic field of the form  $e^{-j\omega t}$  ) we obtain [35]:

$$\nabla^2 \mathbf{E} + k_o^2 n_i^2 \mathbf{E} = 0 \quad (2.4)$$

which is the familiar vector wave equation for a uniform dielectric with refractive index  $n_i$ . Here  $k_o$  is the free-space wavenumber given by  $k_o = \omega \sqrt{\mu_o \epsilon_o}$ . The electric field vector  $\mathbf{E}$  in equation 2.4 is now complex having both magnitude and phase. Assuming that the structure is uniform in the  $y$ -direction and extends to infinity, that is  $\frac{\partial}{\partial y} = 0$ . If we further assume a  $z$ -dependence of the form  $e^{j\beta z}$ , with  $\beta$  as the longitudinal propagation constant, equation 2.4 may be written for the three regions of the guide as follows [35]:

$$\frac{d^2 \mathbf{E}_1}{dx^2} + q^2 \mathbf{E}_1 = 0 \quad , \quad -2a \leq x \leq 0 \quad (2.5)$$

$$\frac{d^2 \mathbf{E}_2}{dx^2} - p^2 \mathbf{E}_2 = 0 \quad , \quad x \leq -2a \quad (2.6)$$

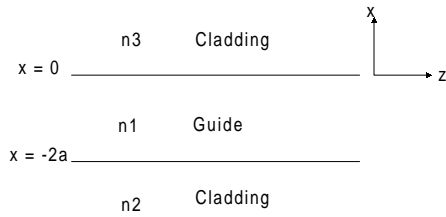


**Figure 2.1.** Three layer slab waveguide, 2-D view

$$\frac{d^2 \mathbf{E}_3}{dx^2} - r^2 \mathbf{E}_3 = 0, \quad x \geq 0 \quad (2.7)$$

where  $q^2 = n_1^2 k_o^2 - \beta^2$ ,  $p^2 = \beta^2 - n_2^2 k_o^2$  and  $r^2 = \beta^2 - n_3^2 k_o^2$ . Similar forms of the wave equation in the three regions may easily be derived for the magnetic field  $\mathbf{H}$  from Maxwell's equations.

### Transverse Electric (TE) Guided Modes

Our assumption  $\frac{\partial}{\partial y} = 0$  implies that the only non-zero field components for  $TE$  modes are  $E_y$ ,  $H_x$  and  $H_z$  [35]. From Maxwell's equations [35] we get:

$$H_x = -\frac{\beta}{\omega \mu_o} E_y \quad (2.8)$$

$$H_z = -\frac{j}{\omega \mu_o} \frac{\partial E_y}{\partial x} \quad (2.9)$$

Equations 2.8 and 2.9 express two nonzero magnetic field components in terms of the single nonzero electric field component  $E_y$ , which itself is given by the solution of the wave equations in each region. The other requirements to be satisfied by these field components is that the tangential components  $E_y$  and  $H_z$  should be continuous at the  $n_1 - n_2$  and  $n_1 - n_3$  interfaces of the dielectric waveguide. For the guided modes, we require that the power to be confined largely to the central region of the guide and no power escapes from the structure. The form of equations 2.5, 2.6 and 2.7 then implies that this requirement will be satisfied for an oscillatory solution in the middle region ( $q^2 \geq 0$ ) with evanescent tails in the top and bottom cladding regions ( $r^2, p^2 \geq 0$ ). Thus, the solution of  $E_y$  in the three regions for the guided modes is [35]:

$$E_y = \begin{cases} Ae^{-rx} & , x \geq 0 \\ A \cos(qx) + B \sin(qx) & , 0 \geq x \geq -2a \\ (A \cos(2aq) - B \sin(2aq)) e^{p(x+2a)} & , x \leq -2a \end{cases} \quad (2.10)$$

The form of equation has been chosen so that the requirement of the continuity of  $E_y$  at  $x = 0$  and  $x = -2a$  is automatically satisfied. To complete the boundary requirements, it remains to ensure continuity of  $H_z$ . This component is given by:

$$H_z = \frac{-j}{\omega \mu_o} \begin{cases} -rAe^{-rx} & , x \geq 0 \\ q(-A \sin(qx) + B \cos(qx)) & , 0 \geq x \geq -2a \\ p(A \cos(2aq) - B \sin(2aq)) e^{p(x+2a)} & , x \leq -2a \end{cases} \quad (2.11)$$

The continuity condition yields two equations. One at  $x = 0$  and the second at  $x = -2a$ , that is:

$$-rA = qB \quad (2.12)$$

and

$$q(A \sin(2aq) + B \cos(2aq)) = p(A \cos(2aq) - B \sin(2aq)) \quad (2.13)$$

Eliminating the ratio  $A/B$  from these equations yields [35]:

$$\tan(2aq) = \frac{q(p+r)}{q^2 - pr} \quad (2.14)$$

This is the eigenvalue equation for the  $TE$  modes of asymmetric slab waveguide. It can be shown that only certain discrete values of  $\beta$  can satisfy it, so this guide will only *support* a discrete set of guided modes with no power loss factor. The  $\beta$  can be found from this equation using numerical or graphical methods.

### Transverse Magnetic (TM) Guided Modes

For this polarization, the only non-zero field components are  $H_y$ ,  $E_x$  and  $E_z$  [35]. Also from Maxwell's equations, we have:

$$E_x = \frac{\beta}{\omega n_i^2 \epsilon_o} H_y \quad (2.15)$$

$$E_z = \frac{j}{\omega n_i^2 \epsilon_o} \frac{\partial H_y}{\partial x} \quad (2.16)$$

These equations relate the electric field components  $E_x$  and  $E_z$  to the only nonzero magnetic field component  $H_y$  which itself is a solution of wave equations in the three regions. The solution of the  $H_y$  may be written as [35]:

$$H_y = \begin{cases} C e^{-rx} & , x \geq 0 \\ C \cos(qx) + D \sin(qx) & , 0 \geq x \geq -2a \\ (C \cos(2aq) - D \sin(2aq)) e^{p(x+2a)} & , x \leq -2a \end{cases} \quad (2.17)$$

and  $E_z$  is given by:

$$E_z = \frac{j}{\omega \epsilon_o} \begin{cases} -\frac{rC}{n_3^2} e^{-rx} & , x \geq 0 \\ \frac{q}{n_1^2} (-C \sin(qx) + D \cos(qx)) & , 0 \geq x \geq -2a \\ \frac{p}{n_2^2} (C \cos(2aq) - D \sin(2aq)) e^{p(x+2a)} & , x \leq -2a \end{cases} \quad (2.18)$$

continuity of  $E_z$  at  $x = 0$  and  $x = -2a$  gives:

$$-\frac{rC}{n_3^2} = \frac{qD}{n_1^2} \quad (2.19)$$

and

$$\frac{q}{n_1^2} (C \sin(2aq) + D \cos(2aq)) = \frac{p}{n_2^2} (C \cos(2aq) - D \sin(2aq)) \quad (2.20)$$



Eliminating the ratio  $C/D$  from these equation results in [35]:

$$\tan(2aq) = \frac{qn_1^2(n_3^2p + n_2^2r)}{n_2^3n_3^2q^2 - n_1^4pr} \quad (2.21)$$

which is the eigenvalue equation for the  $TM$  modes of a slab waveguide.

### Other Types of Modes

The modal solutions found so far are descriptive of the light confined inside the guide. However, further solutions should exist to account for the light propagation *outside* the guide. These are known as radiation modes and they correspond to leakage of energy from the guide into the open space [36]. We solved equations 2.5, 2.6 and 2.7 to find the  $TE$  modes of a slab waveguide. This is a general second-order differential equation, which can be written in the form:

$$\frac{d^2 E_i}{dx^2} + C_i^2 E_i = 0 \quad (2.22)$$

In our previous analysis the form of the solution was exponential or sinusoidal, depending upon the *sign* of the term  $C_i^2 = n_i^2 k_o^2 - \beta^2$ . If we consider all possible values of  $\beta$ , it turns out that a wider range of solutions can be found. If we again take  $n_1 > n_2 \geq n_3$ , the complete set can be represented as a diagram in  $\beta$ -space [36] as shown in figure 2.2. The essential features of the diagram are [36]:

1. For  $\beta > k_o n_1$ , the solutions are exponential in all three layers. Since this implies infinite field amplitudes at large distances from the guide, these are unrealistic solutions.
2. For  $k_o n_1 > \beta > k_o n_2$ , there are a discrete number of bound or *guided modes*, which are the solutions already found. They vary sinusoidally inside the guide core and decay exponentially outside the guide.
3. For  $k_o n_2 > \beta > k_o n_3$ , the solutions vary exponentially in the top layer and sinusoidally in both the guide and bottom layer. Since these fully penetrate the bottom layer, they are called *substrate modes*. Any value of  $\beta$  is allowed between the two limits given above, so the set forms a continuum.
4. For  $k_o n_3 > \beta$ , solutions vary sinusoidally in all three layers. These particular field patterns are known as *radiation modes*. Once again any value of  $\beta$  is allowed in the range above, so the set forms another continuum.

## 2.3 Method of Lines

Method of Lines (MoL) is a semi-analytical technique for the solution of partial differential equations (PDE). All independent variables are discretized except one

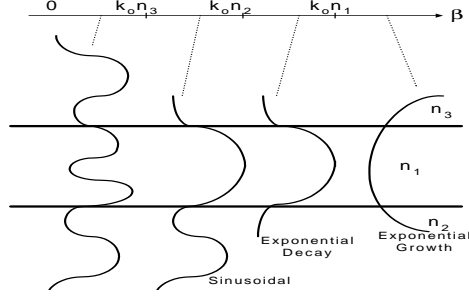


**Figure 2.2.** Modal solutions represented in the  $\beta$ -Space

and thus, the partial differential equation is transformed into a set of ordinary differential equations (ODE) which can be solved analytically [17]. This results in a higher numerical accuracy, less computational time and smaller memory requirements as compared to fully-discretizing finite-difference techniques. This method can account for the backwards-reflected field from longitudinally inhomogeneous structures such as waveguide junctions and gratings. It has been applied to model integrated optical and microwave waveguide problems for stationary analysis as well as for beam-propagation [18–22, 37].

### 2.3.1 Basic 3-Point Formulation of the MoL

Consider the two-dimensional wave equation:

$$\frac{\partial^2 \psi(x, z)}{\partial x^2} + \frac{\partial^2 \psi(x, z)}{\partial z^2} + k_o^2 n^2(x) \psi(x, z) = 0 \quad (2.23)$$

Here both the field  $\psi(x, z)$  and the refractive index  $n(x)$  are discretized along the  $x$ -axis. At the  $i$ th grid, the  $\partial^2/\partial x^2$  term in equation 2.23 is replaced by a three-point central difference approximation of the form:

$$\frac{\partial^2 \psi_i(z)}{\partial x^2} \approx \frac{\psi_{i+1}(z) - 2\psi_i(z) + \psi_{i-1}(z)}{(\Delta x)^2} \quad (2.24)$$

When this equation is applied at each of the  $M$  discrete grid points of the problem space as shown in figure 2.3(a), we obtain  $M$  distinct equations, which can be put together in a single matrix equation of the form:

$$\frac{1}{(\Delta x)^2} C \Psi + \frac{d^2}{dz^2} \Psi + k_o^2 N \Psi = 0 \quad (2.25)$$

where  $C$  is a tri-diagonal second-order central-difference matrix,  $N$  is a diagonal matrix containing the discretized values of  $n^2(x)$ , and  $\Psi$  is a column vector

containing the discretized field values. The above equation may then be written in the simplified form:

$$\frac{d^2}{dz^2}\Psi + Q\Psi = 0 \quad (2.26)$$

where

$$Q = \frac{1}{(\Delta x)^2}C + k_o^2 N \quad (2.27)$$

The solution of this 2nd-order ordinary matrix differential equation is formally given by [19]:

$$\Psi = e^{+j\sqrt{Q}z}A + e^{-j\sqrt{Q}z}B \quad (2.28)$$

where  $e^{+j\sqrt{Q}z}$  represents field propagation in the  $+z$  direction and  $e^{-j\sqrt{Q}z}$  represents field propagation in  $-z$  direction. The matrices  $e^{+j\sqrt{Q}z}$  and  $e^{-j\sqrt{Q}z}$  are calculated by diagonalizing matrix  $Q$ , such that  $Q = T\Lambda T^{-1}$  where  $T$  is a matrix containing the eigenvectors of  $Q$  and  $\Lambda$  is a diagonal matrix containing the eigenvalues of  $Q$ .

### 2.3.2 Interface Conditions

In order to correctly model the electric and magnetic fields behavior at an interface, the interface conditions (I.Cs.) should be appropriately accounted for in the Method of Lines formulation. We are mainly concerned with multi-layer structures in which the material properties are constant within each layer and change *abruptly* from one layer to the next. Depending upon the polarization of the field,  $\psi$  may represent either  $E_y$  for the  $TE$  polarization or  $H_y$  for the  $TM$  polarization. At an index discontinuity in the transverse direction  $x$ ,  $\psi$  is continuous. However, all its higher order derivatives with respect to  $x$ , i.e.  $\psi^{(n)}$  are in general discontinuous there. With reference to figure 2.3(b), where an index discontinuity is assumed at  $x = 0$ , the discontinuities in  $\psi^{(n)}$  can easily be deduced from the wave equation, and are summarized below:

$$\psi_{0+} = \psi_{0-} = \psi_0 \quad (2.29)$$

$$\psi_{0+}^{(1)} = \rho_{21}\psi_{0-}^{(1)} \quad (2.30)$$

$$\psi_{0+}^{(2)} = \psi_{0-}^{(2)} + \zeta_{12}\psi_0 \quad (2.31)$$

$$\psi_{0+}^{(3)} = \rho_{21} \left( \psi_{0-}^{(3)} + \zeta_{12}\psi_{0-}^{(1)} \right) \quad (2.32)$$

$$\psi_{0+}^{(4)} = \psi_{0-}^{(4)} + 2\zeta_{12}\psi_{0-}^{(2)} + \zeta_{12}^2\psi_0 \quad (2.33)$$

where  $\zeta_{12} = k_o^2(n_1^2 - n_2^2)$ ,  $\rho_{21} = n_2^2/n_1^2$  for the  $TM$  case and  $\rho_{21} = 1$  for the  $TE$  case. The subscripts  $0^+$  and  $0^-$  represent the field immediately to the right and to the left of the interface, respectively.

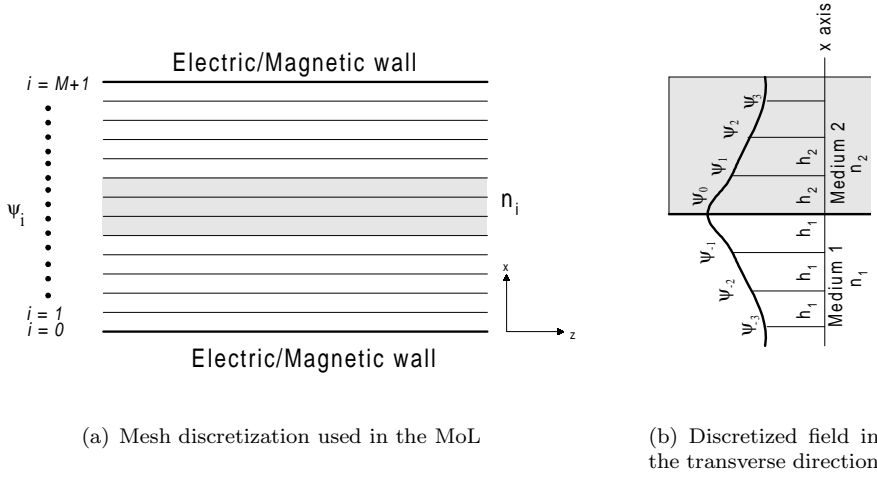


**Figure 2.3.** Mesh and field sampling

### 2.3.3 Improved 3-Point Formulation with Interface Conditions

Within a certain layer, the refractive index and mesh size are uniform. From one layer to the next, either the refractive index or the mesh size or both may change abruptly. With reference to figure 2.3(b), the field on either side of the interface is expanded in terms of the field at the interface using Taylor's series expansion, that is:

$$\psi_{-1} = \psi_{0-} - h_1 \psi_{0-}^{(1)} + \frac{h_1^2}{2!} \psi_{0-}^{(2)} + \dots \quad (2.34)$$

$$\psi_{+1} = \psi_{0+} + h_2 \psi_{0+}^{(1)} + \frac{h_2^2}{2!} \psi_{0+}^{(2)} + \dots \quad (2.35)$$

Here  $\psi_{0+}$  and  $\psi_{0-}$  represent the field at  $x = 0^+$  and  $x = 0^-$  respectively. Using the interface conditions 2.29, 2.30 and 2.31 to substitute for all  $\psi_{0+}^{(n)}$  in terms of  $\psi_{0-}^{(n)}$  in equation 2.35, we obtain:

$$\psi_{+1} = (1 + 0.5h_2^2\zeta_{12})\psi_{0-} + h_2\rho_{21}\psi_{0-}^{(1)} + 0.5h_2^2\psi_{0-}^{(2)} + \dots \quad (2.36)$$

eliminating  $\psi_{0-}^{(1)}$  from equations 2.36 and 2.34, we obtain:

$$\psi_{0-}^{(2)} \approx \frac{\psi_{+1} - (\tau_{21}\rho_{21} + 1 + 0.5h_2^2\zeta_{12})\psi_{0-} + \tau_{21}\rho_{21}\psi_{-1}}{0.5h_2(h_1\rho_{21} + h_2)} \quad (2.37)$$

where  $\tau_{21} = h_2/h_1$ . This relation can be used to approximate the  $\partial^2/\partial x^2$  operator immediately to the left of a sampling point  $i$ , that is at  $i^-$ , in terms of

the field values at  $i + 1$ ,  $i$  and  $i - 1$  with the inclusion of appropriate interface conditions.

### 2.3.4 Higher-Order Formulation with Interface Conditions

We can improve the numerical accuracy of the algorithm by using higher-order finite-difference approximations in the derivation. In the case of 5-point approximation, we account for two more terms in the Taylor's series expansion of equations 2.34 and 2.35, and also include one more sampling point on either side of the interface in the derivation. Similarly, a 7-point approximation can be derived. In **Paper A**, such a derivation is explained. Moreover, a high-contrast waveguide ( $TE$  and  $TM$  modes) and a metal-dielectric surface plasmon  $TM$  mode is simulated and the improved numerical accuracy of the new finite-difference approximation schemes is demonstrated.

## 2.4 Perfectly Matched Layer (PML) Absorber

In order to model *free space* at the boundaries of the problem space, absorbing boundary conditions are required to terminate the problem space. If we use electric/magnetic wall boundary condition with either  $E_y = 0$  or  $H_y = 0$ , it will reflect back the radiative waves into the problem space and hence corrupt the computed results. The use of an appropriate numerical absorbing boundary conditions in the finite-difference simulation of wave equation in an open space region is necessary because it will limit the computational domain width and absorb the outgoing waves.

The PML absorbing scheme based on complex distance approach was first incorporated into the MoL in reference [38]. It has been shown in the literature that the PML can absorb propagating waves over a wide range of incident angles [38] and the reflected field is extremely small. The absorption of the *radiative* wave is done by changing the distance  $x$  from *real* to *imaginary*. This introduces an numerical attenuation factor in the radiative field and hence causes decay of the radiative field in the PML region. The last mesh point is terminated by an electric/magnetic wall boundary condition. The *real* distance is transformed to a *complex* one according to:

$$x \rightarrow x(1 + j\sigma) \quad (2.38)$$

$$dx \rightarrow dx(1 + j\sigma) \quad (2.39)$$

here  $\sigma$  is the decay-factor constant. The wave  $e^{+jkx}$  propagating in  $+x$  direction in the real space will be converted to

$$e^{+jkx(1+j\sigma)} = e^{+jkx} e^{-k\sigma x} \quad (2.40)$$

in the complex space. The factor  $e^{-k\sigma x}$  causes the decay of the field in the  $+x$  direction in the complex space. The value of  $\sigma$  is set arbitrarily and the number

of samples in the PML absorber is chosen to cause a significant decay in the field so that it is not reflected by the electric/magnetic wall.

In **Paper B** and **Paper C**, the PML absorbing layer is used to terminate the mesh space and absorb outgoing radiation waves. Its effectiveness is demonstrated by the correctness of the calculated deep grating spectrum in **Paper B**, and by the accurate calculation of the imaginary part of the propagation constant of a leaky waveguide structure in **Paper C**.

## 2.5 Simulation of Discontinuities

### 2.5.1 A Single Discontinuity

Previous analysis deals with stationary MoL which can be used to find the modal shape and propagation constants of a multilayer waveguide. Now we move to the problem of bi-directional beam propagation and wave reflection from waveguide junctions and discontinuities. With reference to figure 2.4(a), the problem space is divided into two regions, region (0) and region (1). The field is incident from region (0). After reflection from the discontinuity, there is a reflected field in region (0) and a transmitted field in region (1). The total field in each region is the sum of the forward and the backward traveling field:

$$\Psi_0 = e^{+jS_0z} A_0 + e^{-jS_0z} B_0 \quad (2.41)$$

$$\Psi_1 = e^{+jS_1z} A_1 \quad (2.42)$$

where  $\Psi$  is a column vector representing the field at the sample points,  $A_0$ ,  $B_0$ ,  $A_1$  are constant vectors,  $S = \sqrt{Q}$  and  $Q$  is defined before. For *TM* polarization,  $\Psi$  is continuous at the interface at  $z = 0$ , thus  $\Psi_0|_{z=0} = \Psi_1|_{z=0}$ . From equation 2.41

$$A_0 + B_0 = A_1 \quad (2.43)$$

from the interface condition equations, at the *i*th discretization line, the field on either side of the discontinuity at  $z = 0$  is related by

$$\frac{\psi'_{iz-}}{n_{iz-}^2} = \frac{\psi'_{iz+}}{n_{iz+}^2} \quad (2.44)$$

The *prime* superscript represents derivative with respect to  $z$ , normal to the interface. For all the discretization lines, the set of equations 2.44 can be put together in one matrix equation of the form:

$$N_0^{-1} \Psi'_0 = (N_1)^{-1} \Psi'_1 \quad (2.45)$$

where the matrix  $N$  is a diagonal matrix of refractive index squared  $n_i^2$  at each sample point. From equation 2.41, differentiating with respect to  $z$ , we have:

$$\Psi'_0 = jS_0 e^{jS_0z} A_0 - jS_0 e^{-jS_0z} B_0 \quad (2.46)$$

at the interface:

$$\Psi'_0|_{z=0} = jS_0(A_0 - B_0) \quad (2.47)$$

similarly:

$$\Psi'_1|_{z=0} = jS_1A_1 \quad (2.48)$$

substitute the last two equations in equation 2.45, and simplifying:

$$(N_0)^{-1}S_0(A_0 - B_0) = (N_1)^{-1}S_1A_1 \quad (2.49)$$

$$(A_0 - B_0) = S_0^{-1}(N_0)(N_1)^{-1}S_1A_1 \quad (2.50)$$

Eliminating  $B_0$  and simplifying, we get the transmitted field  $A_1$  in terms of  $A_0$ :

$$A_1 = 2(I + S_0^{-1}N_0N_1^{-1}S_1)^{-1}A_0 \quad (2.51)$$

Eliminating  $A_0$  and simplifying, we get the reflected field at  $z = 0$ :

$$B_0 = (I - S_0^{-1}N_0N_1^{-1}S_1)(I + S_0^{-1}N_0N_1^{-1}S_1)^{-1}A_0 \quad (2.52)$$

For the *TE* polarization, both field and its  $z$  derivatives are continuous across an interface. Following a similar procedure, we derive the *Transmission* and *Reflection* matrices for the *TE* case.

$$A_1 = 2(I + S_0^{-1}S_1)^{-1}A_0 \quad (2.53)$$

$$B_0 = (I - S_0^{-1}S_1)(I + S_0^{-1}S_1)^{-1}A_0 \quad (2.54)$$

where the last two equations were obtained from equation 2.51 and 2.52 by replacing  $N_0$  and  $N_1$  by the identity matrix  $I$ . The transmission matrix  $T$  and the reflection matrix  $R$  are related by:

$$A_1 = B_0 + A_0 \quad (2.55)$$

$$= RA_0 + A_0 = TA_0 \quad (2.56)$$

### 2.5.2 A Double Discontinuity

Refer to figure 2.4(b), the problem space is divided into three regions. In general, the total field in each regions is composed of the forward traveling field  $e^{+jSz}$  and the backward traveling field  $e^{-jSz}$ .

$$\Psi_0 = e^{+jS_0z}A_0 + e^{-jS_0z}B_0 \quad (2.57)$$

$$\Psi_1 = e^{+jS_1z}A_1 + e^{-jS_1(z-d)}B_1 \quad (2.58)$$

$$\Psi_2 = e^{+jS_2(z-d)}A_2 \quad (2.59)$$

Note that this particular form of equations 2.58 and 2.59 is chosen to avoid numerical instabilities in the MoL. An alternate form of equation 2.58, that

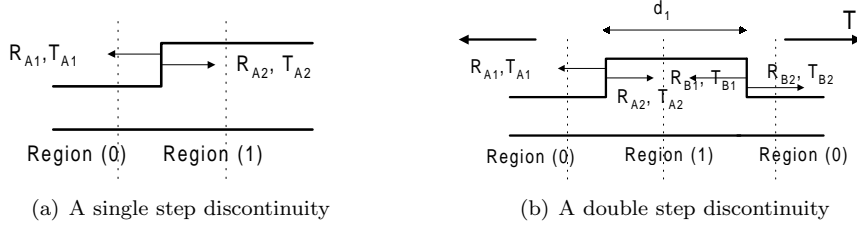


**Figure 2.4.** A single and double waveguide discontinuity

is  $\Psi_1 = e^{+jS_1z}A_1 + e^{-jS_1z}B_1$ , may also be chosen. This results in a factor  $(e^{jS_1d})^{-1}$  in the resulting formulas. Unfortunately, this factor turns out to be ill-conditioned or singular during simulation and its inverse can not be calculated. Applying the interface conditions at  $z = 0$ , at  $z = d$  and simplifying, we end up with four equations with five unknowns  $A_0$ ,  $B_0$ ,  $A_1$ ,  $B_1$  and  $A_2$ . We can solve for the unknowns in terms of the incident field  $A_0$ . The procedure is similar to that followed in the single discontinuity section. The final results are:

$$A_2 = (I + T_2)^{-1}T_2e^{+jS_1d}K_4A_0 \quad (2.60)$$

$$B_0 = K_3A_0 \quad (2.61)$$

where:

$$K_4 = (I + T_1) + (I - T_1)K_3, \text{ and} \quad (2.62)$$

$$K_3 = (S_1 + S_2)^{-1}(S_2 - S_1) \quad (2.63)$$

The results for the *TM* polarization are similar but with  $T_1 = S_1^{-1}N_1N_0^{-1}S_0$  and  $T_2 = S_2^{-1}N_2N_1^{-1}S_1$ .

### 2.5.3 Multiple Discontinuities

Consider the multi-layer structure in figure 2.5. The total field in each layer is the sum of the forward and the backward traveling wave, that is:

$$\Psi_0 = e^{+jS_0z}A_0 + e^{-jS_0z}B_0 \quad (2.64)$$

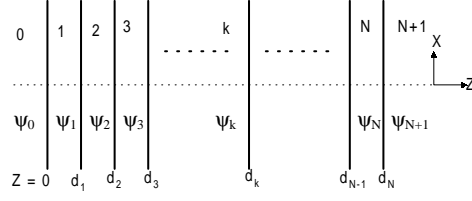
$$\Psi_1 = e^{+jS_1z}A_1 + e^{-jS_1(z-d_1)}B_1 \quad (2.65)$$

$\vdots$

$$\Psi_k = e^{+jS_k(z-d_{k-1})}A_k + e^{-jS_k(z-d_k)}B_k \quad (2.66)$$

$\vdots$



**Figure 2.5.** Multiple waveguide discontinuities

$$\Psi_{N+1} = e^{+jS_{N+1}(z-d_N)} A_{N+1} \quad (2.67)$$

The wave is incident on the interface  $z = 0$  from the left. In the region  $N + 1$ , the wave is assumed to propagate without reflection in the  $+z$  direction. At each discontinuity, the boundary condition requires the continuity of the tangential field  $E_y$  and  $H_x$ . In other words, the continuity of  $\Psi$  and  $\frac{d\Psi}{dz}$  must be satisfied. Application of these conditions results in the following recursive relationship [37]:

$$e^{jS_k(d_k-d_{k-1})} A_k = \frac{1}{2}(I + S_k^{-1}S_{k+1})A_{k+1} + \frac{1}{2}(I - S_k^{-1}S_{k+1})e^{jS_{k+1}(d_{k+1}-d_k)} B_{k+1} \quad (2.68)$$

$$B_k = \frac{1}{2}(I - S_k^{-1}S_{k+1})A_{k+1} + \frac{1}{2}(I + S_k^{-1}S_{k+1})e^{jS_{k+1}(d_{k+1}-d_k)} B_{k+1} \quad (2.69)$$

where  $k = 0, 1, 2, \dots, N$ , For  $k = 0$ ,  $d_0 = d_{-1} = 0$  and for  $k = N$ ,  $B_{N+1} = 0$ . This is a recursive relationship which express the field in layer  $k$  in terms of the field in layer  $k + 1$ . We start from the last layer, in which there is only a forward propagating wave, and work backwards, layer by layer, until we reach the first layer. Thus the field in the last layer is expressed in terms of the field in the first layer. From this, we can find the reflection and transmission matrices and hence the reflected and transmitted fields.

## 2.6 Cascading and Doubling Algorithm

To model a long waveguide grating with deep corrugations, a fast and stable algorithm is developed within the Method of Lines framework in **Paper B**. It works by finding the *equivalent* reflection and transmission coefficient matrices of a discontinuity structure and then, duplicating it to find the equivalent reflection

and transmission matrices of two such discontinuities attached together. For  $N$  discretization lines in the problem space, this algorithm works on an  $N^2$  matrix for storage and eigen-value calculation. Some other algorithms [6, 8] based on raising a matrix to a certain power to model a certain number of periods, operate upon  $(2N)^2$  matrices. This algorithm is found to be stable and its accuracy is verified against published results.

### 2.6.1 Theory

With reference to figure 2.6, two waveguide regions ‘A’ and ‘B’ are attached together. Their individual reflection and transmission matrices are assumed to be known. We will next develop the scheme to find the reflection and transmission matrices of the combined structure.  $R_A$  and  $T_A$  are reflection and transmission matrices of the isolated structure ‘A’. For an asymmetrical region,  $R_{A1} \neq R_{A2}$  and  $T_{A1} \neq T_{A2}$ .  $R_{A1}, T_{A2}$  ( $R_{A2}, T_{A1}$ ) are the reflection and transmission matrices of the discontinuity ‘A’ when the field is incident from left(right) of the discontinuity. The same comments apply to region ‘B’. If the two regions are not identical then  $R_A \neq R_B$  and  $T_A \neq T_B$ . The reflection and transmission matrices of the combined structure are denoted by  $R_{01}$  and  $T_{02}$  respectively when the field is incident from the left. These matrices are obtained by adding the successive reflections and transmissions as the two structures interact. The field propagation in the unperturbed waveguide section of length  $d$  is described by  $e^{\pm jSz}$  [39] and  $S$  is defined before.  $e^{+jSz}$  represents a wave propagating in the  $+z$  direction since a time-variation of the form  $e^{-j\omega t}$  is assumed. The field vector  $a_0$  is assumed to be incident from the left on the first discontinuity (see figure 2.7). We can express the net reflected field in terms of the summation of forward and backwards traveling waves after multiple reflections from the two discontinuities.

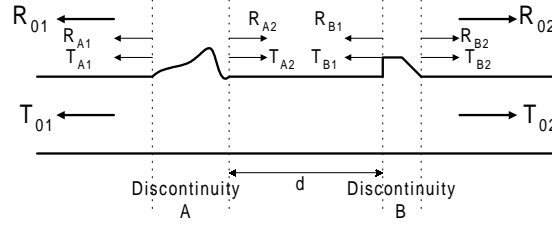


**Figure 2.6.** Two waveguide structures cascaded together

$$\begin{aligned}
 R_{01}a_0 = & R_{A1}a_0 + T_{A1}e^{jSd}R_{B1}e^{jSd}T_{A2}a_0 + \\
 & T_{A1}(e^{jSd}R_{B1}e^{jSd}R_{A2})e^{jSd}R_{B1}e^{jSd}T_{A2}a_0 + \\
 & T_{A1}(e^{jSd}R_{B1}e^{jSd}R_{A2})^2e^{jSd}R_{B1}e^{jSd}T_{A2}a_0 + \\
 & T_{A1}(e^{jSd}R_{B1}e^{jSd}R_{A2})^3e^{jSd}R_{B1}e^{jSd}T_{A2}a_0 + \dots
 \end{aligned} \tag{2.70}$$

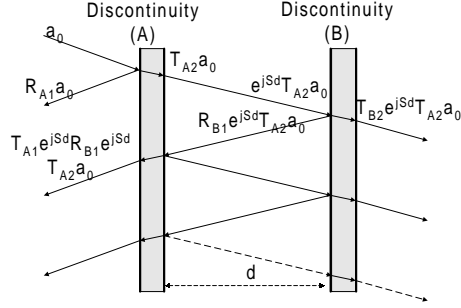


**Figure 2.7.** Multiple reflections from two cascaded regions

$$R_{01} = R_{A1} + T_{A1}e^{jSd}R_{B1} \left[ \sum_{n=0}^{\infty} (e^{jSd}R_{A2}e^{jSd}R_{B1})^n \right] e^{jSd}T_{A2} \quad (2.71)$$

$$R_{01} = R_{A1} + T_{A1}e^{jSd}R_{B1} (I - e^{jSd}R_{A2}e^{jSd}R_{B1})^{-1} e^{jSd}T_{A2} \quad (2.72)$$

where the infinite geometric series in 2.72 is assumed to be convergent and is replaced by an equivalent quotient term. The transmission matrix  $T_0$  of the combined structure is obtained in a similar fashion.

$$T_{02}a_0 = T_{B2}e^{jSd}T_{A2}a_0 + T_{B2}(e^{jSd}R_{A2}e^{jSd}R_{B1})a_0 + T_{B2}(e^{jSd}R_{A2}e^{jSd}R_{B1})^2 e^{jSd}T_{A2}a_0 + \dots \quad (2.73)$$

$$T_{02}a_0 = T_{B2} \left[ \sum_{n=0}^{\infty} (e^{jSd}R_{A2}e^{jSd}R_{B1})^n \right] e^{jSd}T_{A2}a_0 \quad (2.74)$$

$$T_{02} = T_{B2} (I - e^{jSd}R_{A2}e^{jSd}R_{B1})^{-1} e^{jSd}T_{A2} \quad (2.75)$$

Equations 2.75 and 2.72 are very similar to each other with a common quotient factor  $(I - e^{jSd}R_{A2}e^{jSd}R_{B1})^{-1}e^{jSd}T_{A2}$ . These formulas give net reflection and transmission matrices of a cascaded structure composed of two sub-structures in terms of their individual reflection and transmission matrices. The relations for  $R_{02}$  and  $T_{01}$  as seen from the right are easily obtained from equations 2.75 and 2.72 by interchanging  $A \rightleftharpoons B$  and  $1 \rightleftharpoons 2$ . That is:

$$R_{02} = R_{B2} + T_{B2}e^{jSd}R_{A2} (I - e^{jSd}R_{B1}e^{jSd}R_{A2})^{-1} e^{jSd}T_{B1} \quad (2.76)$$

$$T_{01} = T_{A1} (I - e^{jSd}R_{B1}e^{jSd}R_{A2})^{-1} e^{jSd}T_{B1} \quad (2.77)$$

### 2.6.2 Symmetrical and Identical Structures

If each of the structures 'A' and 'B' are symmetrical then  $R_1 = R_2 = R$  and  $T_1 = T_2 = T$ . Thus equations 2.75 and 2.72 reduce to:

$$R_{01} = R_A + T_Ae^{jSd}R_B (I - e^{jSd}R_Ae^{jSd}R_B)^{-1} e^{jSd}T_A \quad (2.78)$$

$$T_{02} = T_B (I - e^{jSd} R_A e^{jSd} R_B)^{-1} e^{jSd} T_A \quad (2.79)$$

If the symmetric structures ‘A’ and ‘B’ are also identical, then  $R_A = R_B$  and  $T_A = T_B$ . So the relations are further simplified to:

$$R_{01} = R + T e^{jSd} R (I - e^{jSd} R e^{jSd} R)^{-1} e^{jSd} T \quad (2.80)$$

$$T_{02} = T (I - e^{jSd} R e^{jSd} R)^{-1} e^{jSd} T \quad (2.81)$$

If two symmetric and identical structures are connected to each other directly, such that  $d = 0$ , then:

$$R_{01} = R + T R (I - R^2)^{-1} T \quad (2.82)$$

$$T_{02} = T (I - R^2)^{-1} T \quad (2.83)$$

### 2.6.3 Case Study: Uniform Rectangular Grating

The rectangular grating is a classic example of a symmetrical periodic structure. This problem can be solved by considering the first discontinuity as shown in figure 2.4(a). The reflection matrix for the *TM* polarized field is given by:

$$R_{A1} = [I - S_0^{-1} N_0 N_1^{-1} S_1] [I + S_0^{-1} N_0 N_1^{-1} S_1]^{-1} \quad (2.84)$$

$$= \left[ (S_0^{-1} N_0 N_1^{-1} S_1)^{-1} - I \right] S_0^{-1} N_0 N_1^{-1} S_1 \cdot \left[ \left( (S_0^{-1} N_0 N_1^{-1} S_1)^{-1} + I \right) S_0^{-1} N_0 N_1^{-1} S_1 \right]^{-1} \quad (2.85)$$

$$= \left[ (S_0^{-1} N_0 N_1^{-1} S_1)^{-1} - I \right] S_0^{-1} N_0 N_1^{-1} S_1 \cdot (S_0^{-1} N_0 N_1^{-1} S_1)^{-1} \left[ (S_0^{-1} N_0 N_1^{-1} S_1)^{-1} + I \right]^{-1} \quad (2.86)$$

$$= \left[ (S_0^{-1} N_0 N_1^{-1} S_1)^{-1} - I \right] \left[ (S_0^{-1} N_0 N_1^{-1} S_1)^{-1} + I \right]^{-1} \quad (2.87)$$

$$= - \left[ I - (S_0^{-1} N_0 N_1^{-1} S_1)^{-1} \right] \left[ I + (S_0^{-1} N_0 N_1^{-1} S_1)^{-1} \right]^{-1} \quad (2.88)$$

$$= - \left[ I - S_1^{-1} N_1 N_0^{-1} S_0 \right] \left[ I + S_1^{-1} N_1 N_0^{-1} S_0 \right]^{-1} \quad (2.89)$$

$$= -R_{A2} \quad (2.90)$$

where  $N$  is a diagonal matrix of relative permittivity values sampled at the mesh points. Thus for the above case  $R_{A1} = -R_{A2}$ ,  $T_{A2} = I + R_{A1}$  and  $T_{A1} = I + R_{A2}$  [39]. For the *TE* mode, the matrices  $N_0$  and  $N_1$  are replaced by the identity matrix  $I$ . These equations are valid for both *TE* and *TM* cases. The next step is to treat the double discontinuity shown in figure 2.4(b). All  $R$ s and  $T$ s appearing in figure 2.4(b) can be expressed in terms of  $R_{A1}$ .

$$R_{A2} = -R_{A1} \quad (2.91)$$

$$T_{A1} = I + R_{A2} = I - R_{A1} \quad (2.92)$$

$$T_{A2} = I + R_{A1} \quad (2.93)$$

$$R_{B1} = R_{A2} = -R_{A1} \quad (2.94)$$

$$R_{B2} = R_{A1} \quad (2.95)$$

$$T_{B1} = T_{A2} = I + R_{A1} \quad (2.96)$$

$$T_{B2} = T_{A1} = I - R_{A1} \quad (2.97)$$

Since the structure of figure 2.4(b) is symmetric, we need only to define  $R$  and  $T$  for the structure. Using equations 2.75 and 2.72 we obtain:

$$R = R_{A1} + (I - R_{A1}) e^{jS_1 d_1} (-R_{A1}) \left[ I - (e^{jS_1 d_1} R_{A1})^2 \right]^{-1} e^{jS_1 d_1} (I + R_{A1}) \quad (2.98)$$

$$T = (I - R_{A1}) \left[ I - (e^{jS_1 d_1} R_{A1})^2 \right]^{-1} e^{jS_1 d_1} (I + R_{A1}) \quad (2.99)$$

The final step is to model the whole periodic structure iteratively. It starts by combining two symmetric identical structures through a section of region (0) of length  $d_o$  as shown in figure 2.8. Using equations 2.80 and 2.81, the new reflection and transmission matrices for the combined structure is expressed in terms of the old reflection and transmission matrices of the individual structure, that is:

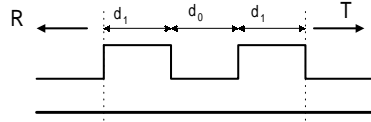


**Figure 2.8.** Two identical structures cascaded together

$$R_{new} \leftarrow R_{old} + T_{old} e^{jS_0 d_0} R_{old} \left[ I - (e^{jS_0 d_0} R_{old})^2 \right]^{-1} e^{jS_0 d_0} T_{old} \quad (2.100)$$

$$T_{new} \leftarrow T_{old} \left[ I - (e^{jS_0 d_0} R_{old})^2 \right]^{-1} e^{jS_0 d_0} T_{old} \quad (2.101)$$

These two equations are the basis of the Doubling Algorithm. The factor  $(I - (e^{jS_0 d_0} R)^2)^{-1} e^{jS_0 d_0} T$  is common in both equations which makes the algorithm fast. At each iteration, the number of grating periods simulated is doubled, that is 1, 2, 4, 8, 16, 32 and so on. This works in power of 2 only but we can model any number of periods by attaching the appropriate number of sections each having periods expressed as power of 2. For example we can model 10 periods by attaching 8 and 2 periods.

In **Paper B**, a deep asymmetrical waveguide grating from reference [10] (see figure 2.9) is modeled using the Cascading and Doubling Algorithm, and its

modal spectral reflectivity is calculated for different number of periods. The results are compared with previously published results [10] demonstrating the validity and numerical stability of the new derived algorithm. Such deep gratings can be useful for short-period DBR lasers [40].

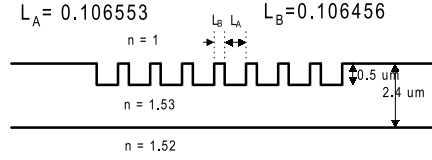


**Figure 2.9.** A deep waveguide grating structure, (COST 240 problem).

## 2.7 ARROW Grating Simulation

The idea of an ARROW structure was first proposed by M. A. Duguay and co-workers [23]. In a conventional waveguide, the guidance is due to total internal reflection (TIR) in a region of high refractive index surrounded by regions of lower refractive index. However, in the ARROW structure, the guidance is desired in a medium of low refractive index (such as the guide layer in figure 2.10(a)) surrounded on one or both sides by a medium of high refractive index (such as the substrate in figure 2.10(a)). The guidance in the guide layer is achieved by reflection from the anti-resonant layer (such as the ARROW layer in figure 2.10(a)). The ARROW structure is essentially a leaky waveguide [26] and the modes are characterized by a complex propagation constant having imaginary part representing radiation leakage. The radiation losses of the leaky waves can be reduced by the high reflectivity of the anti-resonant cladding layer [23]. Anti-resonant reflecting optical waveguides (ARROW) are useful as they can have large modal field with single mode operation. They are also selective for  $TE$  polarization and show high loss for the  $TM$  polarization. They can be integrated monolithically with electronic components in the  $\text{SiO}_2/\text{Si}$  material system [25]. When periodic corrugations are put on the top surface of an ARROW waveguide (see figure 2.10(a)) an ARROW grating is obtained. This leads to an optical wavelength filter. In addition, the ARROW grating is also expected to behave as a  $TE$ -pass reflection-mode polarizer since the  $TM$  polarized modes of ARROW waveguide are highly lossy. In this section, an example is given for the modes of an ARROW structure.

### 2.7.1 Unperturbed ARROW Waveguide

The Method of Lines is applied to find the field profile and the complex effective indices of different quasi-guided ARROW eigen-modes ( $TE$  and  $TM$ ) for the structure shown in the figure 2.10(a) [23]. The development of the fundamental

$TE_1$  and higher  $TE_2$  mode profiles is shown in the figure 2.10(b) at  $\lambda = 1.3 \mu m$  as the ARROW layer thickness is varied. By examining figure 2.10(b) and figure 2.11(a), it is clear that below the first resonance, the  $TE_1$  is effectively a core mode with the lowest attenuation. However, above the first resonance ( $d_{ARROW} > 0.2 \mu m$ ). The  $TE_2$  mode undergoes transformation becoming the effective core mode with the lowest attenuation (i.e. the  $TE_2$  mode takes the former role of the  $TE_1$  mode). The  $TE_1$  mode now peaks at the thin ARROW layer and develops an evanescent tail in the core. Thus when operating below resonance, the mode of interest to us will be the  $TE_1$  mode and when operating above the first resonance, the mode of interest is the  $TE_2$  mode.

The results for the propagation constant calculation (both real and imaginary parts) are shown in table 2.1 at the free-space wavelength of  $1.3 \mu m$ . The error of the MoL calculations as compared with the exact analytical results and the power loss of each mode in dB/cm are also shown in this table.

In **Paper C**, a shallow and a deep ARROW grating is simulated for its polarization discrimination properties. It is shown that by operating the ARROW slightly off resonance, the polarization discrimination properties can be maintained even for deep gratings.

Mode	$N_{eff}$ (MoL)	Error	Power Loss (dB/cm)
$TE_1$	1.44170016+6.038e-7j	-1.57e-7+6.661e-9j	0.255
$TE_2$	1.41701300+2.296e-4j	-1.48e-7+1.85e-6j	96.6
$TE_3$	1.41262699+2.164e-3j	-7.44e-7-1.95e-3j	889.95
$TE_4$	1.37370114+5.119e-5j	-2.33e-6+6.04e-7j	21.24
$TM_1$	1.44122731+1.315e-4j	-2.21e-7+1.67e-6j	54.41
$TM_2$	1.42013501+4.578e-3j	-2.85e-5+4.20e-5j	1888.28
$TM_3$	1.40832494+9.113e-3j	6.31e-5+1.24e-4j	3854.10

**Table 2.1.** Effective-index of different ARROW modes and the the corresponding error ( $N_{eff}(Analytical) - N_{eff}(MoL)$ )

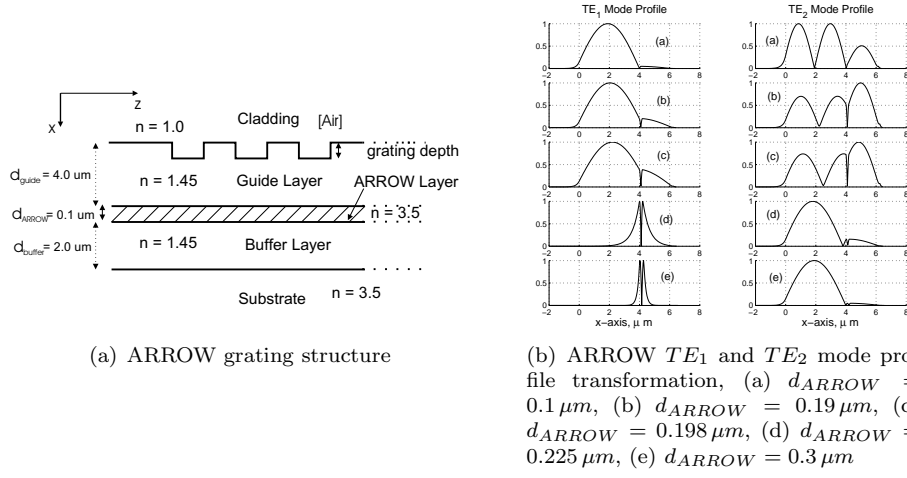
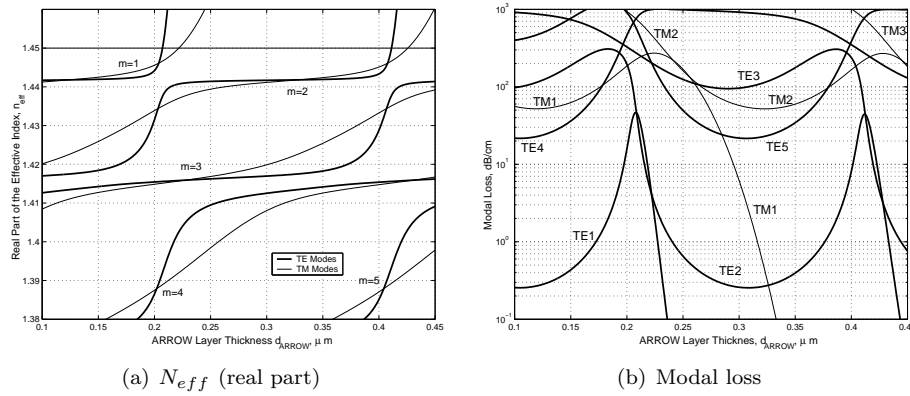


Figure 2.10. ARROW grating

Figure 2.11.  $N_{\text{eff}}$  and modal loss of  $TE$  and  $TM$  modes vs ARROW layer thickness



## Chapter 3

# Semiconductor Laser Simulation

### 3.1 Introduction

The word ‘LASER’ is an abbreviation of ‘Light Amplification by Stimulated Emission of Radiation’. However, a laser is usually not just an amplifier of radiation but also an oscillator which can provide continuous output of electromagnetic radiation at optical frequencies. A laser needs two basic ingredients: first is a material which makes the active region of the laser and provides net stimulated emission of radiation, and second is the resonant formation of a standing or traveling wave of the emitted radiation in a feedback cavity for the continuous operation of the laser. A semiconductor injection laser is build around a p-n junction concept as shown in figure 3.1. The injected current in a forward biased p-n junction provides optical gain in the active region of the laser. The resonant laser cavity is made from the cleaved facets of the diode (Fabry-Perot cavity in the  $z$ -direction) which act as mirrors. When sufficient current is injected in the p-n junction so that the optical gain experienced by the electromagnetic field is just enough to overcome the losses ( such as absorption, scattering and emission from facets) in the cavity, a continuous wave optical radiation is emitted from the facets of the diode. In order to minimize the optical losses in the cavity, an optical waveguide concept in the  $x-y$  plane is helpful to provide a confined mode of radiation without diffraction or leakage losses. In a double hetero-junction active region as shown in the figure 3.1, the P and N-cladding regions are made of a higher bandgap material (such as InP) and the active region is made of a lower bandgap material (such as InGaAsP alloy). Such structure has the advantage that both the injected electrons and holes are trapped in the lower bandgap material and cannot easily diffuse to the neighboring region. This carrier trapping at the same spatial location makes it possible to achieve necessary optical gain

for lasing at low injection current. Another advantage of such a layer configuration is that the lower bandgap material usually has a higher refractive index as compared to the higher bandgap material. Thus an optical waveguide is naturally achieved in the transverse  $x - y$  plane. In fact, these two concepts, that is the hetero-junction active region for carrier confinement and the transverse optical waveguide for optical confinement at the same spatial location have made possible the achieving of semiconductor injection lasing at room temperature with low injection current [41].

### 3.2 Basic Rate-Equation Model

In order to understand the static and dynamic operating characteristics of a semiconductor laser, a simple carrier reservoir model is helpful. It is based on establishing a balance between the inflow and the outflow of electrons (holes) and photons from the two coupled reservoirs in an injection laser as shown in figure 3.3. The one-dimensional carrier density and single-mode photon density rate equations can be written as [30]:

$$\frac{dN}{dt} = \frac{\eta_i I}{qV} - (R_{nr} + R_{Aug} + R_l + R_{sp}) - v_g g S \quad (3.1)$$

$$\frac{dS}{dt} = \Gamma v_g g S + \Gamma \beta_{sp} R_{sp} - S/\tau_p \quad (3.2)$$

where  $N$  is the electron density in the active region,  $S$  is the photon density in the cavity in the lasing mode,  $\eta_i$  is the fraction of injected current that passes through the active region,  $I$  is the injected current,  $q$  is the charge on electron,  $V$  is the volume of the active region,  $R_{nr}$  is the carrier loss rate due to non-radiative recombination,  $R_{Aug}$  is the carrier loss due to Auger recombination,  $R_l$  represents the carrier leakage and overflow from the active region,  $R_{sp}$  is the carrier recombination rate due to random spontaneous emission of photons (see figure 3.2),  $v_g$  is the group velocity of the optical mode in the waveguide,  $g$  is the material gain,  $\Gamma$  is the confinement factor,  $\beta_{sp}$  is the fraction of spontaneous emission into the lasing mode and  $\tau_p$  represents the photon lifetime in the cavity. Due to the assumption of charge neutrality in the active region, the electron density  $N$  is equal to the hole density  $P$ . Hence only one rate-equation for the electrons is sufficient. The carrier loss terms  $R_{nr} + R_{Aug} + R_l + R_{sp}$  can be approximated with an equivalent carrier decay term  $N/\tau$  where  $\tau$  is the carrier lifetime in the active region. The term  $v_g g S$  represents the stimulated recombination and couples the two rate-equations to each other.

#### 3.2.1 Threshold Condition

The threshold condition for a Fabry-Perot laser can be derived by equating the amplification of optical mode due to the gain in the cavity to the attenuation

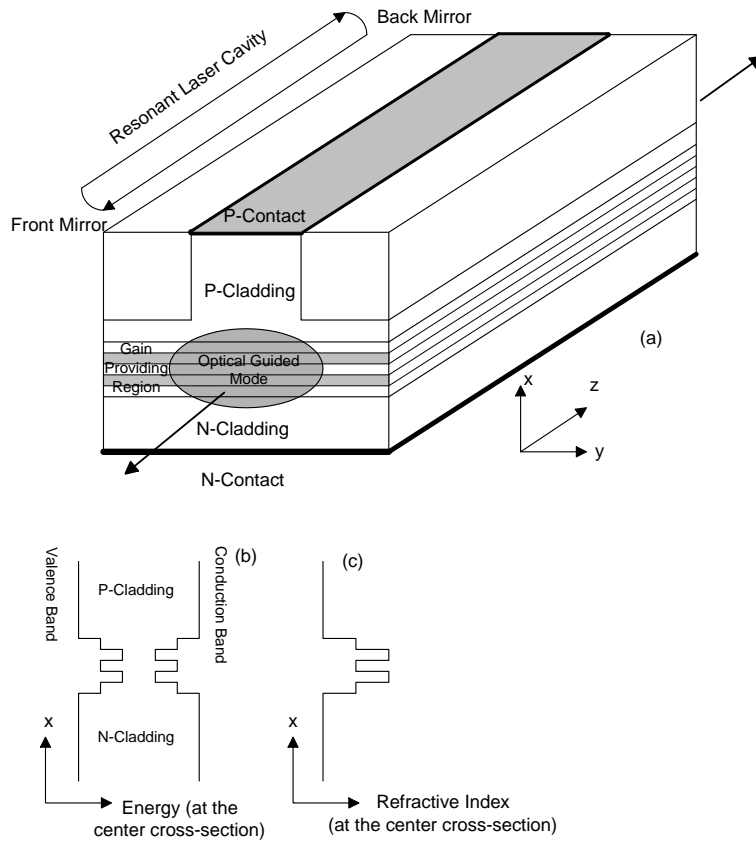


**Figure 3.1.** Schematic diagram of a semiconductor quantum-well laser structure (a), its band diagram (b) and refractive-index profile (c)

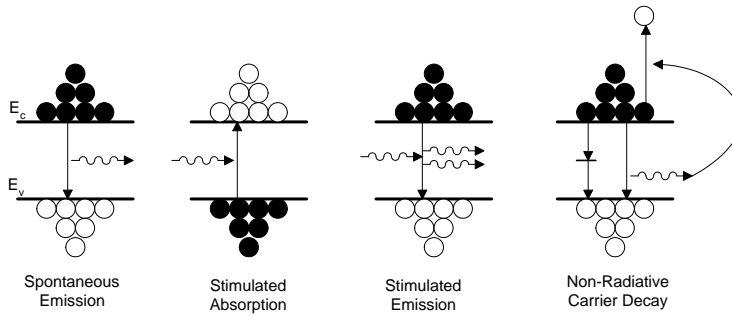


**Figure 3.2.** Electronic transitions (radiative and non-radiative) between the conduction and valences bands in a semiconductor

suffered by the guided mode due to optical losses in the cavity. The electric field  $\mathbf{E}$  of a guided mode  $U(x, y)$  propagating in a cavity along the  $z$ -axis as shown in figure 3.4 can be described as:

$$\mathbf{E} = \mathbf{E}_0 U(x, y) e^{j(\omega t - \tilde{\beta} z)} \quad (3.3)$$

where  $\mathbf{E}_0$  represents the polarization and the maximum amplitude of the electric field,  $\tilde{\beta}$  is the complex propagation constant of the guided mode comprising the gain and the loss suffered by the mode. That is:

$$\tilde{\beta} = \beta_r + j\beta_i = \beta_r + \frac{j}{2}(\Gamma g - \alpha_i) \quad (3.4)$$

where  $\beta_r = 2\pi n_{eff}/\lambda$  ( where  $n_{eff}$  is the guided mode effective index) is the phase constant experienced by the mode and can be determined from the procedures in chapter 2.  $\alpha_i$  is the internal intensity loss (absorption, scattering etc) experienced by the guided mode in the cavity and  $g$  is the material gain associated with the intensity of the field. For a sustainable electric field pattern in the cavity, the electric field vector  $\mathbf{E}$  must exactly duplicate itself after one complete round trip in the cavity. This restriction, called longitudinal resonance condition, can be used to determine the required gain for lasing as well as the emission wavelengths of the laser cavity. Thus we can write that for threshold condition,  $\mathbf{E}(z = 0) = \mathbf{E}(z = 2L)$ . That is:

$$r_1 r_2 e^{-2j\tilde{\beta}L} = 1 \quad (3.5)$$

This complex equation 3.5 can be broken into its magnitude and phase equations. The magnitude equation is (assuming  $r_1, r_2$  are real):

$$r_1 r_2 e^{(\Gamma g - \alpha_i)L} = 1 \quad (3.6)$$

from which the required gain for lasing  $g_{th}$  can be derived as:

$$\Gamma g_{th} = \alpha_i + \frac{1}{L} \ln\left(\frac{1}{r_1 r_2}\right) \quad (3.7)$$

here  $\frac{1}{L} \ln\left(\frac{1}{r_1 r_2}\right)$  represents the useful light emission from both facets of the laser (called mirror loss  $\alpha_m$ ),  $L$  is the cavity length and  $r_1, r_2$  are the facet amplitude reflection coefficients of the electric field.

The phase part from equation 3.5 is  $e^{2j\beta_r L} = 1$  which requires that  $\beta_r L = m\pi$  giving us condition on the longitudinal resonance wavelengths  $\lambda_{res}$ :

$$\lambda_{res} = \frac{2n_{eff}L}{m} \quad (3.8)$$

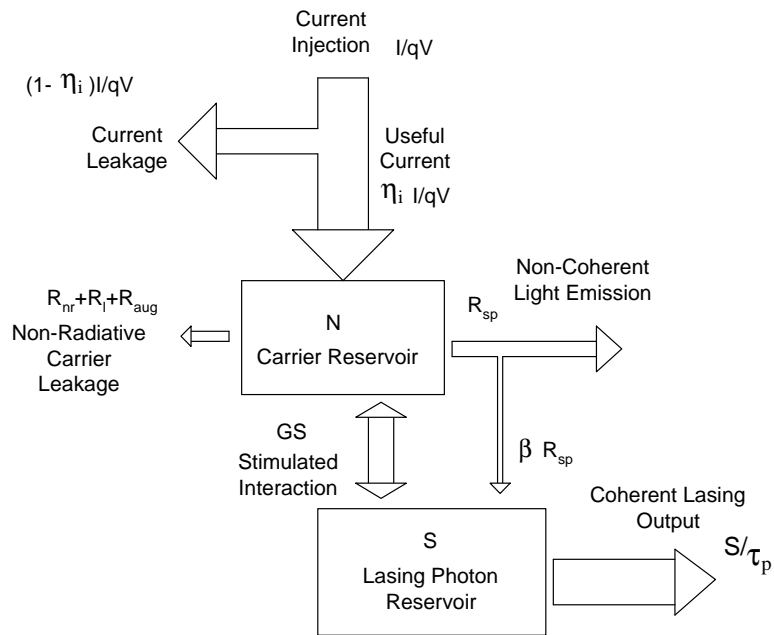


**Figure 3.3.** Carrier reservoir model of a semiconductor laser used in the rate-equations

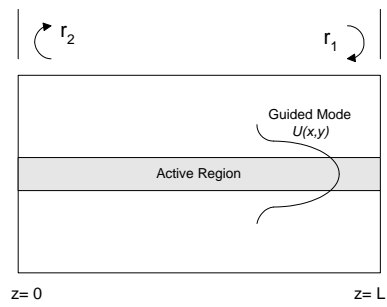


**Figure 3.4.** Schematic diagram of an FP cavity

### 3.2.2 Steady-State Characteristics

The steady-state characteristics of a laser can be derived from the two rate-equations 3.1 and 3.2 by setting the time-derivative terms  $\frac{d}{dt}$  to zero. From the first equation 3.1, we ignore the stimulated recombination term  $v_g g S$  at threshold since lasing photon density  $S$  is negligible at threshold. This gives us the threshold current.

$$I_{th} = \frac{qV N_{th}}{\eta_i \tau} \quad (3.9)$$

where  $N_{th}$  is the threshold carrier density. The threshold carrier density  $N_{th}$  can be calculated by assuming (or modelling) a gain equation of the form  $g = g_o \ln(N/N_{tr})$  where  $g_o$  and  $N_{tr}$  are the active region material parameters. Thus:

$$N_{th} = N_{tr} e^{g_{th}/g_o} = N_{tr} e^{(\alpha_i + \alpha_m)/\Gamma g_o} \quad (3.10)$$

Above threshold the carrier density  $N$  in the active region is fixed to  $N = N_{th}$  due to the coupling of the  $v_g g S$  term in both the rate equations. Using this fact, one can derive the output power  $P_o$  from both facets above threshold as [30] :

$$P_o = \eta_i \frac{\alpha_m}{\alpha_i + \alpha_m} \frac{h\nu}{q} (I - I_{th}) \quad (3.11)$$

where  $h\nu$  is the energy per photon at the lasing frequency  $\nu$ .

### 3.2.3 Dynamic Characteristics

The two coupled rate-equations 3.1 and 3.2 are non-linear equations. However they can be linearized around an operating point and their small-signal time-harmonic properties can be derived. Taking derivatives of both equations and assuming that  $I$ ,  $N$ ,  $S$ ,  $g$  are dynamic variables, we get:

$$\partial \left[ \frac{dN}{dt} \right] = \frac{\eta_i dI}{qV} - \frac{dN}{\tau_{\Delta N}} - v_g g dS - S v_g dg \quad (3.12)$$

$$\partial \left[ \frac{dS}{dt} \right] = \Gamma v_g g dS + S \Gamma v_g dg - dS/\tau_p \quad (3.13)$$

where the  $\Gamma \beta_{sp} R_{sp}$  term is ignored above threshold and  $\tau_{\Delta N}$  is the differential carrier lifetime defined as:

$$\frac{1}{\tau_{\Delta N}} = \frac{d(R_{nr} + R_{Aug} + R_l + R_{sp})}{dN} \quad (3.14)$$

The material gain  $g$  is affected both by the carrier density  $N$  and the photon density  $S$ . Assuming a gain mode  $g = \frac{g_o \ln(N/N_{tr})}{1 + \epsilon S}$ , where  $\epsilon$  represents the gain reduction at high photon density due to carrier heating and spectral hole burning

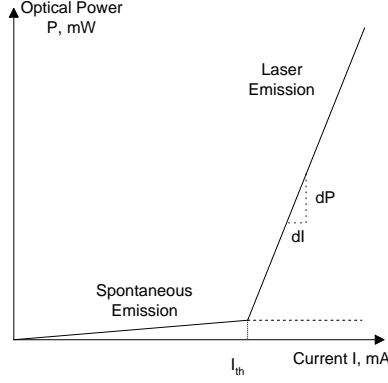


**Figure 3.5.** Light-Current response of an injection laser

[30]. Thus the differential gain is  $dg = adN - a_p dS$  where  $a \equiv \partial g / \partial N$  and  $a_p \equiv -\partial g / \partial S$ . Thus putting 3.12 and 3.13 in a matrix form, we get:

$$\frac{\partial}{\partial t} \begin{bmatrix} dN \\ dS \end{bmatrix} = \begin{bmatrix} -\gamma_{NN} & -\gamma_{NP} \\ \gamma_{PN} & -\gamma_{PP} \end{bmatrix} \begin{bmatrix} dN \\ dS \end{bmatrix} + \frac{\eta_i}{qV} \begin{bmatrix} dI \\ 0 \end{bmatrix} \quad (3.15)$$

where  $\gamma_{NN} = 1/\tau_{\Delta N} + v_g a S$ ,  $\gamma_{NP} = 1/\Gamma \tau_p - v_g a_p S$ ,  $\gamma_{PN} = \Gamma v_g a S$  and  $\gamma_{PP} = \Gamma v_g a_p S$  [30]. For small-signal time-harmonic solution, we assume a sinusoidal current imposed on the dc-bias current, thus the solution may be assumed of the form:

$$dI(t) = \tilde{I} e^{j\omega t} \quad (3.16)$$

$$dN(t) = \tilde{N} e^{j\omega t} \quad (3.17)$$

$$dS(t) = \tilde{S} e^{j\omega t} \quad (3.18)$$

Setting  $d/dt \rightarrow j\omega$  and rearranging terms in the equation 3.15, we get:

$$\begin{bmatrix} \gamma_{NN} + j\omega & \gamma_{NP} \\ -\gamma_{PN} & \gamma_{PP} + j\omega \end{bmatrix} \begin{bmatrix} \tilde{N} \\ \tilde{S} \end{bmatrix} = \frac{\eta_i \tilde{I}}{qV} \begin{bmatrix} 1 \\ 0 \end{bmatrix} \quad (3.19)$$

The solution for  $\tilde{N}$  and  $\tilde{S}$  can be obtained from 3.19 using Cramer's rule. Thus we get:

$$\tilde{N} = \frac{\eta_i \tilde{I}}{qV} \frac{\gamma_{PP} + j\omega}{\omega_R^2} H(\omega) \quad (3.20)$$

$$\tilde{S} = \frac{\eta_i \tilde{I}}{qV} \frac{\gamma_{PN}}{\omega_R^2} H(\omega) \quad (3.21)$$

where

$$H(\omega) = \frac{\omega_R^2}{\omega_R^2 - \omega^2 + j\omega\gamma} \quad (3.22)$$

is the two-parameter modulation transfer function,  $\omega_R^2 \equiv \gamma_{NP}\gamma_{PN} + \gamma_{NN}\gamma_{PP}$  is called the relaxation resonance frequency and  $\gamma \equiv \gamma_{NN} + \gamma_{PP}$  is called the damping parameter. Above threshold, the expressions for  $\omega_R$  and  $\gamma$  can be simplified to:

$$\omega_R^2 = \frac{v_g a S}{\tau_p} \quad (3.23)$$

$$\gamma = \frac{1}{\tau_{\Delta N}} + v_g a S \left(1 + \frac{\epsilon}{a v_g \tau_p}\right) \quad (3.24)$$

Using equation 3.23 in 3.24, we can write  $\gamma$  as a function of resonant frequency  $f_R = \omega/2\pi$ , that is:

$$\gamma = \gamma_o + K f_R^2 \quad (3.25)$$

where  $\gamma_o = \tau_{\Delta N}^{-1}$  and  $K = 4\pi^2(\tau_p + \frac{\epsilon}{v_g a})$ . Moreover,  $f_R$  can be expressed as a function of the input current, that is:

$$f_R = D \sqrt{I - I_{th}} \quad (3.26)$$

where  $D = \frac{1}{2\pi} \sqrt{\eta_i \frac{\Gamma v_g a}{qV}}$ . The  $K$ -factor and the  $D$ -factor are useful for characterising the maximum possible modulation frequency of a laser.

### 3.2.4 Parasitic Effects

Until now, only the intrinsic response of the junction laser is described. However, there are parasitic resistance and capacitance associated with a junction laser as shown in figure 3.6. The series resistance  $R_d$  is mainly due to the P-cladding. A shunt resistance could exist due to current leakage from the sides of the p-n junction. A parallel capacitance  $C_p$  could exist across the p-n junction due to the capacitance associated with semi-insulating layers or polymer burying layers. For dynamic response, the parasitics could affect the laser intrinsic response especially at higher modulation frequencies. In **Paper D**, it is shown that the finite drive impedance of the generator and/or parasitic capacitance of the laser chip in combination with the carrier density fluctuations across the laser active layer  $\tilde{N}$  significantly increases the damping  $\gamma$  of the laser modulation response. This excess damping is especially pronounced if the volume of the active region is small such as for a vertical cavity surface emitting laser (VCSEL), and corresponds to a reduction of the differential carrier lifetime  $\tau_{\Delta N}$ . The parasitics effect can be analyzed by including a third rate-equation describing the inflow of carriers from the injection source to the laser active volume. This extra rate-equation is coupled to the carrier-photon dynamics via the voltage fluctuations



across the active layer of the laser. The three coupled rate-equations can be solved for the small-signal modulation response of the laser. The parasitic cut-off frequency, the damping rate and the resonant frequency of the laser can be derived from the poles of the small-signal modulation response.

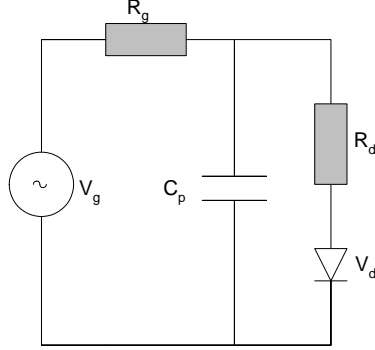


**Figure 3.6.** Equivalent circuit of a laser and parasitics

### 3.3 Self-Consistent 2D Simulation

Previously described rate-equation model is useful for basic understanding of the intrinsic response of a laser. However, for detailed simulation such as carrier injection simulation, gain calculation, optical waveguide mode calculation and carrier leakage, physics based device simulation is necessary. Such simulation is based on fundamental partial differential equations describing the electronic, optical and quantum mechanical aspects of a semiconductor laser. In **Paper E** and **F**, a commercial software LASTIP [42] is used for these simulations. The device simulation is based on the Poisson equation for the electrostatic potential  $\phi$  (equation 3.27) and the carrier continuity equations combined with the drift-diffusion model for the carrier transport [33] (equations 3.28-3.29). An optical rate equation (equation 3.30) is used to calculate the photon density  $S$  in the lasing mode and couples the electronic and the optical equations through the stimulated recombination term  $R_{st}$  (equation 3.31). The transverse optical modal shape  $\psi(x, y)$  and the effective index  $n_{eff}$  are calculated by solving the scalar Helmholtz equation 3.32. The 2D optical field  $\psi(x, y)$  is normalized such that  $\int \int |\psi|^2 dx dy = 1$ .

$$\nabla \cdot (\epsilon_o \epsilon_{dc} \nabla \phi) = -q(p - n + N_d^+ - N_A^-) \quad (3.27)$$

$$\frac{\partial n}{\partial t} = \nabla \cdot [-\mu_n n \nabla \phi + D_n \nabla n] - R_{SRH} - R_{Aug} - R_{sp} - R_{st} \quad (3.28)$$

$$\frac{\partial p}{\partial t} = \nabla \cdot [+ \mu_p p \nabla \phi + D_p \nabla p] - R_{SRH} - R_{Aug} - R_{sp} - R_{st} \quad (3.29)$$

$$\frac{\partial S}{\partial t} = \int \int R_{st} dx dy - \frac{S}{\tau_p} + \beta_{sp} \int \int R_{sp} dx dy \quad (3.30)$$

$$R_{st} = v_g S g(x, y) |\psi(x, y)|^2 \quad (3.31)$$

$$(\nabla_{xy}^2 + k_o^2 \epsilon_{opt}) \psi(x, y) = k_o^2 n_{eff}^2 \psi(x, y) \quad (3.32)$$

here,  $p$  and  $n$  are the mobile hole and electron density,  $N_d^+$  and  $N_A^-$  are the immobile ionized donor and acceptor density that make the p-n junction,  $\epsilon_o$  is the permittivity of the free space,  $\epsilon_{dc}$  and  $\epsilon_{opt}$  are the relative permittivity at low-frequency (DC) and at the lasing frequency respectively,  $\mu_n$ ,  $\mu_p$  and  $D_n$ ,  $D_p$  are the corresponding carrier mobilities and diffusion constants,  $v_g$  is the optical mode group velocity,  $k_o = 2\pi/\lambda$  is the optical wavevector,  $\tau_p$  is the photon lifetime in the cavity and  $\beta_{sp}$  is the coupling coefficient of the spontaneous emitted power into the lasing mode. A parabolic isotropic conduction band is assumed and the valence band dispersion including the effects of strain is calculated using  $4 \times 4$   $\mathbf{k} \cdot \mathbf{p}$  method [43–45]. The optical gain spectrum  $g(n, \lambda)$  is calculated from the calculated band structure assuming a Lorentzian lineshape broadening function with a time constant  $\tau_{scat} = 0.1$  psec. The reduction of optical gain at high optical power is included phenomenologically using the form  $g(n, S) = g(n)/(1 + \epsilon S)$  where  $\epsilon$  is the non-linear gain compression factor. The spontaneous emission rate  $R_{sp}$  is calculated self-consistently from the calculated optical gain spectrum. A thermionic emission model [42, 46] is used to simulate the carrier transport over the hetero-barriers in the MQW region, since drift-diffusion theory is not valid at the hetero-junctions. Carrier loss mechanisms, such as non-radiative recombination  $R_{SRH}$  and Auger recombination  $R_{Aug}$  are included phenomenologically, using parameters taken from published work [47, 48]. The default material parameters such as bandgap, lattice constant, effective masses, Luttinger parameters and carrier mobility for quantum well, barrier and passive layers are used in the simulation. Quantum well and barrier region intervalence-band absorption loss (IVBA),  $\alpha_p = k_p p$ , is calculated phenomenologically which depends upon the local density of holes within the quantum wells [47].

### 3.3.1 Thermionic Emission Current at a Hetero-Junction

To model the current at an abrupt junction between two different materials as shown in figure 3.7, thermionic emission theory is implemented in the simulation software [42]. The drift-diffusion theory is not valid at a heterojunction due to the bandedge discontinuity. The current flux across the junction is defined as:

$$J_n = \gamma_n v_{bn}^{therm} (n_b - n_{b0}) \quad (3.33)$$

$$J_h = \gamma_p v_{bp}^{therm} (p_b - p_{b0}) \quad (3.34)$$

where  $n_b$  and  $p_b$  denote the electron and hole concentration respectively on the barrier side of the junction.  $n_{b0}$  and  $p_{b0}$  denote the electron and hole concentration when quasi Fermi level is equal on both sides of the junction. The constants

$\gamma_n$  and  $\gamma_p$  provide a mechanism to include any correction to the standard theory. The thermal recombination velocities are given by:

$$v_{bn}^{therm} = \sqrt{\frac{kT}{2\pi m_{bn}}} \quad (3.35)$$

$$v_{bp}^{therm} = \sqrt{\frac{kT}{2\pi m_{bp}}} \quad (3.36)$$

where  $m_{bn}$  and  $m_{bp}$  are the electron and hole effective mass on the barrier side.

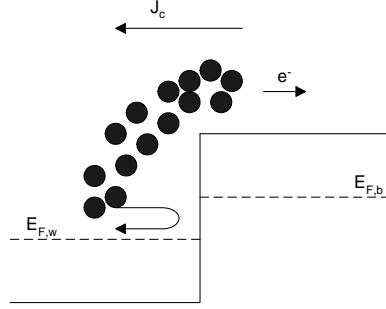


**Figure 3.7.** A heterojunction and thermionic emission current

### 3.4 Multiple Quantum Well Active Region Optimization

Modern day semiconductor lasers used for optical communication are usually based on multiple quantum-well active region [30]. A quantum well is a thin double hetero-junction layer structure with thickness of the order few nanometers. It acts a confining waveguide along the direction of the quantum well for the electrons and holes just like an optical waveguide structure as explained in the previous chapter. The carrier wavefunction assumes discrete energy levels along the direction of the quantum-well modifying the emission wavelength of the laser. An advantage of a quantum well laser is the reduction in the threshold current due to reduced volume of the active region. By growing quantum well and barrier layers with lattice constant different from the underlying substrate, called strain engineering, one can further reduce the threshold current and increase the modulation bandwidth of the laser [30]. Historically, the InGaAsP(well) / InGaAsP(barrier) / InP(substrate) material has been mainly used for the 1300nm and 1550nm lasers. However, the large valence band discontinuity ( $\Delta E_v \approx 60\% \Delta E_g$ ) [49] in this material system increases the effective hole quantum well (QW) confinement energy and limits the vertical hole transport

through the multi-quantum wells (MQW). This can result in a hole pile-up on the p-side of the active region. The increased hole population at the p-side of the MQW also increases the electron population on the p-side due to Coulomb attraction and higher mobility of electrons. This largely affects the total material gain and carrier density dependent losses. For a given total carrier density  $n$  in the MQW, the sum of the material gain from all wells is less in the non-uniform case than that if the carrier density is uniform in all the wells. This is due to a sublinear relationship of the material gain  $g$  with carrier density  $n$  ( $g \propto \ln(n)$ ). In a similar fashion, the carrier losses increase superlinearly with carrier density (Auger recombination  $\propto n^3$  and spontaneous recombination  $\propto n^2$ ) and hence the total carrier losses are enhanced in the non-uniform case. The material gain and loss distribution limits the maximum number of wells that can be effectively used if the hole confinement energy is too large. Auger recombination and electron leakage at high optical power has been shown to be the main carrier loss mechanism in 1550nm lasers [47, 48, 50, 51]. By aiming for a uniform carrier density in all the wells, the total material gain can be maximized and the non-radiative carrier losses minimized, which is essential to reduce the threshold current and the threshold carrier density in the wells. For direct modulation of semiconductor laser, the differential gain  $dg/dn$  is one of the most important factors which limits the modulation bandwidth [30]. The differential gain is higher at low carrier density and an improved modulation bandwidth can be achieved by operating all the wells at minimum carrier density, which is an additional benefit of using an optimized carrier distribution in the QWs.

As shown in **Paper E**, an InGaAsP(well)/InGaAlAs(barrier) combination is useful for improved carrier (especially holes) transport through MQWs. Due to a large conduction band discontinuity ( $\Delta E_c \approx 72\% \Delta E_g$ ) in this material system [49], the effective confinement energy for electrons is increased while the confinement energy for holes ( $\Delta E_v \approx 28\% \Delta E_g$ ) is reduced for the same barrier bandgap as compared to an InGaAsP barrier. Consequently, the thermionic emission barrier for the holes will be smaller. By utilizing compressive strained well and tensile strained barrier, the thermionic emission barrier can be further reduced due to the splitting of heavy-hole and light-hole band edges [52] since the holes in the quantum well can thermalize over the light hole energy level in the barrier [53]. The number of wells can be increased in the active region and still maintain good carrier transport and population inversion in all the wells simultaneously. Moreover, the deeper electron wells are also advantageous since electrons easily escape from the wells if the wells are too shallow [48, 50] due to their light effective mass. Making the electron wells deeper will improve their confinement in the active region especially at higher temperatures.

### 3.4.1 Single Quantum Well Material Gain

The material gain from an individual quantum well is an important design parameter. In **Paper E**, an optimization is performed to get a quantum well structure with good carrier transport and gain properties. A compressive well with

tensile barrier has been theoretically [43,44,52,54,55] and experimentally [56–58] shown to achieve high gain, differential gain and a large modulation bandwidth. A 0.88% compressive strain  $In_{0.75}Ga_{0.25}As_{0.81}P_{0.19}$  well and  $In_{0.41}Ga_{1-y}Al_yAs$  0.83% tensile strained barrier are considered here. The well composition is kept fixed in these simulations and the barrier bandgap is varied between 1420nm to 1280nm by changing the Aluminum fraction (from 12% to 20%) keeping its strain almost fixed to maintain strain compensation. The material gain vs. carrier density results for 8nm well thickness are presented in figure 3.9. An optimum material gain is obtained at the barrier bandgap of around 1350nm (16% Al). If the barrier is too low (12% Al), the confinement of electrons in the well is reduced due to their small effective mass. This reduces the overlap between the electron and the hole wavefunctions, thus reducing the gain from the well. Moreover, the material gain saturates quickly even at lower carrier density due to the transformation from 2D stair-case QW density of state to a 3D parabolic bulk density of state [59]. On the other hand if the barrier is too high (20% Al), there are too many electron, heavy and light hole subbands. The subbands for the light hole can also be populated but they do not contribute to the optical gain for the *TE*-polarized light [43], thus decreasing the material gain for the same carrier density.

### 3.4.2 Carrier and Gain Non-Uniformity Among Wells

For this simulation, the simulated device structure is shown in figure 3.8(a). Since we are only interested in the carrier transport along *y*-direction, the waveguide is considered infinite along the *x*-axis. This can be implemented in the simulation software by a transparent boundary condition on both sides along the *x*-axis. Simulations are done for three different p-doping values in the active region and the results are presented in figures 3.10(a)-3.10(c) (electron/hole distribution) and figure 3.10(d) (local material gain). The carrier distribution in the MQW region depends not only upon the carrier transport over the hetero-barriers but also on carrier loss mechanism such as Auger recombination. For the low barrier MQWs, the carrier distribution (both holes and electrons) is uniform among all the wells. As the barrier bandgap is increased, the carrier distribution becomes more non-uniform and carrier accumulation takes place on the n-side of the MQW. This is due to the increased well depth for electrons and is a fundamental change in the carrier distribution due to the large conduction band offset compared to the InGaAsP/InGaAsP system. Due to Coulomb attraction, the holes are now probably attracted toward electrons on the n-side. The carrier accumulation is pronounced for barrier bandgaps of  $\lambda_g \leq 1300\text{nm}$ .

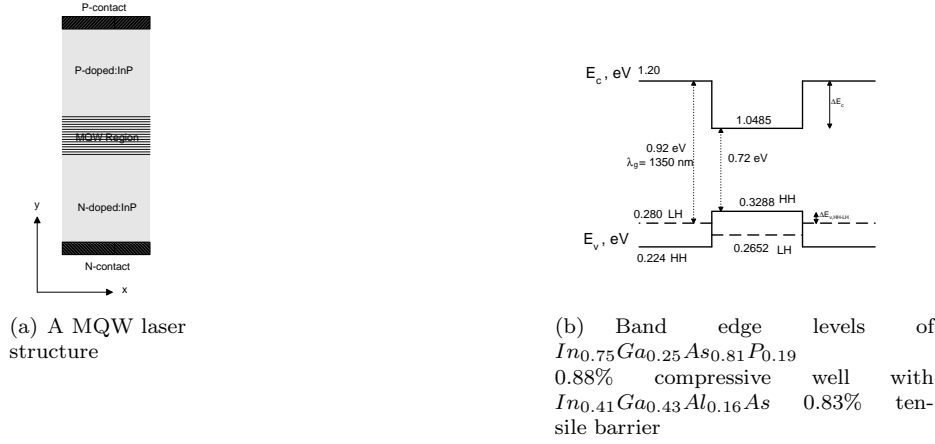


Figure 3.8. A MQW laser structure and band edge levels for a QW

## 3.5 Lateral Current Injection (LCI) Laser

### 3.5.1 Introduction

Semiconductor injection lasers as described before usually employ vertical carrier injection (VCI) of both holes and electrons through the heterojunction barriers in the multiple quantum-well active region to achieve population inversion and hence optical gain. The carrier transport mechanism from one heterojunction region to the next one is thermionic emission current [42, 46] which is exponentially dependent upon the bandedge discontinuity between the two regions. For efficient injection of carriers in VCI laser, especially holes since they have higher effective-mass and lower mobility, a reduced bandedge discontinuity between the well and the barrier region is desirable. This is done in **Paper E** by using InGaAsP quantum wells with shallow InGaAlAs barriers to get reduced valence

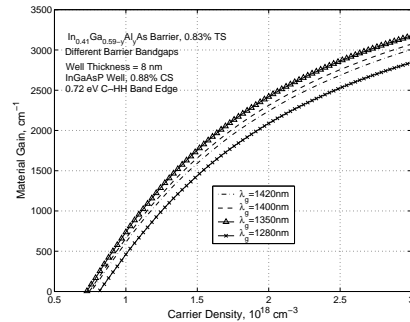
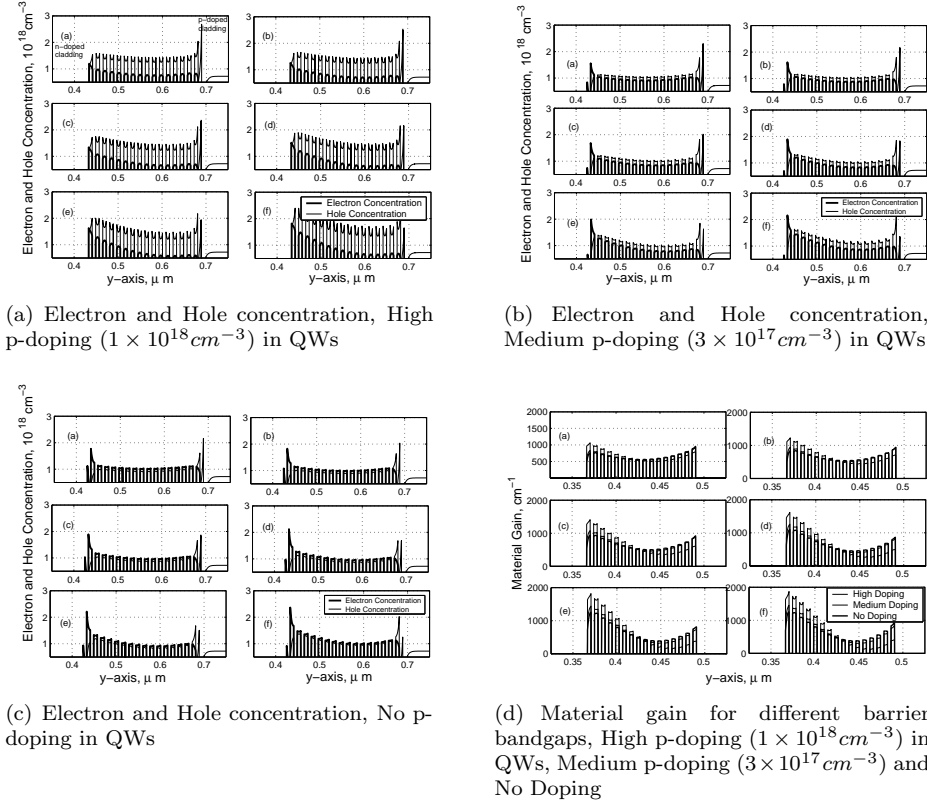


Figure 3.9. Material gain for a quantum well with different barrier bandgaps



**Figure 3.10.** Electron concentration, Hole concentration and material gain, 10 mA bias current,  $\approx 2$  mW optical power/facet, For each subfigure (a)  $\lambda_g = 1400\text{nm}$  barrier, (b)  $\lambda_g = 1370\text{nm}$  barrier, (c)  $\lambda_g = 1350\text{nm}$  barrier, (d)  $\lambda_g = 1325\text{nm}$  barrier, (e)  $\lambda_g = 1300\text{nm}$  barrier, (f)  $\lambda_g = 1280\text{nm}$  barrier

band discontinuity and improve the hole injection.

In VCI scheme, all the quantum wells are fed in series which limits the maximum number of quantum wells in the active region that can be efficiently injected. An alternate approach is to inject carriers parallel to quantum well hetero-junctions called lateral current injection (LCI). Previous work has been done to explore the LCI concept both theoretically [60–63] and experimentally [64–69]. However, the performance of LCI lasers has not reached to a level where they can be an alternate to the VCI lasers. The hole injection in LCI lasers is a major problem due to poor hole mobility in compound semiconductor materials. In vertical injection lasers, the distance traveled by carriers in the active region where they can interact with the photon field depends upon the well thickness (5–10 nm) and the number of wells (5–15), and is usually of the order of (25–150 nm). However, in LCI laser configuration, the carriers travel parallel to the quantum wells and the travel distance is equal to the active region width or mesa width which is of the order of 0.75–2.0  $\mu\text{m}$ . In the presence of photon field during lasing, stimulated recombination reduces the carrier lifetime considerably and the area of the active region away from the hole-injection contact is not sufficiently inverted to provide much gain. Hence the width of the active region has to be reduced to improve the carrier (especially holes) and gain uniformity across the whole active region and provide equal gain from all parts of the quantum wells. In **Paper F**, a simulation exercise is performed to design an optimum geometry of an LCI laser. The effects of different mesa width and p-doping in the QWs on the carrier and gain uniformity across the active region are explored.

### 3.5.2 Device Geometry

The device geometry for an LCI laser is shown in figure 3.11(a). The MQW active region is grown on a semi-insulating (SI) substrate and the top cladding layers is also SI:InP for better current confinement. This help reduce the current leakage at high forward bias from the parasitic p-n junctions in parallel to the lasing QWs [61]. A mesa is etched through the QWs and the InP p- and n-cladding regions are selectively re-grown [60]. The p and n-dopants in the left and the right cladding regions could be introduced during re-growth (two regrowth steps) or ion-implanted (one regrowth step) [60]. For comparison, a vertical carrier injection device is also shown in figure 3.11(b).

Practical problems associated with the LCI laser growth and device processing are the separate re-growth of the p- and n-cladding, and the top semi-insulating InP cladding layer. These extra re-growth steps increase the device complexity and cost. Many alternate schemes have been presented in the literature for manufacturing an LCI laser. To avoid re-growth steps, The p- and n-cladding regions can also be doped by ion-implantation [68] or dopant diffusion [65,70]. During ion-implantation of dopants, the decomposition of InP above 360°C is a problem, and the activation of high p-dopant density is difficult [60]. The dopant diffusion is also a relatively uncontrolled process and the location



of the p-n junction is unpredictable. Moreover, the dopants could also diffuse into the SI or undoped top and bottom InP layers creating carrier leakage paths around the QWs. If the regrowth of InP cladding is not preferred, the bandgap of the quaternary cladding can be increased through diffusion doping, QW intermixing or ion-implantation [69,71]. However, the increase in the bandgap of the cladding region is usually not sufficient to prevent the carrier leakage (especially electrons) out of the QWs into the cladding. The top and the bottom claddings could be made of undoped InP [64]. These parallel undoped InP layers create excess current leakage paths around the active region especially at high forward bias thus degrading the lasing efficiency and roll-over in the laser output. Some of the difficulties in fabricating LCI laser are highlighted in [60].

### 3.5.3 Simulation Model

The simulation model is based on the same equations as described in section 3.3. A dopant and field dependent mobility model is used to simulate the reduction in carrier mobility at higher dopant density and electric field. The laser active region operates at high forward bias current and the electric field magnitude in the active region is small which does not affect the carrier transport. The carrier transport is mainly through the diffusion process parallel to the QWs. The mobility model used is:

$$\mu_{p,n} = \frac{\mu_{0p,n}}{(1 + (\frac{\mu_{0p,n}F}{v_{sp,n}})^{\beta_{p,n}})^{\beta_{p,n}^{-1}}} \quad (3.37)$$

$$\mu_{0p,n} = \mu_{1p,n} + \frac{\mu_{2p,n} - \mu_{1p,n}}{1 + (\frac{N_D + N_A}{N_{rp,n}})^{\alpha_{p,n}}} \quad (3.38)$$

where  $\mu_{1p,n}$ ,  $\mu_{2p,n}$ ,  $\alpha_{p,n}$ ,  $\beta_{p,n}$  are the fitting parameters,  $v_{sp,n}$  is the carrier saturation velocity,  $N_{rp,n}$  is the reference dopant density and  $N_D$ ,  $N_A$  are the total donor and acceptor density respectively. These values are taken from [42] and are given in table 3.1. Quantum well and barrier region intervalence-band absorption (IVBA) loss  $\alpha_p = k_p p$  is calculate phenomenologically which depends upon the local density of holes (p) within the quantum wells. To simulate the semi-insulation (SI) Fe-doped InP layers, the trap density  $N_t$ , electron and hole capture cross-section  $\sigma_n$ ,  $\sigma_p$  and the deep trap level  $E_t$  below the conduction band edge is taken from [72].

### P-I and V-I Characteristics

In **Paper F**, LCI lasers with mesa width of 0.5, 1.0 and 1.5  $\mu m$  are simulated for their static performance. Their I-P and I-V-R curves are plotted in figures 3.12(a)-3.12(b). The laser with 0.5  $\mu m$  has the smallest threshold current and for 1.5  $\mu m$  mesa width, the threshold current is high.

### Carrier and Gain Non-Uniformity

The electron, hole and gain distribution in the active region are plotted in figures 3.13(a)-3.13(b) at a bias current of 75 mA. It is clear from these results that the carrier distribution (especially holes) in the active region depends upon the mesa width. The hole distribution shows a peak at the injection side (p-side cladding) and it decreases toward the n-side cladding. The electron distribution also follows the hole distribution due to Coulomb attraction and the fact that electron mobility is much higher than the hole mobility. Hence, the gain is highly non-uniform and peaked toward the p-side for wider mesas due to its strong dependence on both electron and hole density locally. For  $1.5 \mu m$  mesa, the active region close to the n-side is not providing gain as the carrier density is not high. The overlap between the gain region in the QWs and the optical intensity should be large for efficient lasing operation. As the mesa width is increased, the overlap between the gain region and the modal intensity peak is reduced, hence more gain is required from the p-side of the QWs to compensate for the reduction in the overlap.

$\mu_{1p}$	$0.0 \text{ m}^2 V^{-1} sec^{-1}$	$\mu_{1n}$	$0.0 \text{ m}^2 V^{-1} sec^{-1}$
$\mu_{2p}$	$0.036 \text{ m}^2 V^{-1} sec^{-1}$	$\mu_{2n}$	$0.45 + 0.65y \text{ m}^2 V^{-1} sec^{-1}$
$v_{sp}$	$1.0 \times 10^5 \text{ m sec}^{-1}$	$v_{sn}$	$1.0 \times 10^5 - 0.225 \times 10^5 y \text{ m sec}^{-1}$
$\alpha_p$	0.4	$\alpha_n$	0.436
$\beta_p$	1.0	$\beta_n$	2.0
$N_{rp}$	$9.6 \times 10^{20} \text{ m}^{-3}$	$N_{rn}$	$1.69 \times 10^{24} \text{ m}^{-3}$

**Table 3.1.** Carrier mobility fitting parameters for  $In_{1-x}Ga_xAs_yP_{1-y}$

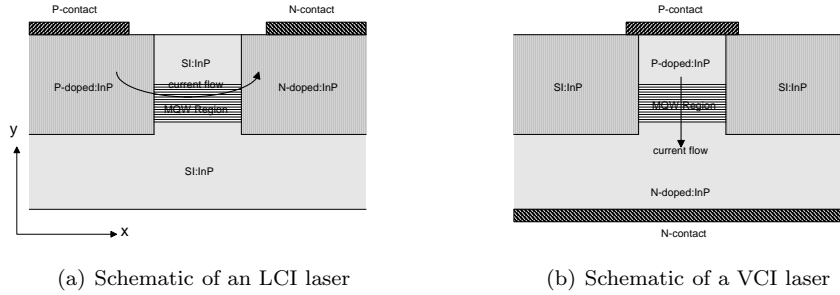


**Figure 3.11.** Schematic of an LCI and VCI laser

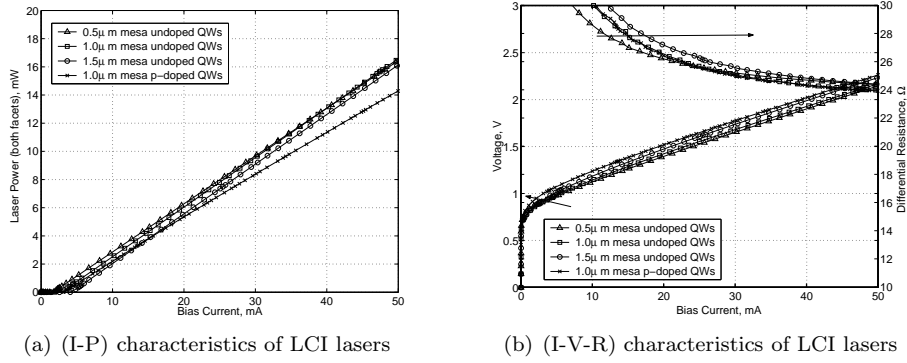


**Figure 3.12.** DC-characteristics of LCI lasers with different mesa widths and doping

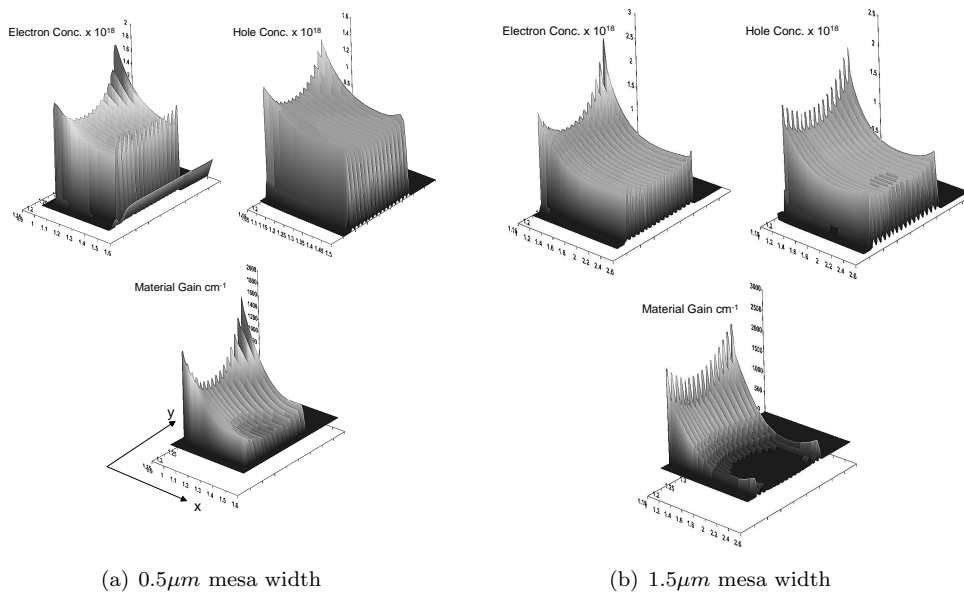


**Figure 3.13.** Carrier and gain distribution in the MQW region



## Chapter 4

# Characterisation of MQW Active Region and Lasers

### 4.1 Introduction

In order to improve the performance of multiple quantum-well based active region of a directly modulated laser, we need to do different experimental measurements to verify the device simulation results and to further optimize the quantum well structures. In this chapter, an introduction is given about the experimental methods used in this thesis to characterise different quantum well structures and corresponding semiconductor lasers. These experimental methods are used to evaluate the newly grown InGaAsP/InGaAlAs quantum wells and compare them with the traditional InGaAsP/InGaAsP quantum well structure. For a large number of quantum wells in the active region, the carrier transport from well to well is important for good static as well as dynamic performance. Ti:Sapphire femto-second pulsed laser excitation and time-resolved photo-luminescence up-conversion technique is utilized to measure the ambipolar carrier transport through MQWs. To compare carrier transport measurement results with the laser performance, semi-insulating re-grown buried heterostructure Fabry-Perot lasers were fabricated from similarly grown MQWs and their static and dynamic performance was evaluated. The modal optical gain spectra and chirp can be deduced from the the amplified spontaneous emission (ASE) measurement collected from one facet of the FP laser below threshold. To measure the microwave modulation properties of the laser, small-signal measurements are performed to compare the dynamic performance of different lasers. From these small signal measurements, one can extract the important parameters such as K-factor, D-factor, differential gain, gain compression factor and parasitic cut-off frequency. The work presented in this chapter is published in **Paper G, H and I.**

## 4.2 Transient PL Measurement

### 4.2.1 Measurement Setup

Time and wavelength resolved PL are measured using a PL up-conversion technique [73], based on a self mode-locking Ti:Sapphire laser (repetition rate 76 MHz, central wavelength 780 nm, pulse duration 130 fs) as shown in figure 4.1. A 1 mm thick LiIO<sub>3</sub> crystal, a 0.5 m spectrometer with a liquid N<sub>2</sub>-cooled CCD detector are used for sum-frequency generation and its spectrally resolved detection. A symbolic diagram is shown in figure 4.2 to explain how the time resolution can be obtained by the temporal overlap of the luminescence signal from the sample and the delayed laser pulse falling on the non-linear crystal and generating the sum-frequency. The wavelength (or energy) resolution is obtained by rotating the crystal to get phase-matching for a particular wavelength as shown in figure 4.1.

In our setup, the laser pulses are focused onto the sample with a spot size of around 60  $\mu\text{m}$  and the average pulse excitation can be varied from 10-400 mW using neutral density filters. Taking into account the surface reflectivity (0.32) of InP and the absorption length  $L = \alpha^{-1} = 300\text{nm}$  at 780nm where  $\alpha$  is the absorption coefficient, the average photoexcited carrier density per pulse can be varied from  $1 \times 10^{16} \text{ cm}^{-3}$  to  $5 \times 10^{18} \text{ cm}^{-3}$  depending upon the excitation power per pulse. The temporal resolution of the measurement setup depends upon the minimum displacement of the delay stage and is around 200 fsec.

### 4.2.2 MQW Carrier Transport Test Structure

A special test structure is needed to do the time and wavelength resolved PL measurement with sub picosecond time resolution. A schematic band diagram of the test structure used for carrier transport measurements is shown in figure 4.3. The test structure works through generation of photoexcited carriers in the top InP absorption layer by a laser pulse, and their time-delayed detection in a deeper QW region after passing through a number of shallow transport QWs [74]. The structures can be undoped, p-doped or n-doped to investigate the ambipolar carrier transport, electron transport and hole transport respectively. On the InP substrate, after growing a 200 nm InP buffer layer, a quaternary InGaAsP Q1.4 50nm thick layer is grown to block the photo generated carriers underneath the sample from falling into the detection well and generating a false signal. A deeper InGaAs 10nm well with  $\lambda_g = 1650\text{nm}$  is grown to serve as a marker well in the time-resolved PL measurements. Then any number of shallow InGaAsP transport quantum wells  $\lambda_g = 1550\text{nm}$  ( here 6 wells are shown ) of the same composition are grown. On top of the shallow transport QWs, an undoped 600nm thick InP cap layer is grown to absorb the excitation laser pulses and generate carriers.

Most of the 780nm laser pulse is absorbed in the top InP cladding over its absorption length and generates photoexcited carriers. These carriers start to

diffuse ambipolarly toward the shallow QWs and hence the PL signal from the InP cladding decays exponentially  $\exp(-t/\tau_1)$  with a time-constant  $\tau_1$  which is mainly limited by the carrier diffusion. As more carriers travel to the shallow QWs, the PL signal from the shallow QWs at 1550nm start to increase exponentially  $(1 - \exp(-t/\tau_2))$  with a time-constant  $\tau_2$ . The time-constant  $\tau_2$  depends on the diffusion of the photogenerated carriers from the top InP layer and subsequent diffusion and capture among the shallow QWs. Therefore,  $\tau_2$  is nearly equal to  $\tau_1$ . Progressively the carriers move from the shallow QWs to the deep QW and the PL signal at 1650nm increases exponentially  $((1 - \exp(-t/\tau_3)))$  with a time-constant  $\tau_3$ . The time constant  $\tau_3$  is mainly dependent upon the time it takes for the carriers to pass over all the shallow QWs. The difference  $\tau^* = \tau_3 - \tau_1$  between the time-constants can be taken as the effective time taken by the carriers to travel the shallow QWs active region of thickness  $L$  with effective velocity  $v^*$  and effective diffusion constant  $D^* = L^2/\tau^*$  [75].

The measured transient PL signal from the shallow and the deep QW form a test structure (shown in figure 4.3) is given in figures 4.4(a) and 4.4(b). In **Paper G**, a least-square curve fit is done on the measured data with a fitting function of the form  $PL(t) = A_0 + A_1 \exp(-t/\tau)$  to extract the exponential time-constant  $\tau_2$  and  $\tau_3$  at 1550nm and 1650nm. From these time constants, one can estimate the effective carrier transport time constant  $\tau^*$ , the effective diffusion constant  $D^*$  [75] and the quality of the grown material from the PL decay time constant in the shallow wells. By measuring the transport time for different well-barrier combinations having different composition (such as InGaAsP and InGaAlAs) and bandgaps, one can optimize the quantum well structure to be used in the active region of a laser. This method helps design a direct modulated laser where a large number of quantum wells (such as 16, 20 or more) are needed in the active region to improve the confinement factor as well as the differential gain.

### 4.3 FP-Laser Characterisation

A broad-area Fabry-Perot laser is perhaps the simplest semiconductor laser cavity that can be made in minimum number of growth and processing steps. From such a structure, we can determine light-current and current-voltage relationship of the laser diode. More complicated structures having single transverse mode such as buried heterostructure (BH) waveguide laser or ridge waveguide laser can be made. BH lasers make it possible to accurately determine the current density in the active region, do optical gain and chirp measurements as well as high speed microwave measurements.

In **Paper G**, Fabry-Perot laser structures were grown from similar QWs as were used in the carrier transport measurements. This helps further determine the performance of different QWs in actual lasing situation. Devices were processed into semi-insulating buried-heterostructure (SIBH) lasers by dry etching of different mesa widths and semi-insulating Fe:InP regrowth up till the contact

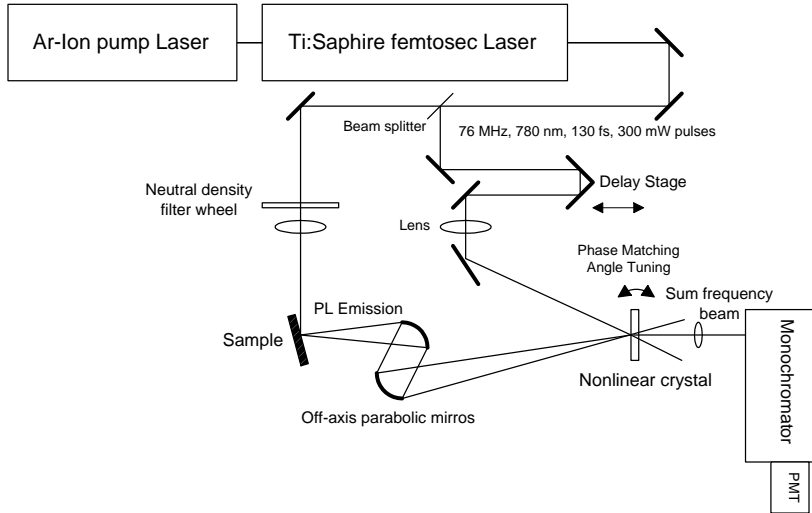


**Figure 4.1.** Time and wavelength resolved PL upconversion setup

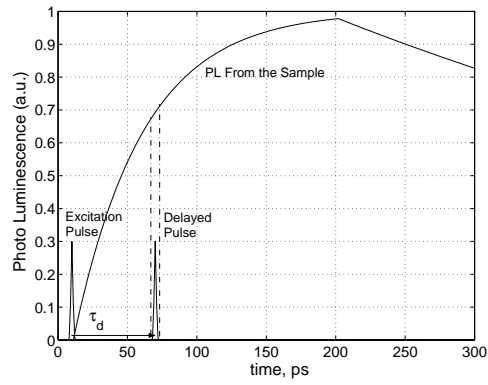


**Figure 4.2.** Time-resolved PL measurement operation principle

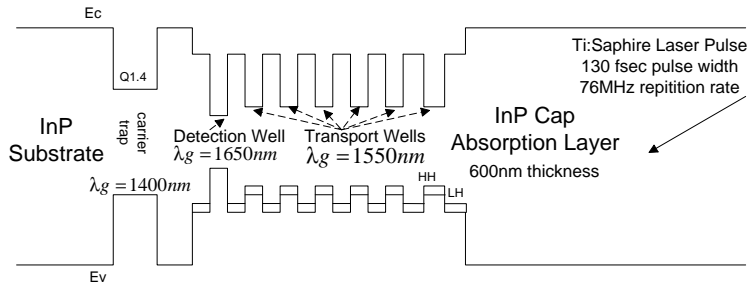
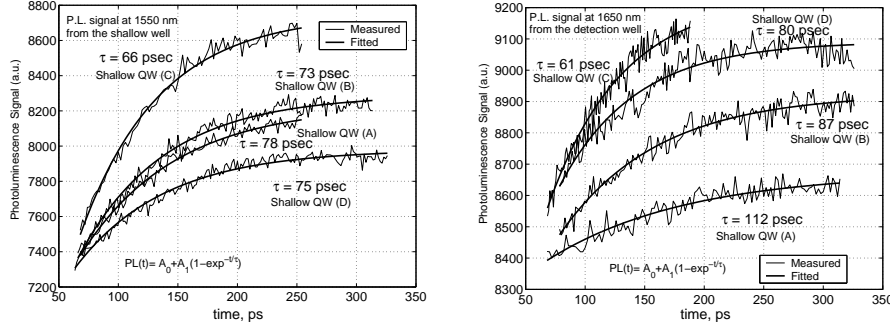


**Figure 4.3.** MQW carrier transport test structure band diagram





(a) Transient PL signal at 1550nm from the shallow transport quantum wells (b) Transient PL signal at 1650nm from the deep detection quantum well

**Figure 4.4.** Transient PL signal from the deep and the shallow QWs

layer. The SIBH structure confines the current to the active region of the mesa and improves the heat dissipation as well at high forward bias current of the laser. Thus we can have a good estimate about the current density in the active region and calculate the threshold current density  $J_{th}$  and internal efficiency  $\eta_i$  accurately. A layer structure is given in figure 4.5(a) for Laser-(B16). Laser-(B16) has 16 undoped QWs, no separate confinement heterostructure (SCH) layer around the QWs and the mesa width is  $1.8 \mu\text{m}$  resulting in an estimated confinement factor  $\Gamma = 0.278$ . Another similar laser with 20 QWs is also grown and processed into semi-insulating flat buried-heterostructure (SIFBH) [76] by growing an extra p-cladding layer on top of the SI layer. The cavity length can be defined by cleaving of the facets and can be from  $100 \mu\text{m}$  to  $2000 \mu\text{m}$  typically used for such evaluation.

#### 4.3.1 Light-Current and Voltage-Current Measurements

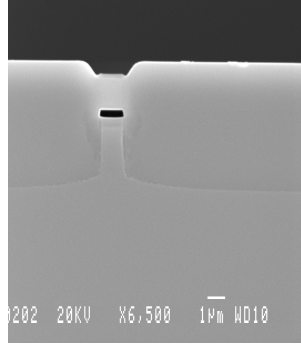
For this measurement, laser chips are usually mounted on a subcarrier and placed on a copper heat sink with a temperature controller as shown in figure 4.6. Light-current static measurements are performed with pulsed as well as continuous current injection at different temperatures. The light output from one facet is collected using an integrating sphere and a calibrated detector.

The output power  $P_o$  from one facet of a laser as a function of the injected current  $I$  is given by the relationship [30]:

$$P_o = \eta_d \frac{h\nu}{2q} (I - I_{th}) \quad (4.1)$$

where  $I_{th}$  is the threshold current. From this measurement, the  $\eta_d$  can be calculated from the slope of the L-I curve. The differential efficiency  $\eta_d$  is also defined as [30]:

In <sub>0.53</sub> Ga <sub>0.47</sub> As Contact Layer, 0.2 $\mu$ m, p++
InP Cladding Layer, 1.5 $\mu$ m, p+ doping
In <sub>0.41</sub> Ga <sub>0.43</sub> Al <sub>0.16</sub> As Barrier, 0.83%TS, 8nm, undoped $\lambda_g = 1350nm$
<div style="display: flex; align-items: center;"> <div style="border: 1px dashed black; padding: 2px; margin: 2px;"> In<sub>0.75</sub>Ga<sub>0.25</sub>As<sub>0.8</sub>P<sub>0.2</sub> Well, 0.95%CS, 8nm, undoped <math>\lambda_g = 1550nm</math> </div> <div style="margin-left: 10px;"> 16 periods </div> </div>
In <sub>0.41</sub> Ga <sub>0.43</sub> Al <sub>0.16</sub> As Barrier, 0.83%TS, 8nm, undoped $\lambda_g = 1350nm$
InP Buffer Cladding Layer, 500nm, n+
InP Substrate n++ <001>



(a) FP-Laser (B16) epitaxial layer structure

(b) FP-Laser (B16) cross-section SEM image

**Figure 4.5.** FP-Laser (B16) epitaxial structure and cross-section SEM image

$$\eta_d = \frac{\eta_i \alpha_m}{\alpha_i + \alpha_m} \quad (4.2)$$

where  $\alpha_i$  is the modal background loss of the laser cavity and  $\alpha_m$  is the mirror loss defined as [30]:

$$\alpha_m = (1/L) \ln(1/r_1 r_2) \quad (4.3)$$

where  $L$  is the length of the laser cavity and  $r_1$ ,  $r_2$  are the facet amplitude reflection coefficients. By measuring similar devices having different lengths (such as 200, 400, 600, 1000  $\mu$ m), using the relationship:

$$\eta_d^{-1} = \frac{\alpha_i L}{\eta_i \ln(1/r_1 r_2)} + \eta_i^{-1} \quad (4.4)$$

and plotting  $\eta_d^{-1}$  against cavity length  $L$ , one can estimate the internal efficiency  $\eta_i$  and the background modal loss  $\alpha_i$  of the structure under investigation [30]. One must also know the modal facet reflectivity  $r_1$  and  $r_2$  of the waveguide mode which can be usually calculated from the methods described in chapter 2.

The semiconductor injection laser behaves below threshold as a p-n junction diode with  $I - V$  characteristics of the form [30]:

$$I_d = I_r (e^{qV_d/\eta kT} - 1) \quad (4.5)$$

where  $I_r$  is the reverse leakage current,  $V_d$  is the voltage across the p-n junction and  $\eta$  is the ideality factor of the diode. From the  $I - V$  measurements (both forward and reversed bias), one can calculate the diode turn-on voltage which is

approximately equal to the bandgap of the active region, diode static series resistance  $R = V_d/I_d$  and differential resistance  $r = \partial V_d/\partial I_d$  and reverse saturation current. In addition, these measurements help us estimate any shunt current leakage paths around the p-n junction which may degrade the laser static and dynamic performance.

For measurements at elevated temperature  $T$ , the threshold current can be approximated as:

$$I_{th}(T) = I_0 e^{T/T_0} \quad (4.6)$$

where  $I_0$  and  $T_0$  are phenomenological factors. The important factor  $T_0$  describes the temperature dependence of the laser threshold current and can be estimated from the threshold current measurements at different temperatures (usually from 20° C to 80 °C) and doing the curve fitting to extract  $T_0$ .

In **Paper G**, such measurements are done at different heat-sink temperatures varying from 20 °C up to 120 °C. Pulsed L-I measurement results for Laser-B16 are given in figure 4.7(a). From this measurement, the differential efficiency  $\eta_d$ , threshold current  $I_{th}$ , threshold current density  $J_{th}$  and  $T_0$  of the device is calculated. Similarly laser-B20 is also measured and the results are given in figure 4.8(a). The extracted parameters for both lasers are given in table 4.1. The laser-B16 had high series resistance due to bad p-contact, which explains the increased threshold current as compared to the laser-B20.

### 4.3.2 Optical Gain and Chirp Measurements

Optical gain represents the coherent amplification of an electromagnetic field as it passes through a laser cavity. For a plane wave, the intensity material gain  $g$  can be related to the imaginary part  $n_i$  of the refractive index, that is  $g = 4\pi n_i/\lambda_o$  where  $\lambda_o$  is the free space wavelength. For a waveguide structure commonly used in semiconductor lasers, the guided electromagnetic wave is in the form of a transversely confined mode. Hence, the gain experienced by the mode is called modal gain and equal to  $\Gamma g$  where  $\Gamma$  is the modal confinement factor defined as the fraction of the transverse modal intensity confined to the active region of the laser.

The modal optical gain (or loss) measurements in a single transverse-mode optical waveguide structure are usually performed using the Hakki-Paoli method [77–79]. The FP-laser is biased below threshold and the amplified spontaneous emission (ASE) is collected from one of the facets of the laser using an

Laser No.	$J_{th}/\text{well at}$ 20°C, $A/cm^2$	$\eta_d$ at 20°C	$T_0$ 20-80°C
B16	260	0.48	74
B20	95	0.45	78

**Table 4.1.** FP-Lasers DC characterisation results

anti-reflection coated lens coupled to a single mode fiber with a built-in polariser/isolator. The net modal gain is obtained from the ratio of maximum intensity  $I_{max}$  and minimum intensity  $I_{min}$  of the ASE.

$$G_{net} = \Gamma g - \alpha_i = \frac{1}{L} \ln\left(\frac{S-1}{S+1}\right) + \alpha_m. \quad (4.7)$$

where  $S = \sqrt{I_{max}/I_{min}}$  and  $\alpha_m$  is the mirror loss. A more accurate method, used in **Paper G**, to measure optical gain for an FP cavity is by using the analytical expression to fit the amplified spontaneous emission (ASE) [80].

$$ASE(\nu) = \frac{(1-r_1^2)(e^{gL}-1)(1+r_2^2e^{gL})}{(1-r_1r_2e^{gL})^2 + 4r_1r_2e^{gL}\sin^2(kL)} \frac{\eta_{sp}}{\eta_i} \frac{h\nu}{2} \quad (4.8)$$

where  $k = 2\pi/\lambda$ ,  $\eta_{sp}$  is the population inversion factor and  $\eta_i$  is the internal efficiency.

The chirp or alpha parameter  $\alpha_H$  is a material parameter which shows the inter-dependence of the real and the imaginary parts of refractive index of a material through Kramers-Krong relationship [30]. It is defined as follows:

$$\alpha_H = \frac{\delta n_r / \delta N}{\delta n_i / \delta N} = \frac{4\pi n_g}{c} \frac{\delta f / \delta I}{\delta(\Gamma g - \alpha_i) / \delta I} \quad (4.9)$$

where  $n_r$  and  $n_i$  are the real and the imaginary parts of the waveguide modal index respectively,  $n_g$  is the waveguide group modal index and  $N$  is the carrier density in the active region. The chirp factor  $\alpha_H$  is calculated from the measured shift in the FP resonance peak  $\delta f$  and the differential gain  $\delta(\Gamma g - \alpha_i)$  as a differential current  $\delta I$  is applied to the laser below threshold [79]. However, such a measurement also includes the thermal chirp, that is the red shift in the FP resonance due to the heating of the laser when a current step is applied. The chirp factor  $\alpha_H$  is an important parameter for directly modulated laser and it is related to the frequency change of the laser during modulation. The frequency chirping  $\delta f$  in a directly modulated laser is given by [30]:

$$\delta f = \frac{\alpha_H}{4\pi} \Gamma v_g a \delta N \quad (4.10)$$

Hence a smaller  $\alpha_H$  is desired in order to avoid the dispersion and corresponding spreading of the optical pulsed when a directly modulated laser is used for high speed data transmission through standard single mode fiber.

In **Paper G**, gain measurement of the laser (B16) are done and the results are given in figure 4.7(b). A facet reflectivity of 0.3 is assumed to calculate the mirror loss. Similarly, gain measurements of the laser-B20 are given in figure 4.8(b). The differential modal gain  $dG/dJ$  was calculated from the fitted modal gain, and the results are given in figure 4.9(a). The results for the chirp measurement are shown in figure 4.9(b) for the laser-(B16) and laser-B20. Even though the laser-B20 has higher differential gain  $dG$ , it has poor  $\alpha_H$  as compared to the laser-B16. This can possibly be due to the excessive heating of the laser-B16

due to poor p-contact and the resulting red shift which compensates the blue shift due to the current step and thus the  $\alpha_H$  is underestimated. The gain and chirp measurements indicate that by operating the laser to the left side of the gain peak (e.g. by a DBR or DFB grating), one can get higher differential gain and reduced chirp which is advantageous to increase the laser bandwidth and reduce dispersion.

### 4.3.3 Small-Signal Modulation Response Measurements

Small-signal modulation response measurements are performed on the laser chips using a network analyzer and high speed calibrated detector [76]. A schematic diagram of the setup is given in figure 4.10. The measured response at different bias current is usually fitted to a 3-pole transfer function of the form:

$$H(\omega) = \frac{Const.}{(-f^2 + j\frac{f}{2\pi}\gamma + f_r^2)(jf + f_p)} \quad (4.11)$$

The damping constant  $\gamma$ , resonant frequency  $f_r$  and parasitic frequency  $f_p$  are extracted at each bias current from this fitting procedure. The K-factor of each laser is obtained by fitting  $\gamma$  and  $f_r^2$  at different biases to a straight line of the form  $\gamma = \gamma_o + Kf_r^2$ . Similarly the D-factor of the laser is obtained by the relationship  $f_r = D\sqrt{I - I_{th}}$  at low bias. The K-factor and D-factor are also given by the relationships [76]:

$$K = 4\pi^2(\tau_p + \frac{\epsilon}{v_g a}) \quad (4.12)$$

and

$$D = \frac{1}{2\pi} \sqrt{\eta_i \frac{\Gamma v_g a}{qV}} \quad (4.13)$$

where  $\tau_p$  is the photon lifetime,  $a = dg/dn$  is the material differential gain vs carrier density,  $\epsilon$  is the non-linear gain compression factor,  $v_g$  is the modal group velocity,  $\Gamma$  is the optical confinement factor and  $V$  is the active region volume. By such measurements, one can extract differential gain  $a$  and gain compression factor  $\epsilon$  of a device. These parameters give us very useful information about the dynamic performance of the active region and help compare different quantum wells for high speed operation.

The laser maximum achievable bandwidth can be limited either by the parasitics  $f_{3dB,par} = (2 + \sqrt{3})f_p$ , or by the damping limit  $f_{3dB,damp} = 2\sqrt{2}\pi/K$  [30], or by thermal effects which give a maximum relaxation frequency  $f_{r,max}$  that occurs at a bias current earlier than the other limits are reached. The thermal limit can be written as  $f_{3dB,therm} = \sqrt{1 + \sqrt{2}}f_{r,max}$  [76].

In **Paper G**, small-signal measurements of the laser-B(16) are done and the extraction results are given in table 4.2. These results indicate that the Laser-B(16) bandwidth is limited by thermal effects.

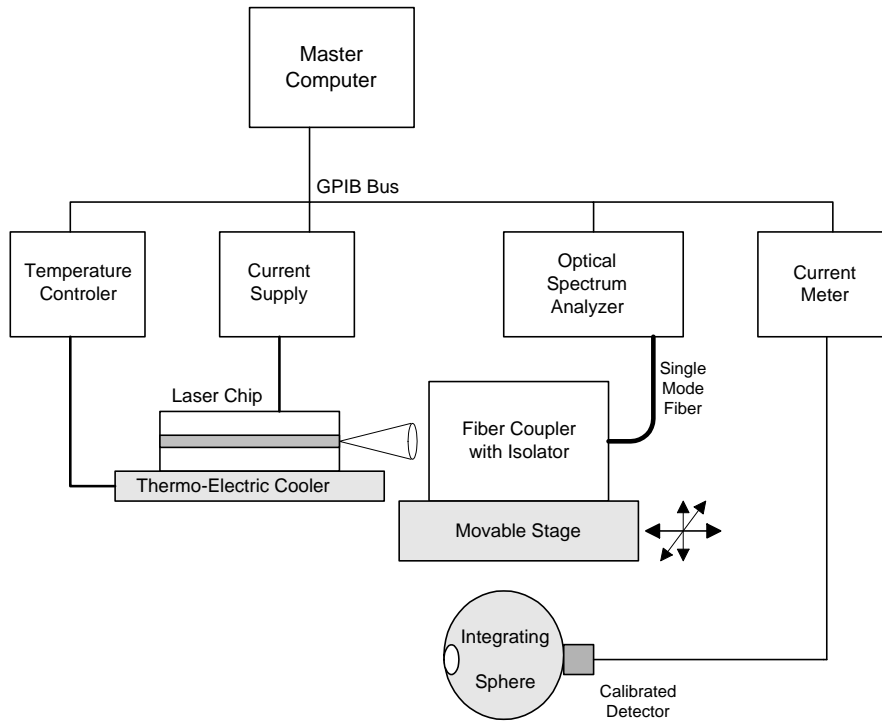
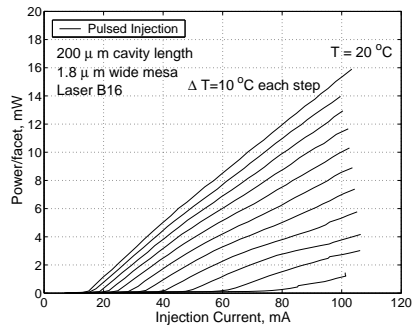
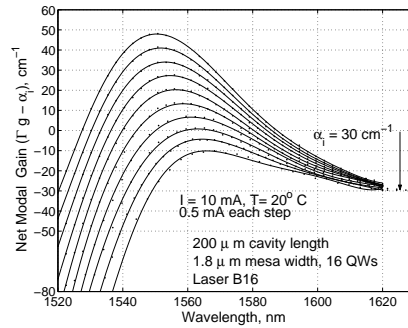


Figure 4.6. DC light-current and gain measurement setup

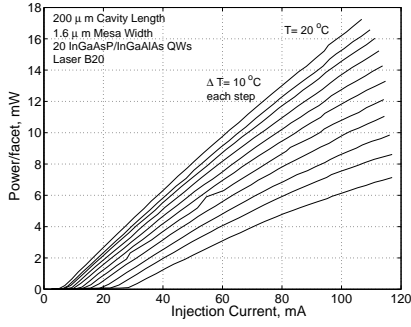


(a) FP-Laser (B16) pulsed light-current measurements

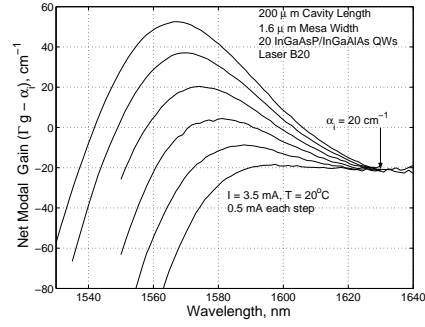


(b) FP-Laser (B16) gain measurement

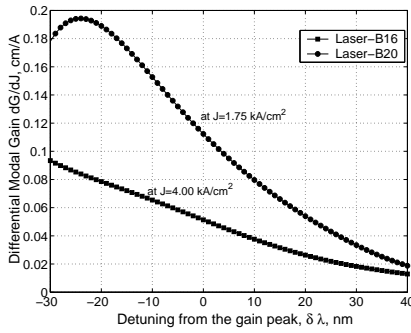
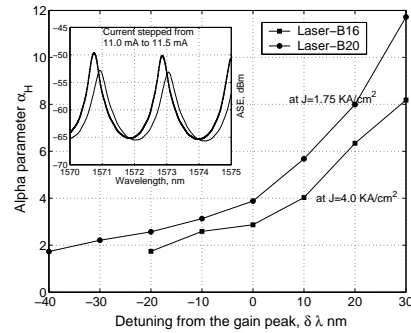
Figure 4.7. FP-Laser (B16) light-current and gain measurement



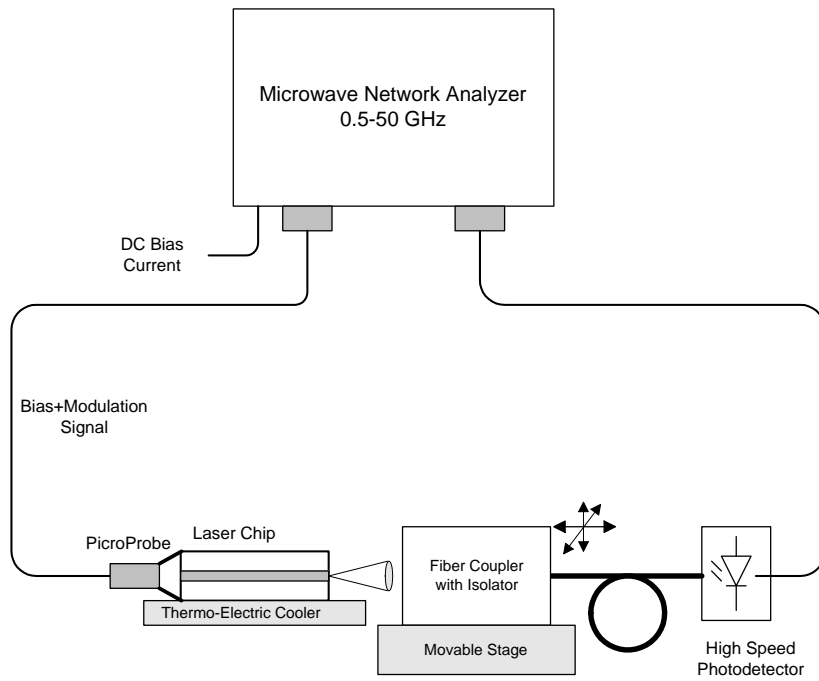
(a) FP-Laser (B20) pulsed light-current measurements



(b) FP-Laser (B20) gain measurement

**Figure 4.8.** FP-Laser (B20) light-current and gain measurement(a) FP-Laser (B16) and (B20) differential modal gain  $dG/dJ$  measurement below threshold(b) FP-Laser (B16) and (B20) chirp parameter  $\alpha_H$  measurement below threshold**Figure 4.9.** Differential modal gain and chirp measurement of the laser

Laser No.	K-factor ns	D-factor $\frac{GHz}{\sqrt{mA}}$	$f_{3dB,damp}$ GHz	$f_{3dB,par}$ GHz	$f_{3dB,therm}$ GHz	$f_{3dB,real}$ GHz
B16	0.256	2.0	34.7 GHz	22.4	17.2	11.8

**Table 4.2.** FP-Lasers small-signal characterisation results**Figure 4.10.** Small-signal modulation response measurement setup



## 4.4 Wide-Band Directly Modulated DBR Laser

The possibility of broad band direct current modulation is an attractive feature of semiconductor lasers and such lasers are potential candidates for low cost short distance digital communication. In digital applications, the laser diode is turned on and off to produce optical pulses for the transmission of information. In analog links, the laser drive current and therefore its optical output is varied in an analog fashion for the transmission of RF signals on the optical carrier. Analog fiber optic links are used for the distribution of radio-frequency and microwave signals over optical fiber in cable-TV and wireless communication applications. For high-frequency, wide band and low-distortion fiber-optic microwave links, a DFB or DBR laser, capable to be modulated to more than 30 GHz, is a possible source. One of the techniques used to achieve such high bandwidth is detuned loading, which increases the interaction between the photons and the free carriers in the laser cavity [81]. This increased interaction not only increases the modulation bandwidth, but also reduces the variation in the optical gain during the modulation. It can therefore reduce the signal distortion and increase the linearity of the laser diode.

### 4.4.1 DBR Laser Structure

A two-section high speed DBR-laser with one active section and one DBR section is shown in figure 4.11. These lasers have 100-200  $\mu\text{m}$  active section and 300  $\mu\text{m}$  passive Bragg-section with a coupling coefficient estimated to be about  $80\text{ cm}^{-1}$ . The active structure consists of 16  $\text{In}_{0.74}\text{Ga}_{0.26}\text{As}_{0.85}\text{P}_{0.15}$  wells, 7 nm thick with 1 % compressive strain, separated by  $\text{In}_{0.46}\text{Ga}_{0.54}\text{As}_{0.85}\text{P}_{0.15}$  barriers, 8 nm thick with 0.9 % tensile strain. The active structure is surrounded by an asymmetrical box separate confinement layer (SCL) of 10 nm InGaAsP  $\lambda_g = 1.3\mu\text{m}$  on the p-side and 40 nm on the n-side, all layers are doped  $1 \times 10^{18}\text{ cm}^{-3}$ . The grating section consists of a 10 nm InP buffer layer, a waveguide consisting of bulk  $\lambda_g = 1.3\mu\text{m}$ . On top of the waveguide is an InP spacer layer of 40 nm thickness followed by a bulk  $\lambda = 1.3\mu\text{m}$  grating layer. The lasers have a thin film resistor on top off the Bragg section and the Bragg wavelength can be tuned thermally by a lateral current through the resistor. The transverse structure used for current confinement is called semi-insulating flat-surface buried heterostructure (SI-FBH) with ground-source-ground (GSG) contact configuration.

### 4.4.2 40 Gb/s Transmission

Using such high bandwidth DBR laser, successful transmission experiments at 10 and 20 Gb/s have been performed through 125 and 30 km of standard single-mode-fiber (SMF), respectively [82, 83]. However, few transmission experiments have been done using directly modulated lasers at 40 Gb/s [84]. In **Paper H**, successful 40 Gb/s digital transmission experiment is done for back-to-back (B-B) transmission and through 1 km of standard SMF with these lasers. A 40 Gb/s

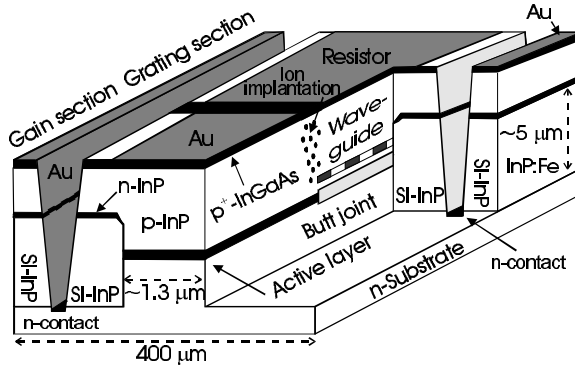


**Figure 4.11.** Schematic picture of a two-section DBR Laser with Ground-Source-Ground contact

parallel bit-error-ratio tester (ParBERT 81250 45G from Agilent) is used in this experiment. The schematic diagram of the experimental setup is shown in figure 4.12. A  $(2^5 - 1)$  pseudo-random bit sequence AC-drive signal (2 Vp-p) is fed to the laser using a Picoprobe ground-signal-ground high frequency probe directly on the laser. The laser output is collected by a fiber with an integrated lens and an optical isolator and detected by the optical input of the ParBERT. Error free performance for greater than one minute operation is observed back-to-back and after 1 km of standard SMF. For B-B transmission, the BER decreases without any error floor as the received power is increased. A  $\text{BER} < 10^{-10}$  is achieved at -2 dBm received average optical power. A  $\text{BER} < 10^{-8}$  is obtained through fiber for 2 dBm received power. The 40 Gb/s eye diagrams B-B and at 1 km of fiber are shown in Figure 4.13. The eye diagram for B-B is clearly open but exhibits a pattern dependence. After 1 km of fiber the eye opening is smaller, but with a more optimized electrical set up the input signal and the eye opening would probably improve. The extinction ratio is approximately 3 dB in both eye diagrams and during the BER measurements.

#### 4.4.3 Analog Distortion in DBR Laser

Directly modulated lasers can also be used for analog transmission of microwave signal on the optical carrier such as for radio-over fiber applications, cable television, wireless distributed antenna system and microwave radar links [85]. A major concern in an analog optical link is the linearity of the laser at the microwave modulation frequency. Distortion, defined as the appearance of frequencies other than the modulation frequency, occurs if time-dependent variables multiply or

occur in non-linear terms. From the rate equations 3.1, 3.2, one can see that if carrier density  $N(t)$  changes during modulation, then the terms  $g(N, t)S(t)$  and  $R_{sp}(N(t))$  produce distortion.

In order to define the non-linearity of a laser, the output optical power is expressed as a polynomial function of the input current, that is:

$$P_o(t) = a_1 I_{in}(t) + a_2 I_{in}^2(t) + a_3 I_{in}^3(t) + \dots \quad (4.14)$$

Now suppose the input current is  $I_{in}(t) = A \cos(\omega_o t)$ , then the output is:

$$P_o(t) = a_1 A \cos(\omega_o t) + a_2 (A \cos(\omega_o t))^2 + a_3 (A \cos(\omega_o t))^3 + \dots \quad (4.15)$$

$$= \frac{a_2 A^2}{2} + (a_1 A + \frac{3a_3 A^3}{4}) \cos(\omega_o t) + \frac{a_2 A^2}{2} \cos(2\omega_o t) + \frac{a_3 A^3}{4} \cos(3\omega_o t) + \dots \quad (4.16)$$

The output consists of the fundamental frequency  $\omega_o$  and the higher order harmonics  $2\omega_o, 3\omega_o$  etc. The harmonic distortion is defined as the ratio of the amplitude of particular harmonic frequency to the amplitude of the fundamental frequency, for example the second-order distortion  $HD2$  can be defined as:

$$HD2 \approx \frac{a_2 A}{2a_1}, \text{ if } a_1 A \gg \frac{3a_3 A^3}{4} \quad (4.17)$$

If two microwave signals having close frequencies such as  $\omega_1$  and  $\omega_2$  are fed to the laser, then the mixing products, called intermodulation products, occur at the output (see figure 4.15). If we assume an input signal of the form  $I_{in}(t) = A \cos(\omega_1 t) + A \cos(\omega_2 t)$ , then the output is:

$$P_o(t) = a_1 A (\cos(\omega_1 t) + \cos(\omega_2 t)) + a_2 A^2 (\cos(\omega_1 t) + \cos(\omega_2 t))^2 + a_3 A^3 (\cos(\omega_1 t) + \cos(\omega_2 t))^3 + \dots \quad (4.18)$$

and using trigonometric identities, the second and third-order intermodulation can be found as:

$$\omega_1 \pm \omega_2 : a_2 A^2 \cos(\omega_1 + \omega_2)t + a_2 A^2 \cos(\omega_1 - \omega_2)t \quad (4.19)$$

$$2\omega_1 \pm \omega_2 : \frac{3a_3 A^3}{4} \cos(2\omega_1 + \omega_2)t + \frac{3a_3 A^3}{4} \cos(2\omega_1 - \omega_2)t \quad (4.20)$$

$$2\omega_2 \pm \omega_1 : \frac{3a_3 A^3}{4} \cos(2\omega_2 + \omega_1)t + \frac{3a_3 A^3}{4} \cos(2\omega_2 - \omega_1)t \quad (4.21)$$

The terms  $2\omega_2 - \omega_1$  and  $2\omega_1 - \omega_2$  fall very close to the original frequencies  $\omega_1$  and  $\omega_2$  and are very important from the distortion point of view since they are

difficult to filter out from the original signal. The third-order intermodulation distortion (IMD3) can be defined as the ratio of the amplitude at frequency  $2\omega_2 - \omega_1$  to the amplitude of the fundamental frequency, that is:

$$IMD3 = \frac{3a_3A^2}{4a_1} \quad (4.22)$$

Another useful parameter to characterise the intermodulation distortion in an analog device is the third-order intercept point (IP3) which can be determined by a two-tone power sweep of the modulation signals and plotting the output power of the fundamental and the third-order intermodulation product against the input signal power. The intersection of the fundamental term  $a_1A$  and the third-order term  $3/4a_3A^3$  gives the IP3.

Spurious free dynamic range (SFDR) of an analog device is defined as the range of output ac power over which the fundamental frequency signal is above the noise floor and the third-order intermodulation products (IMD3) are below the noise floor. An example measurement is given showing the SFDR and the IP3 measurement of a laser in figure 4.16.

The experimental setup to measure harmonic and intermodulation distortion consists of two HP 83712-B signal generators with high spectral purity. The signals are combined and dc-bias for the lasers is added through a bias-T (see figure 4.14). Signal and bias are fed to the laser via direct probing on the laser and no matching of the laser (laser resistance  $10\ \Omega$ ) to the  $50\ \Omega$  transmission cable is performed. The light is collected by a lensed fiber with an integrated optical isolator and detected by a 20 GHz bandwidth PIN-detector.

In **Paper I**, the measurement of the fundamental, third-order intermodulation products (IMD3) and noise in the two-tone experiments is done. The modulation response and the distortion in the DBR lasers depend on the bias current and the detuning from the center of the Bragg peak. Measurements are therefor made at different bias currents and at different detuning on the Bragg peak (detuning through heating of the Bragg section). Laser 3637B-13 is characterized in the range 1-19 GHz. It is measured lasing on both the long and short wavelength side of the Bragg peak to evaluate the effect of detuned loading (see figure 4.17). The position on the Bragg reflection curve is controlled by adjusting the Bragg resistor current and detecting when the lasing mode jumps from one side to the other. The resulting SFDR results are plotted in figure 4.18(a) for a bias current of 70 mA. For the long wavelength side, the  $SFDR \geq 102\ \text{dBHz}^{2/3}$  over the whole range with the best value of  $116\ \text{dBHz}^{2/3}$  at 1 GHz. In the range 1-10 GHz,  $SFDR \geq 106\ \text{dBHz}^{2/3}$ . For the short wavelength side, the  $SFDR \geq 98\ \text{dBHz}^{2/3}$  over the whole range with the best value of  $106.5\ \text{dBHz}^{2/3}$  at 1GHz. Figure 4.18(b) gives the input power at the IP3 point for the short and the long wavelength sides of the laser 3637B-13.

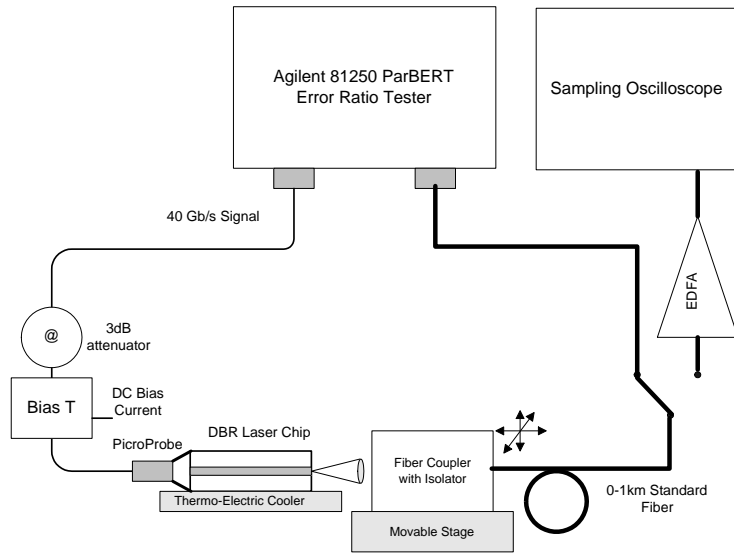


**Figure 4.12.** Measurement set up for the 40 Gb/s measurements on DBR laser

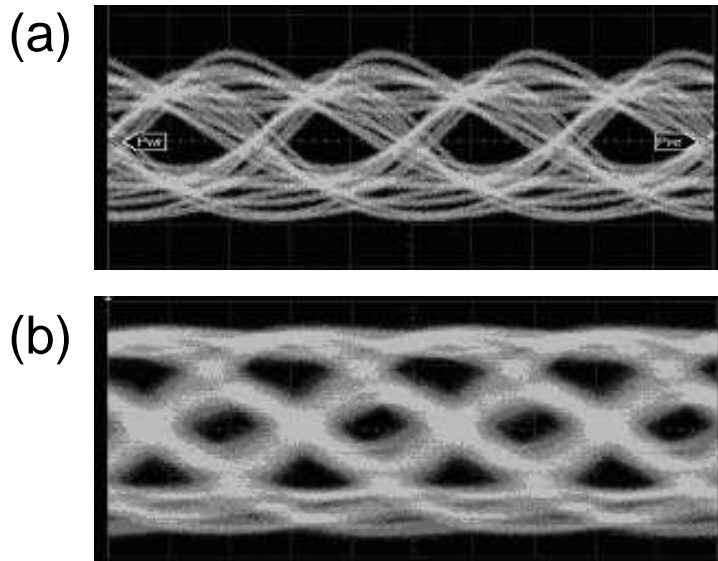


**Figure 4.13.** Eye diagram for 40Gb/sec transmission at 65mA bias and 2 V<sub>p-p</sub> drive voltage (a) back-to-back (b) through 1 km of standard SMF

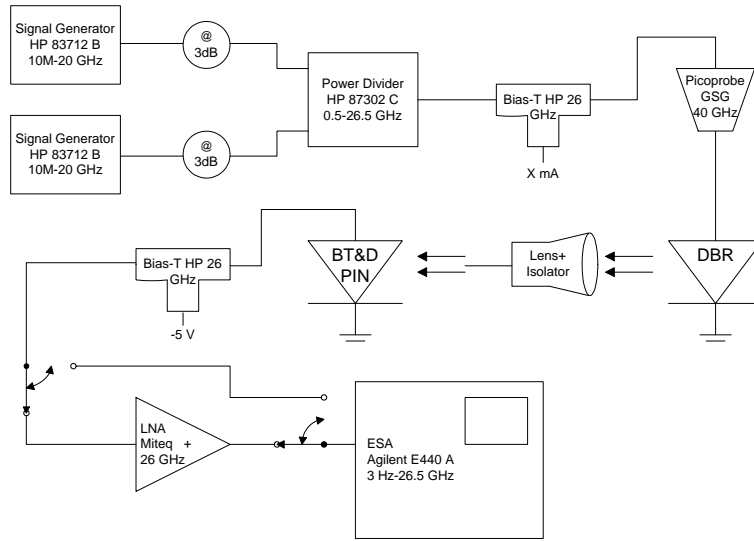


**Figure 4.14.** Measurement set up for the two-tone analog measurements of a laser

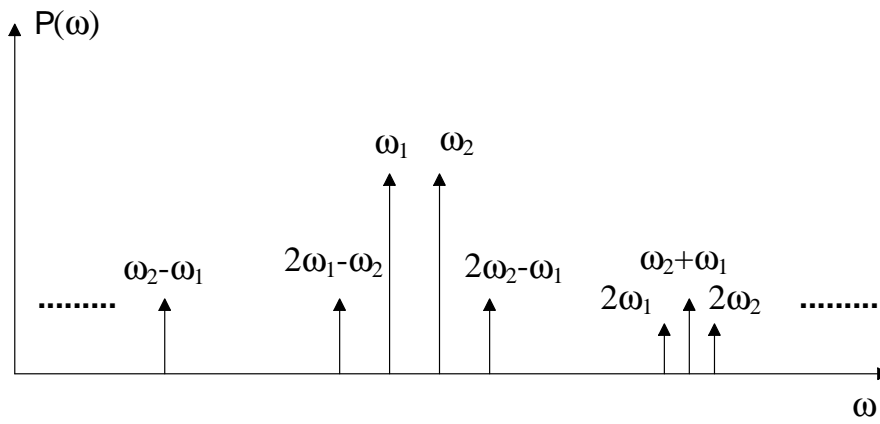


**Figure 4.15.** Laser output spectrum for a two-tone input

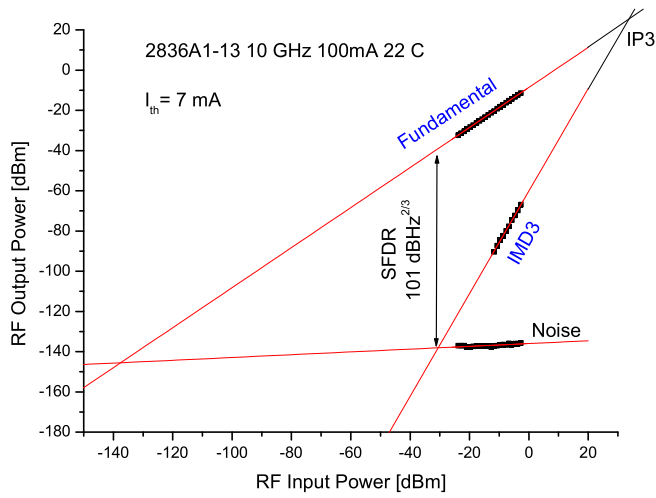


**Figure 4.16.** Fundamental and third-order intermodulation IMD3 measurement for a two-section DBR laser

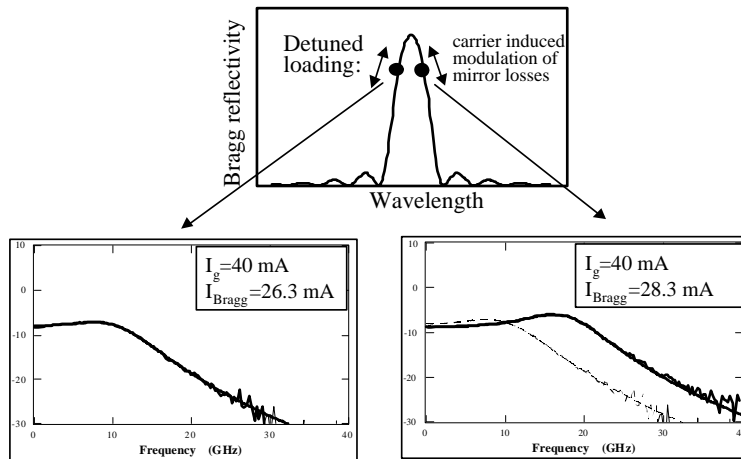
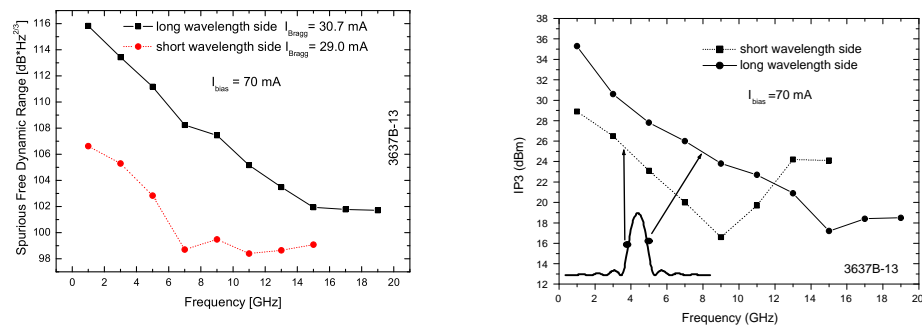


**Figure 4.17.** Small signal modulation response of a DBR laser lasing on the (a) short and (b) the long wavelength side of the Bragg peak. The dotted line in the (b) is the short wavelength response.



(a) SFDR at the long and the short wavelength (b) IP3 at the long and the short wavelength sides of the Bragg peak at bias current of 70 mA of the Bragg peak

**Figure 4.18.** SFDR and IP3 measurements



## Chapter 5

# Summary, Conclusion and Future Work

### Summary and Conclusion:

In the first part of the thesis, the numerical accuracy of the Method of Lines (MoL) is improved by using the higher-order approximations of the transverse second-derivative operator in the Helmholtz equation, and by including the necessary interface conditions for the  $\mathbf{E}$  and the  $\mathbf{H}$  fields. The basic 3-point uniform-mesh approximation of second-derivative operator is extended to the 5-point and 7-point non-uniform mesh formulation at an abrupt transition of refractive-index and/or mesh size. Application of these higher-order schemes to the MoL show substantial improvement in the convergence rate towards the analytical results both for the real and the imaginary parts of the propagation constant. The perfectly matched layer (PML) absorbing boundary condition is used to simulate the open space around the problem space which makes it possible to simulate leaky modes having complex propagation constant.

For beam propagation simulation in waveguides, an efficient Cascading and Doubling Algorithm is derived within the MoL framework and found to be highly efficient and numerically stable in modelling long deep waveguide gratings. It can efficiently model periodic, quasi-periodic, symmetric and asymmetric waveguide gratings by attaching appropriate sections of individual gratings. Grating shapes other than the usual rectangular shape, such as sinusoidal or trapezoidal, can be modelled by sub-dividing one period of the grating into many uniform sections and finding the equivalent reflection and transmission coefficient matrix of one period. Many such periods can then be joined together to get the resultant response.

An new waveguide polarizer filter based on the ARROW grating is proposed and analyzed using the MoL. The ARROW grating structure  $TE$  and  $TM$  modal spectral response is calculated for different configurations. Both a shallow and a deep grating structures are considered. When operating at anti-resonance

(low-loss case), both grating types exhibit a spectral response similar to that of conventional gratings. However, when operating near resonance (high-loss case), the peak reflectivity is reduced in value and the side-lobes are smoothed due to the increase in the leakage loss.

Following conclusions can be drawn from the first part of the thesis.

- The higher-order approximations in the MoL result in reduced matrix size, faster computational speed and lower memory usage. They are useful to simulate high-contrast multilayer structures having large transverse dimensions. The improved scheme can model metals and lossy dielectrics in a unified way without divergence. The use of PML absorbing boundary condition gives accurate value for the imaginary part of the propagation constant, indicating that it accurately simulates the open space around the problem space. Thus one can simulate lossy waveguides, leaky modes as well as scattering from inhomogeneous regions and gratings.
- The Cascading and Doubling algorithm is a versatile bi-directional beam propagation algorithm which is numerically stable even for infinite period grating and does not suffer from divergence. It can correctly calculate the transmission and reflection spectra of both  $TE$  and  $TM$  modes in a waveguide grating. It can also simulate surface plasmon gratings or metal layers gratings since the transverse second-order derivative and the interface conditions are properly implemented. Due to its full-spectrum formulation, it can calculate deep grating spectra where modes other than the guided modes also take part in the energy transfer from one part of the waveguide to the next part. When combined with higher-order approximation, the resulting matrix size is smaller which further improves the speed of the beam-propagation algorithm.
- The polarization discrimination property of the ARROW waveguide causes the ARROW grating to behave as a  $TE$ -pass reflection-mode filter (i.e. a band-pass wavelength filter that strongly reflects  $TE$ -polarized waves, while negligibly reflecting  $TM$  polarized waves). A conventional grating does not exhibit this property. By designing the ARROW with slight loss, the differential loss between the  $TE$  core-mode and the rest of the modes can be increased substantially enhancing the grating polarization, spectral and modal discrimination properties even for deep gratings.

In the second part of the thesis, an InGaAsP compressive well with InGaAlAs tensile barrier combination is explored to improve the performance of InP based  $1.55\ \mu\text{m}$  semiconductor lasers. Theoretical simulations are performed to simulate the effect of varying barrier bandgap for a MQW laser. Confinement energies of  $150\text{meV}$   $\Delta E_c$ ,  $50\text{meV}$   $\Delta E_{v,hh-lh}$  are found to be optimum in terms of material gain, differential gain and carrier and gain uniformity among all the wells. This is contrary to the designs with fewer wells in which barriers with higher bandgap ( $\lambda_g = 1250\text{nm}$ ) are usually employed. For MQWs with high bandgap InGaAlAs

barriers, the electrons can pile up near the n-side, which is in contrast to the MQWs with InGaAsP barriers, where the holes can accumulate near the p-side. Due to the reduced  $\Delta E_v$ , a large number of quantum wells can be efficiently pumped through improved vertical hole transport reducing the carrier density needed to lase in an individual well. The high p-doping of the active region is found to increase the carrier and gain non-uniformity among the wells especially for wells with higher barrier bandgap.

Following on the simulation results, detailed experimental study is performed to measure the carrier transport in a MQW structures using specially grown test structures and time and wavelength resolved PL up-conversion technique. Different QWs with same InGaAsP  $\lambda_g = 1.55 \mu\text{m}$  well and different InGaAsP or InGaAlAs barrier having increasing bandgap (varying from  $\lambda_g = 1.26 \mu\text{m}$  to  $1.44 \mu\text{m}$ ) are grown. The InGaAsP/InGaAlAs quantum well with  $\lambda_g = 1.42 \mu\text{m}$  has equally fast carrier transport as the traditional InGaAsP/InGaAsP quantum well even through the electron confinement  $\Delta E_c$  is almost twice in the InGaAsP/InGaAlAs well structure. This fact can help us design uncooled lasers with high modulation bandwidth. SIBH FP-lasers are fabricated from similar wells and their static characteristics (including optical gain and chirp spectra below threshold), thermal characteristics and dynamic response are evaluated. Lasers with  $\lambda_g = 1.35 \mu\text{m}$  InGaAlAs barrier having 16 and 20 wells showed improved high temperature operation, higher optical gain, higher differential gain and lower chirp as compared to the lasers with optimized InGaAsP barrier.

Detailed 2D self-consistent simulations are performed to explore the lateral current injection (LCI) laser concept. It is found that a narrow mesa width ( $< 1 \mu\text{m}$ ) with undoped active region is required to improve the carrier and the gain uniformity in such a laser. The p doping of the active region will increase the carrier and gain non-uniformity. Moreover, the carrier leakage from the active region and current leak from the top and bottom InP cladding should be minimized to improve the lasing efficiency.

High speed DBR lasers are shown to be capable of 40 Gb/s digital transmission at 3 dB extinction ratio for back-to-back and through 1 km of standard single mode fiber. These lasers also demonstrate high spurious free dynamic range of 103 dB  $\text{Hz}^{2/3}$  over a bandwidth of 1-19 GHz for wide-band analog modulation applications.

Following conclusions can be drawn from the second part of the thesis.

- MQW  $1.55 \mu\text{m}$  laser structures based on InGaAsP/InGaAlAs combination with  $\lambda_g = 1.35 \mu\text{m}$  barrier showed improved performance in terms of  $T_0$ , optical gain, differential gain and chirp as compared to the optimized InGaAsP barrier. From carrier transport measurements, InGaAsP/InGaAlAs MQW with  $\lambda_g = 1.42 \mu\text{m}$  barrier has faster carrier transport, hence it can be used to increase the total number of wells beyond 20 in the present lasers. However, too shallow barrier will reduce the gain from the well, which might cancel the advantages obtained by improved carrier transport and more wells.

- LCI laser can be useful for direct modulation application, however the difficulties in fabricating such a device could hamper its progress.
- Optimized DBR lasers are a potential candidate for high bit-rate (40 Gb/s and beyond) digital and wide-band (1-20 GHz and beyond) low-distortion analog links.

### Future Work:

For future work, one can focus on the MoL formulation with reduced eigenvectors. In order to reduce the matrix size, one needs to find a way to neglect the un-necessary modes in the MoL matrix that are not important for grating response calculation. A systematic way should be found to include only the necessary radiation modes (in addition to the guided modes which are always important) which take part in the energy transfer process from one waveguide section to the next section for deep waveguide gratings. This will make the MoL beam propagation method useful for full 3D waveguide deep grating simulation. It can also be helpful to do full-vector bi-directional beam propagation for high contrast or metal clad waveguides for which the transverse mode can not be approximated by a scalar approximation. This method could be useful for the simulation of VCSEL device including the diffraction and polarization effects.

One can also do active waveguide simulation, such as for laser or optical amplifier, using MoL by a complex refractive index to model the optical gain. This could also be useful for the simulation of multi-section DFB, DBR and sampled grating tunable lasers. Since the MoL includes the radiation modes as well, one can simulate the grating coupler sections for tunable laser and second-order grating for vertical emission of the lasing radiation.

From a recent batch, we have achieved good lasing from a 20 well InGaAsP InGaAlAs FP laser. To further improve the bandwidth of a directly modulated laser, the number of wells in the active region can be increased beyond 20 to increase the confinement factor and reduce the carrier density in each well. For efficient carrier injection in such a large number of wells, one can use wells with even shallower barrier, such as the structure ‘C’ in **Paper G**. High speed lasers can be made with good ohmic contact and narrow contact pads to reduce the parasitics. By measuring the small-signal modulation response and the noise spectrum of such lasers, important device and material parameters such as the K-factor, D-factor, differential gain  $dg/dn$  and gain-compression factor  $\epsilon$  can be extracted. By doing carrier lifetime measurements, one can extract the carrier density vs current density relationship in the quantum wells. Once the active region of the laser is optimized, one can make optimized DFB and DBR lasers to get the highest possible bandwidth from the active region.

## Chapter 6

# Summary of the Original Work

In this section, a short summary of the original work is given. A short description of the author's contributions in each article is also given.

**Paper A:** *A New Higher-Order Finite-Difference Approximation Scheme for the Method of Lines.*

In this article, a new 5-point and a 7-point non-uniform mesh finite-difference scheme is derived to approximate the second-derivative operator in the wave equation. The scheme is applied using the Method of Lines for planar step-index waveguides. In this scheme, the necessary interface conditions for the  $TE$  and  $TM$  fields at an index and mesh discontinuity are appropriately included in the derivation. This scheme can model lossless and lossy dielectric material as well as metallic layers having negative real part of the refractive index in a unified way. Numerical results are given for the fundamental  $TE$  and  $TM$  modes of a high-contrast waveguide and for a metal/dielectric single interface  $TM$  surface-plasmon mode showing faster convergence behavior to the analytical results.

*Contribution by the author of the thesis:* The author derived the 5-point and the 7-point finite difference approximation. The author did all the programming in MATLAB, simulated different waveguides and verified the numerical accuracy of the derived algorithms. The author did the literature survey and wrote main parts of the the article.

**Paper B:** *Analysis of Deep Waveguide Gratings: An Efficient Cascading and Doubling Algorithm in the Method of Lines Framework.*

In this work, a new bidirectional non-paraxial beam propagation algorithm is derived which is computationally fast, numerically stable and memory efficient. The algorithm is called Cascading and Doubling algorithm and is implemented

within the Method of Lines (MoL) framework to model long planar waveguide gratings having many periods in the propagation direction. The perfectly matched layer (PML) absorbing condition is used to simulate free space around the grating and avoids the reflection of the radiating modes back into the simulation domain. This algorithm can model  $2^n$  grating periods in  $n$  calculational steps and needs  $N^2$  matrices for  $N$  sample points in the problem space. It can model periodic, quasi-periodic, symmetric and asymmetric gratings efficiently. Different deep waveguide gratings are modeled using this scheme and results for the fundamental *TE* mode spectral reflectivity are compared with published results showing excellent agreement.

*Contribution by the author of the thesis:* The author implemented the new algorithm in MATLAB combining with the results of the 5-point finite-difference algorithm of the **Paper A**, did all the simulations and compared the results with previously published results. The author did the literature survey and wrote major parts of the manuscript.

**Paper C:** *Analysis of Antiresonant Reflecting Optical Waveguide Gratings by use of the Method of Lines.*

In this work, a new polarizing device using anti-resonant reflecting optical waveguide (ARROW) structure is proposed. The modal spectral response of the ARROW grating is calculated using the Cascading and Doubling algorithm. A perfectly matched layer (PML) absorbing boundary condition is used to simulate the open space at the mesh termination for radiation modes and hence, both real and imaginary parts of the propagation constant can be calculated accurately. Power loss is introduced into the ARROW by changing its parameters and the response of the low-loss and the lossy ARROW gratings is analyzed and compared. The reflection and transmission spectra of the ARROW gratings are calculated for different number of grating periods, different groove depths and different power loss of the fundamental mode. The polarization discrimination property of the ARROW waveguide causes the ARROW grating to behave as a TE-pass reflection-mode filter (i.e. a band-pass wavelength filter that strongly reflects TE-polarized waves, while negligibly reflecting TM polarized waves.). A conventional grating does not exhibit this property.

*Contribution by the author of the thesis:* The author implemented the simulation combining with the results of the **Paper A** and **Paper B**, and generated all the results. The author proposed to use the ARROW grating slightly off-resonance in order to increase the polarization discrimination behavior of the deep ARROW grating. The author did the literature survey and wrote major parts of the manuscript.

**Paper D:** *Influence of Electrical Parasitics and Drive Impedance on the Laser Modulation Response.*

In this article, we have analyzed the effects of electrical parasitics and drive impedance on the laser modulation response using a modified rate equation

model. It is found that for lasers with small active-region volume e.g. VCSELs, the finite drive impedance and/or the laser parasitic capacitance can significantly enhance the damping of the laser resonance peak at low bias. This is due to the voltage fluctuations across the laser diode active layer during modulation. It is also shown that the real pole of the small-signal response transfer function corresponding to the laser parasitic cut-off frequency is not fixed but decreases with the increased bias level. This model might explain the decrease of parasitic cutoff frequency at high bias in the measured results.

*Contribution by the author of the thesis:* The author derived the modified rate equation model, and implemented the small-signal linearization of the rate equation model. The author did all the programming and simulations and wrote major parts of the manuscripts.

**Paper E:** *Design Optimization of InGaAsP-InGaAlAs 1.55  $\mu\text{m}$  Strain Compensated MQW Lasers for Direct Modulation Applications.*

In this work, a simulation study of InGaAsP well/ InGaAlAs barrier based 1.55  $\mu\text{m}$  strain-compensated MQW lasers is presented. It is shown that due to a large conduction band discontinuity in this material system, a higher material gain and differential gain can be obtained from such a quantum well as compared to a traditional InGaAsP/InGaAsP quantum well. The deeper electron well also improves elevated temperature operating characteristics and reduces the electron spillover from QWs. For MQWs, a uniform vertical distribution of holes is achievable due to a reduced effective hole confinement energy by optimizing the bandgap and the strain in the barriers. A large number of quantum wells having shallow barrier can be uniformly pumped, reducing the carrier density in each individual well which help reduce the total Auger recombination current. High p-doping in the active region is shown to enhance the carrier and gain non-uniformity in the MQWs especially for high barrier case. However, for the shallow barrier bandgap, the doping of the active region might be beneficial due to increased differential gain from the wells. A simulated high modulation bandwidth is demonstrated, promising directly modulated lasers as a low cost source for short to medium distance (1-10 km) high speed optical links.

*Contribution by the author of the thesis:* The author did the simulations using a commercial software and derived all the results. The author wrote major parts of the manuscript.

**Paper F:** *Lateral Current Injection (LCI) Multiple Quantum-well 1.55  $\mu\text{m}$  Laser with Improved Gain Uniformity Across the Active Region.*

In this article, a simulation study of lateral current injection 1.55  $\mu\text{m}$  laser with strain-compensated multiple quantum-well (MQW) active region (InGaAsP well, InGaAlAs barrier) is done using self-consistent 2D numerical simulations. The main advantage of the LCI structure is the possibility to have a large number of quantum wells in the active region without carrier injection bottleneck since all the QWs are fed in parallel. This makes it possible to reduce the carrier

density in each well, increase the confinement factor and increase the modulation bandwidth of the laser. The effects of different mesa width and p-doping in the QWs on the carrier and gain uniformity across the active region are explored. A high p-doping in the quantum wells is found to increase the carrier and gain non-uniformity across the active region. The QW region close to the n-contact side does not provide much gain at high optical powers. An asymmetric optical waveguide design is proposed to help reduce the gain non-uniformity across the active region. By shifting the optical modal peak toward the p-side, the modal overlap between the gain region and the optical mode is improved and a more even carrier and gain distribution is obtained. However, due to reduced bandgap of the quaternary *InGaAsP* p-cladding, an enhanced electron leakage out of the QWs into the p-cladding degrades the laser efficiency and increases the threshold current. Transient time-domain simulations are also performed to determine the small-signal modulation response of the laser promising a simulated high modulation bandwidth suitable for direct-modulation applications.

*Contribution by the author of the thesis:* The author did the simulations, derived all the results and wrote the manuscript.

**Paper G:** *The Effect of Barrier Composition on the Carrier Transport,  $T_0$ , Gain Spectrum and Chirp of 1.55  $\mu\text{m}$  Multiple Quantum Well Lasers.*

In this work, the effect of barrier bandgap and composition on the optical performance of 1.55  $\mu\text{m}$  *InGaAsP-InGaAlAs* multiple quantum well structures and Fabry-Perot lasers is evaluated experimentally. Direct carrier transport measurements are performed for strain-compensated MQW test structures using time-resolved photoluminescence upconversion. MQW test structures are grown with different barrier composition (*InGaAsP* and *InGaAlAs*) and barrier bandgap (varied from  $\lambda_g = 1440\text{nm}$  to  $1260\text{nm}$ ) having different conduction band  $\Delta E_c$  and valence band discontinuity  $\Delta E_v$  while keeping the same *InGaAsP* well composition ( $\lambda_g = 1550\text{nm}$ ) for all the structures. The ambipolar carrier transport is found to be faster in the structures with lower valence band discontinuity  $\Delta E_v$ . Regrown semi-insulating buried heterostructure Fabry-Perot (SIBH-FP) lasers are fabricated from similar quantum wells and their static characteristics (including optical gain and chirp spectra below threshold), thermal characteristics and small-signal modulation response is measured. Lasers with *InGaAlAs* barrier show improved high temperature operation, higher optical gain, higher differential gain and lower chirp making them suitable candidate for high bandwidth directly modulated uncooled laser applications.

*Contribution by the author of the thesis:* The author designed the experiments and the MQW structures for carrier transport measurements as well as for lasers. The author participated in the MOVPE epitaxy of the structures, did the carrier transport measurements and the laser measurements. The author wrote major parts of the manuscript.



**Paper H:** *40 Gb/s Transmission Experiment Using Directly Modulated 1.55  $\mu\text{m}$  DBR Lasers.*

In this work, transmission experiment is done using high speed detuned loaded DBR laser at 40 Gb/s. Successful error-free operation is achieved for back-to-back transmission and through 1 km of standard single mode fiber. The drive voltage is 2 V peak-peak and the bias current is 55-65 mA. These results show that directly modulated DBR lasers are useful for high speed 40Gb/s transmission at short distance. The transmission distance is limited by the dispersion in the fiber and can be improved with dispersion compensation techniques.

*Contribution by the author of the thesis:* The author participated in the transmission experiment, and wrote some parts of the manuscript.

**Paper I:** *Experimental Evaluation of Detuned Loading Effects on the Distortion in Edge Emitting DBR Lasers.*

In this experimental work, the analog performance of the high speed detuned loaded DBR lasers is evaluated experimentally. We have measured fundamental, third order intermodulation product IMD3 and noise in two-tone measurements, and calculate the spurious free dynamic range (SFDR) and the third order intersection point IP3. The lasers show high SFDR of 103 dB  $\text{Hz}^{2/3}$  in the 1-19 GHz range when tuned to the longer side of the DBR reflection peak.

*Contribution by the author of the thesis:* The author participated in the distortion measurements of the DBR lasers.



# Bibliography

- [1] S. T. Peng and T. Tamir. TM mode perturbation analysis of dielectric gratings. *Applied Physics*, 7(35):35–38, 1975.
- [2] Qing-Huo Liu and Weng Cho Chew. Analysis of discontinuities in planar dielectric waveguides : An eigenmode propagation method. *IEEE Transactions on Microwave Theory and Techniques*, 39(3):422–430, March 1991.
- [3] Yih Peng Chiou and Hung Chun Chang. Analysis of optical waveguide discontinuities using pade approximation. *IEEE Photonics Technology Letters*, 9:964–966, 1997.
- [4] Wei Dong Yang and R. Pregla. Method of lines for analysis of waveguide structures with multidiscontinuities. *Electronics Letters*, 31(11):892, May 1995.
- [5] Wei Dong Yang and Reinhold Pregla. The method of lines for analysis of integrated optical waveguide structures with arbitrary curved interfaces. *IEEE Journal of Lightwave Technology*, 14(5):879–884, May 1996.
- [6] J J Gerdes. Bidirectional eigenmode propagation analysis of optical waveguides based on method of lines. *Electronics Letters*, 30(7):550, March 1994.
- [7] J Gerdes, B Lunitz, D Benish, and R Pregla. Analysis of slab waveguide discontinuities including radiation and absorption effects. *Electronics Letters*, 28(11):1013, May 1992.
- [8] R Pregla and W Yang. Method of lines for analysis of multilayered dielectric waveguides with Bragg gratings. *Electronics Letters*, 29(22):1962, October 1993.
- [9] R Pregla and E Ahlers. Method of lines for analysis of discontinuities in optical waveguides. *Electronics Letters*, 29(21):1845, October 1993.
- [10] J Ctyroky, S Helfert, and R Pregla. Analysis of deep waveguide Bragg gratings. *Optical and Quantum Electronics*, 30(5):343–358, 1998.

- [11] Stefan F. Helfert and Reinhold Pregla. Efficient analysis of periodic structures. *IEEE Journal of Lightwave Technology*, 16(9):1694–1702, September 1998.
- [12] Ashmeet Kaur Taneja and Anurag Sharma. Reflection characteristics of guided wave Bragg gratings using the collocation method. *SPIE Proceedings, International conference on fiber optics and photonics*, 3666:112–119, April 1999.
- [13] Jose Rodriguez, R. D. Crespo, and S. Fernandez. Radiation losses on discontinuities in integrated optical waveguides. *Optical Engineering*, 38(11):1896–1906, November 1999.
- [14] D. Marcuse. *Theory of Dielectric Optical Waveguides*. Academic Press Inc., 1974.
- [15] D. C. Flanders and H. Kogelnick. Grating filters for thin-film optical waveguides. *Applied Physics Letters*, 24(4):194–196, February 1974.
- [16] Kim A. Winick. Effective-index method and coupled-mode theory for almost-periodic waveguide gratings: a comparison. *Applied Optics*, 31(6):757–764, February 1992.
- [17] V. Vemuri and Walter J. Karplus. *Digital Computer Treatment of Partial Differential Equations*. Prentice-Hall Series in Computational Mathematics. Prentice Hall, Inc., Englewood Cliffs, New Jersey 07632, 1981.
- [18] Tatsuo Itoh, editor. *Numerical Techniques for Microwave and Millimeter-Wave Passive Structures*. John Wiley and Sons, 1989.
- [19] J. Gerdes and R. Pregla. Beam-propagation algorithm based on the method of lines. *Journal of Optical Society of America (B)*, 8(2):389–394, February 1991.
- [20] U. Rogge and R. Pregla. Method of lines for the analysis of strip-loaded optical waveguides. *Journal of Optical Society of America (B)*, 8(2):459–463, February 1991.
- [21] Ulrich Rogge. *Method of Lines for the Analysis of Dielectric Waveguides*. PhD thesis, Fern University, Hagen, Germany, 1991.
- [22] Weidong Yang. *Method of Lines for Analysis of Passive and Active Integrated Optical Devices*. PhD thesis, Fern University, Hagen, Germany, 1996.
- [23] M A Duguay, Y Kokubun, T L Koch, and Loren Pfeiffer. Antiresonant reflecting optical waveguides in  $\text{SiO}_2 - \text{Si}$  multilayer structures. *Applied Physics Letters*, 49(1):13–15, July 1986.

- [24] Weiping Huang, Raed M Shubair, Arokia Nathan, and Y Leonard Chow. The modal characteristics of ARROW structures. *IEEE Journal of Lightwave Technology*, 10(8):1015–1022, August 1992.
- [25] Jacek Kubica. Modal propagation within ARROW waveguides. *Optics Communications*, 78(2):133–136, August 1990.
- [26] J L Archambault, R J Black, S Lacroix, and J Bures. Loss calculations for antiresonant waveguides. *IEEE Journal of Lightwave Technology*, 11(3):416–423, March 1993.
- [27] Olle Kjebon, R. Schatz, S. Lourdudoss, S. Nilsson, and B. Staltnacke L. Backbom. 30 Ghz direct modulation bandwidth in detuned loaded InGaAsP DBR lasers at 1.55  $\mu\text{m}$  wavelength. *Electronic Letters*, 33(6):488–489, March 1997.
- [28] Olle Kjebon, M. N. Akram, and Richard Schatz. 40 Gb/s transmission experiment using directly modulated 1.55  $\mu\text{m}$  DBR lasers. In *Indium Phosphide and Related Materials*, pages 495–498. IEEE, May 2003.
- [29] Yasuhiro Matsui, Hitoshi Murai, Shin Arahira, Satoko Kutsuzawa, and Yoh Ogawa. 30-GHz bandwidth 1.55- $\mu\text{m}$  strain-compensated InGaAlAs-InGaAsP MQW laser. *IEEE Photonics Technology Letters*, 9(1):25–27, January 1997.
- [30] Larry A. Coldren and Scott W. Corzine. *Diode Lasers and Photonic Integrated Circuits*. Microwave and Optical Engineering. John Wiley and Sons, Inc., 1995.
- [31] Richard Schatz. *On the Stability and Dynamics of Semiconductor Lasers*. PhD thesis, Royal Institute of Technology, Stockholm, Sweden, August 1994.
- [32] A. J. Lowery. Transmission-line modelling of semiconductor lasers: the transmission-line laser model. *International Journal of Numerical Modelling: Electronic Networks, Devices and Fields*, 2(4):249–265, 1989.
- [33] Zhang-Ming Li, Kenneth M. Dzurko, Andre Delage, and Sean P. McAlister. A self-consistent two dimensional model of quantum well semiconductor lasers: optimization of a GRIN-SCH SQW laser structure. *IEEE Journal of Quantum Electronics*, 28(4):792–803, April 1992.
- [34] PICS3D. Pics3d users’s manual. <http://www.crosslight.com>, 2002.
- [35] M. J. Adams. *An Introduction to Optical Waveguides*. John Wiley and Sons, 1981.
- [36] Richard Symms and John Cozens. *Optical Guided Waves and Devices*. McGraw-Hill Book Company Europe, Shopenhangers Road, Maidenhead, Berkshire, SL6 2QL, England, 1992.

- [37] Abiodun Ahmad Shittu. *Study of periodic waveguides by the finite-difference time-domain method and the Method of Lines*. PhD thesis, King Fahad University of Petroleum and Minerals, Dhahran 31261, Saudi Arabia, September 1994.
- [38] S J Al-Bader and H A Jamid. Perfectly matched layer absorbing boundary conditions for the method of lines modeling scheme. *IEEE Microwave and Guided Waves Letters*, 8(11):357–359, November 1998.
- [39] Muhammad Nadeem Akram. Analysis of anti-resonant reflecting optical waveguide (ARROW) grating using the method of lines. Master's thesis, King Fahd University of Petroleum and Minerals, Dhahran 31261, Saudi Arabia, April 2000.
- [40] Toshihiko Baba, Motoshi Hamasaki, Nobuaki Watanabe, Pasu Kaewplung Akihiro Matsutani, Toshikazu Mukaihara, Fumio Koyama, and Kenichi Iga. A novel short-cavity laser with deep-grating distributed bragg reflectors. *Jpn. J. Appl. Phys*, 35(2B):1390–1394, February 1996.
- [41] I. Hayashi, M. B. Panish, and P. W. Foy. A low-threshold room temperature injection laser. *IEEE Journal of Quantum Electronics*, 5(4):211–212, April 1969.
- [42] LASTIP. Lastip users's manual. <http://www.crosslight.com>, 2002.
- [43] Yasuji Seko and Akira Sakamoto. Valence subband structures and optical properties of strain-compensated quantum wells. *Japanese Journal of Applied Physics*, 40(1):34–39, January 2001.
- [44] Shunji Seki, Takayuki Yamanaka, Wayne Lui, and Kiyoyuki Yokoyama. Theoretical analysis of differential gain of 1.55  $\mu\text{m}$  InGaAsP/InP compressive strained multiple quantum well lasers. *Journal of Applied Physics*, 75(3):1299–1303, February 1994.
- [45] S. L. Chuang. *Physics of Optoelectronic Devices*. Wiley series in Pure and Applied Optics. John Wiley and Sons, Inc., 1995.
- [46] K. Fröjdh and S. Marcinkevicius. Interwell carrier transport in InGaAsP multiple quantum well laser structures. *Applied Physics Letters*, 69(24):3695–3697, December 1996.
- [47] Joachim Piprek, J. Kenton White, and Anthony J. SpringThorpe. What limits the maximum output power of long-wavelength AlGaInAs/InP laser diodes ? *IEEE Journal of Quantum Electronics*, 38(9):1253–1259, September 2002.
- [48] Joachim Piprek, Patrick Abraham, and John E. Bowers. Carrier non-uniformity effects on the internal efficiency of multiquantum well laser. *Applied Physics Letters*, 74(4):489–491, January 1999.

- [49] Takuya Ishikawa and John E. Bowers. Band lineup and in-plane effective mass of InGaAsP or InGaAlAs on InP strained layer quantum well. *IEEE Journal of Quantum Electronics*, 30(2):562–570, February 1994.
- [50] Joachim Piprek, Patrick Abraham, and John E. Bowers. Self-consistent analysis of high-temperature effects on strained-layer multiquantum-well InGaAsP-InP lasers. *IEEE Journal of Quantum Electronics*, 36(3):366–374, March 2000.
- [51] P. Abraham, J. Piprek, S. P. Denbaars, and J. E. Bowers. Study of temperature effects on loss mechanics in  $1.55\ \mu\text{m}$  laser diodes with  $\text{In}_{0.81}\text{Ga}_{0.19}\text{P}$  electron stopper layer. *Semiconductor Science and Technology*, 14:419–424, 1999.
- [52] Yasuhiro Matsui, Hitoshi Murai, Shin Arahira, Yoh Ogawa, and Akira Suzuki. Novel design scheme for high-speed MQW lasers with enhanced differential gain and reduced carrier transport effect. *IEEE Journal of Quantum Electronics*, 34(12):2340–2349, December 1998.
- [53] Christofer Silfvenius, Gunnar Landgren, and Saulius Marcinkevicius. Hole distribution in InGaAsP  $1.3\ \mu\text{m}$  multiple quantum well laser structures with different hole confinement energies. *IEEE Journal of Quantum Electronics*, 35(4):603–607, April 1999.
- [54] Seong-Ju Bae, Seoung-Hwan Park, and Yong-Tak Lee. Bandgap effects of quantum well active layer on threshold current density, differential gain and temperature characteristics of  $1.3\ \mu\text{m}$  InGaAlAs-InP quantum well lasers. *Japanese Journal of Applied Physics*, 41(3A):1354–1358, March 2002.
- [55] O. Issanchou, J. Barrau, E. Idiart-Alhor, and M. Quillec. Theoretical comparison of GaInAs/GaAlInAs and GaInAs/GaInAsP quantum-well lasers. *Journal of Applied Physics*, 6(15):3925–3930, September 1995.
- [56] J Minch, S. H. Park, T. Keating, and S. L. Chuang. Theory and experiment of  $\text{In}_{1-x}\text{Ga}_x\text{As}_y\text{P}_{1-y}$  and  $\text{In}_{1-x-y}\text{Ga}_x\text{Al}_y\text{As}$  long-wavelength strained quantum-well lasers. *IEEE Journal of Quantum Electronics*, 35(5):771–782, May 1999.
- [57] M. L. Xu, G. L. Tan, J. M. Xu, M. Irikawa, H. Shimizu, T. Fukushima, Y. Hirayama, and R. S. Mand. Ultra-high differential gain in GaInAs-AlGaInAs quantum wells: Experiment and modeling. *IEEE Photonics Technology Letters*, 7(9):947–949, September 1995.
- [58] Yasuhiro Matsui, Hitoshi Murai, Shin Arahira, Yoh Ogawa, and Akira Suzuki. Enhanced modulation bandwidth for strain-compensated InGaAlAs-InGaAsP MQW lasers. *IEEE Journal of Quantum Electronics*, 34(10):1970–1978, October 1998.

- [59] Muhammad A. Alam, Mark H. Hybertsen, R. Kent Smith, and Gene A. Baraff. Simulation of semiconductor quantum well lasers. *IEEE Transactions on Electronic Devices*, 47(10):1917–1925, October 2000.
- [60] Edward H. Sargent. Semiconductor lasers for planar integrated optoelectronics. *Solid-State Electronics*, 44:147–173, 2000.
- [61] Edward (Ted) H. Sargent, Genlin Tan, and Jimmy M. Xu. Lateral current injection lasers: Underlying mechanism and design for improved high-power efficiency. *IEEE Journal of Lightwave Technology*, 16(10):1854–1864, October 1998.
- [62] Edward H. Sargent, Geo-Lin Tan, and Jimmy M. Xu. Physical model of OEIC-compatible lateral current injection lasers. *IEEE Journal of Selected Topics in Quantum Electronics*, 3(2):507–512, April 1997.
- [63] Genlin Tan, Keith Lee, and J. M. Xu. Finite element light emitter simulator FELES: A new 2D software design tool for laser devices. *Japanese Journal of Applied Physics*, 32(1B):583–589, January 1993.
- [64] Edward H. Sargent, Kunishige Oe, Catherine Caneau, and J. M. Xu. OEIC-enabling LCI lasers with current guides: combined theoretical-experimental investigation of internal operating mechanism. *IEEE Journal of Quantum Electronics*, 34(7):1280–1287, July 1998.
- [65] Edward H. Sargent, D. A. Suda, A. Margittai, F. R. Shepherd, M. Cleroux, G. Knight, N. Puetz, T. Makino, J. SpringThorpe, G. Chik, and J. M. Xu. Experimental study of LCI lasers fabricated by single MOCVD overgrowth followed by selective dopant diffusion. *IEEE Photonics Technology Letters*, 10(11):1536–1538, November 1998.
- [66] K. Oe, Y. Noguchi, and C. Caneau. GaInAsP lateral current injection lasers on semi-insulating substrates. *IEEE Photonics Technology Letters*, 6(4):479–481, April 1994.
- [67] Y. Kawamura, Y. Noguchi, and H. Iwamura. Lateral current injection In-GaAs/InAlAs MQW lasers grown by GSMBE/LPE hybrid method. *Electronics Letters*, 29(1):102–104, January 1993.
- [68] A. A. Tager, R. Gaska, I. A. Avrutsky, M. Fay, H. Chik, A. SpringThorpe, S. Eicher, J. M. Xu, and M. Shur. Ion-implanted GaAs-InGaAs lateral current injection laser. *IEEE Journal of Selected Topics in Quantum Electronics*, 5(3):664–672, May/June 1999.
- [69] Akira Furuya, Masao Makiuchi, Osamu Wada, and Toshio Fujii. Al-GaAs/GaAs lateral current injection multiquantum well LCI-MQW laser using impurity-induced disordering. *IEEE Journal of Quantum Electronics*, 24(12):2448, December 1988.



- [70] A. Furuya, M. Makiuchi, and O. Wada. Continuous-wave operation of lateral current injection multi-quantum-well laser. *Electronics Letters*, 24(20):1282–1283, September 1988.
- [71] C. A. Beyler, S. G. Hummel, Q. Chen, J. S. Osinski, and P. D. Dapkus. Low threshold current lateral injection laser on semi-insulating substrates fabricated using Si impurity-induced disordering. *Electronics Letters*, 27(15):15–17, July 1991.
- [72] Sebastian Lourdudoss and Olle Kjebon. Hydride vapor phase epitaxy revisited. *IEEE Journal of Selected Topics in Quantum Electronics*, 3(3):749–767, June 1997.
- [73] Jagdeep Shah. Ultrafast luminescence spectroscopy using sum frequency generation. *IEEE Journal of Quantum Electronics*, 24(2):276–288, February 1988.
- [74] H. Hillmer and S. Marcinkevicius. Optically detected carrier transport in III/V semiconductor QW structures: experiments, model calculations and applications in fast 1.55  $\mu\text{m}$  laser devices. *Applied Physics B*, 66:1–17, 1998.
- [75] Nir Tessler, Saulius Marcinkevicius, Ulf Olin, Christofer K. V. Silfvenius, Björn F. Stålnacke, and Gunnar Landgren. Vertical carrier transport in InGaAsP multiple quantum well laser structures: effect of p-doping. *IEEE Journal of Selected Topics in Quantum Electronics*, 3(2):315–319, April 1997.
- [76] Olle Kjebon, R. Schatz, S. Lourdudoss, S. Nilsson, and B. Stålnacke. Modulation response measurements and evaluation of MQW InGaAsP lasers of various designs. *High Speed Semiconductor Laser Sources*, 2684:138–152, April 1996.
- [77] B. W. Hakki and T. L. Paoli. Gain spectra in GaAs double heterostructure injection lasers. *Journal of Applied Physics*, 46:3096–3099, 1975.
- [78] C-S. Chang, S. L. Chuang, J. R. Minch, W. W. Fang, Y. K. Chen, and T. Tanbun-Ek. Amplified spontaneous emission spectroscopy in strained quantum-well lasers. *IEEE Journal of Selected Topics in Quantum Electronics*, 1(4):1100–1107, December 1995.
- [79] Johan Nilsson. Measurement of wavelength and current dependence of gain, refractive index and internal loss in semiconductor lasers. Technical report, Royal Institute of Technology, IMIT Department, Stockholm 16440, Sweden, December 1996.
- [80] Eilert Berglind and Lars Gillner. Optical quantum noise treated with classical electrical network theory. *IEEE Journal of Quantum Electronics*, 30(1):846–853, March 1994.

- [81] K. Vahala and K. Yariv. Detuned loading in coupled cavity semiconductor lasers-effect on quantum noise and dynamics. *Applied Physics Letters*, 45:501–503, May 1984.
- [82] O. Kjebon and E. Almström. Transmission over 125 km standard fiber at 10 Gb/s with two section DBR laser. *Proc. 25th European Conference on Optical Communication*, 1:378–379, September 1999.
- [83] Olle Kjebon and E. Almström. Transmission at 20 Gb/s with directly modulated DBR laser over 30 km standard fiber. *European conference on optical communications*, September 2002.
- [84] K. Sato, S. Kuwahara, Y. Miyamoto, and N. Shimizu. 40 Gb/s direct modulation of distributed feedback laser for very short reach optical links. *Electronic Letters*, 38(15):816–817, July 2002.
- [85] W. S. C. Chang, editor. *RF Photonics Technology in Optical Fiber Links*. Cambridge Publishers, Cambridge University Press, Edinburgh Building, Cambridge CB2 2RU, UK, 2002.